CHALMERS
UNIVERSITY OF TECHNOLOGY

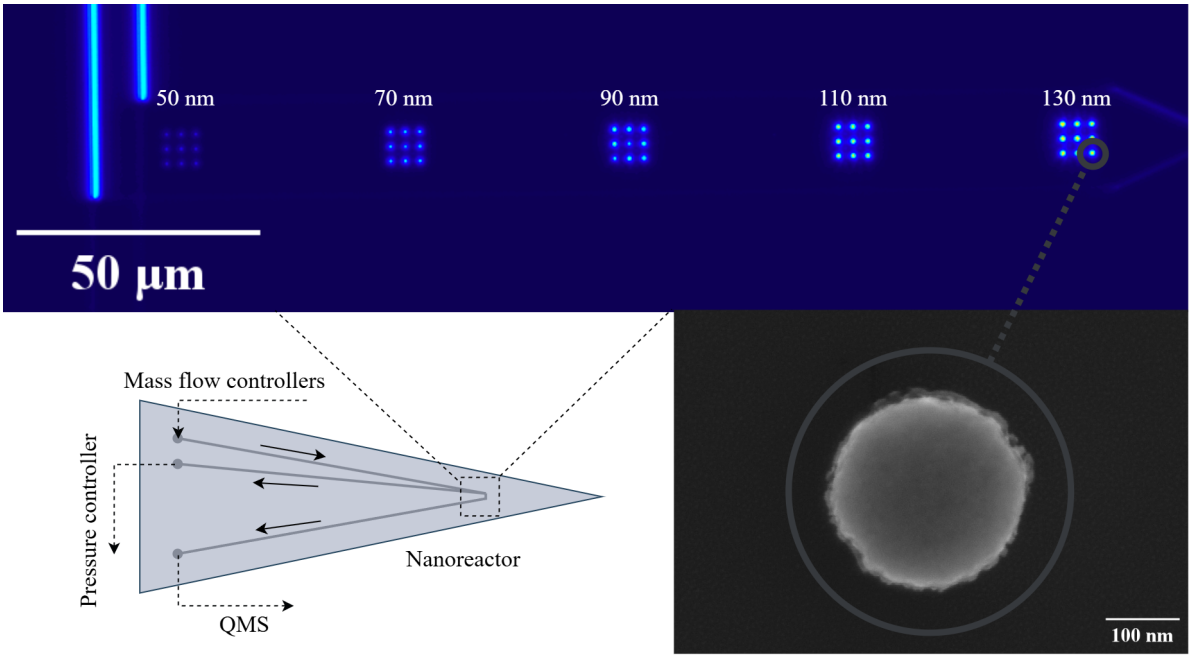

Temperature-dependent reaction dynamics of CO-oxidation on Pt nanoparticles

Probed at a single-particle level under *operando* conditions using temperature-programmed nanoplasmonic sensing

Master's thesis in Nanotechnology

ANTON KAISER OLSSON

DEPARTMENT OF PHYSICS

CHALMERS UNIVERSITY OF TECHNOLOGY
Gothenburg, Sweden 2026
www.chalmers.se

Master's thesis 2026

Temperature-dependent reaction dynamics of CO-oxidation on Pt nanoparticles

Probed at a single-particle level under *operando* conditions using temperature-programmed nanoplasmonic sensing

ANTON KAISER OLSSON

CHALMERS
UNIVERSITY OF TECHNOLOGY

Department of Physics
Division of Chemical Physics
Christoph Langhammer's gruop
Chalmers University of Technology
Gothenburg, Sweden 2026

Temperature-dependent reaction dynamics of CO-oxidation on Pt nanoparticles
Probed at a single-particle level under *operando* conditions using temperature-programmed nanoplasmonic sensing

ANTON KAISER OLSSON

Supervisor: Giuseppe Abbondanza, Department of Physics
Examiner: Christoph Langhammer, Department of Physics

Master's Thesis 2026
Department of Physics
Division of Chemical Physics
Christoph Langhammer's gruop
Chalmers University of Technology
SE-412 96 Gothenburg
Telephone +46 31 772 1000

Acknowledgements, dedications, and similar personal statements in this thesis, reflect the author's own views.

Cover: [Diagram of the nanoplasmonic sensing chip, complemented by a dark-field microscopy image of the nanoreactor and particle arrays, together with an SEM image of a nanoparticle with a radius of 130 nm.]

Typeset in LaTeX
Printed by Chalmers Reproservice
Gothenburg, Sweden 2026

Temperature-dependent reaction dynamics of CO-oxidation on Pt nanoparticles
Probed at a single-particle level under *operando* conditions using temperature-programmed nanoplasmonic sensing

ANTON KAISER OLSSON

Department of Physics
Chalmers University of Technology

Abstract

Key to the continued development of catalysts is bridging the gap between research and industrial operating conditions, or *operando* conditions. Additionally, to achieve a deeper understanding of catalytic dynamics, single-particle analysis has gained popularity as a way to mitigate the loss of information brought about by ensemble-averaging effects. In an effort to both bridge the gap between the research and application while allowing probing at the single-particle level, a technique called nanoplasmonic sensing has emerged. Nanoplasmonic sensing relies on the inherent plasmonic properties of catalytic metal nanoparticles to probe catalytic reactions.

In this thesis, the temperature-dependent reaction dynamics of CO-oxidation facilitated by Pt nanoparticles on a SiO_2 substrate were studied, with a focus on the dynamics of the kinetic phase transitions of Pt nanoparticles between their CO-poisoned and catalytically active states. This was investigated at both the ensemble and single-particle levels under *operando* conditions by performing temperature-programmed nanoplasmonic sensing on a nanoreactor chip hosting the Pt nanoparticles and the chemical reaction. Additionally, the effects of particle size and reactant ratio on the reaction dynamics were studied. To complement the nanoplasmonic sensing measurements, a structural analysis involving hyperspectral and SEM imaging was conducted.

In this thesis, it was shown that temperature-dependent reaction dynamics could be obtained using nanoplasmonic sensing by applying a newly in-house-developed autofocusing software to counteract the drift in focus caused by the thermal expansion of the nanoparticles. Additionally, the critical temperatures of the kinetic phase transitions were evaluated using a statistical method called the bootstrap approach. One of the observed transitions aligned with the expected critical temperatures. However, an additional lower-temperature transition was also observed, and further analysis is required to evaluate whether this transition represents a real physical phenomenon or a measurement/data-treatment artifact. The nanoplasmonic sensing results were supported by the structural analysis, in which irreversible structural changes were observed in the nanoparticles, alluding to insufficient annealing. When assessing the effect of particle size, differences in the observed dynamics between ensemble and single-particle analyses were found, highlighting the need for further analysis at the single-particle level.

Keywords: Nanoplasmonics, PtNP, Operando, Single-particle, Nanoreactors, Dark-field, Hyperspectral, SEM, QMS, CO-poisoning.

Acknowledgments

This has been a long and fulfilling project to be part of, and it is thanks to the many people who have helped me throughout this journey that it all came together. This section is dedicated to thanking all of you.

First, I'd like to thank my examiner, Christoph, for taking me into his group and giving me the opportunity to work on this thesis, as well as my supervisor, Giuseppe, who has been indispensable in helping and guiding me through the project. Additionally, I'd like to thank everyone in the Langhammer group and all those working at the Division of Chemical Physics for being so kind and supportive. Special thanks to Lova, Oscar, and especially Joachim Fritzsche, who produced the chips used in this thesis at the Chalmers MC2 facilities.

Furthermore, I'd like to thank David Albinsson, whose doctoral thesis this project is very heavily rooted in.

Lastly, I'd like to thank my mom, Veronica, my dad, Thomas, and my younger brother, Joel, for all the support they have given me, not just throughout the course of this thesis or during my university years, but throughout my entire life.

Thank you all!

Anton Kaiser Olsson, Gothenburg, July 2026

List of Acronyms

Below is the list of acronyms that have been used throughout this thesis listed in alphabetical order:

AES	Auger Electron Spectroscopy
EM	Electron Microscopy
EM-CCD	Electron Multiplying Charge-coupled Device
ER	Eley-Ridea
ETEM	Environmental Transmission Electron Microscopy
LC	Liquid Crystal
LEED	Low-energy Electron Diffraction
LH	Langmuir-Hinshelwood
LSP	Localized Surface Plasmon
LSPR	Localized Surface Plasmon Resonance
NP	Nanoparticle
PtNP	Platinum Nanoparticle
SEM	Scanning Electron Microscope
SMFM	Single-molecule Fluorescence Microscopy
STM	Scanning Tunneling Microscopy
TEM	Transmission Electron Microscopy
UHV	Ultra-high Vacuum
QMS	Quadrupole Mass Spectrometer
XRD	X-ray Diffraction

Contents

List of Figures

List of Tables

Chapter 1

Introduction

Since the emergence of nanotechnology as a scientific field, it has developed in close parallel with new sensing and measuring techniques. From a modern perspective, the two fields are, in a sense, interwoven with each other. As materials are scaled down to the nanometer regime (10^{-9} m), nanoscale properties begin to dominate over bulk properties [1]. Although nanotechnology as a formal field began development during the 20th century, the integration of nanoscale materials into human-made objects has been carried out for upwards of two millennia [2]. A most famous historic example of which, developed by the ancient Romans, is the integration of gold and silver nanoparticles (NPs) when staining glass in order to make vibrant colors or dichroic glass. The best known example of this Roman handcraft is the Lycurgus Cup, made in the 4th century, which exhibit different colors depending on the direction of the incoming light. This optical effect arise due to a nanoscale phenomenon known as localized surface plasmon resonance (LSPR), which emerge when the dimensions of a metallic material are scaled down to be smaller than the wavelength of visible light (that is less than 800 - 700 nm) [3].

The utilization of LSPR and other plasmonic phenomena for sensing and communication falls within nanoplasmonics, a subfield of nanophotonics, the study of how light interacts with nanoscale structures, and is a very active area of research [3],[4]. One area in particular that is currently integrating plasmonics into its repertoire is that of heterogeneous catalysis [3]. Catalysts are essential in chemistry and play an important role in both scientific and industrial applications, particularly in the chemical manufacturing, petrochemical, automotive, and fertilizer industries. From a modern perspective, catalysts are also central to many environmental and climate change questions due to their ability to reduce pollution [5],[6]. Catalysts work by accelerating the kinetics of a reaction, that is, the speed at which a reaction occurs, through the addition of intermediary reaction steps that are more thermodynamically favorable [7]. Crucially, in an ideal catalyst, none of the catalyzing material is consumed during the reaction, but the same amount persists afterward as before. Heterogeneous catalysis involves catalysts that exist in a different phase compared to the reactants of the reaction, such as solid-phase catalysts with either gaseous or

liquid reactants, with the reaction taking place at the phase boundary at so-called catalytic interfaces [8].

Common solid-phase heterogeneous catalysts consist of catalytically active metallic nanoparticles dispersed within a porous and inert supporting framework to maximize the number of accessible catalytic interfaces where reactions can occur [8]. However, these nanoparticles can vary significantly in size, shape, surrounding environment, and crystallinity, but studying the impact of these properties has proven challenging [3]. Traditionally, when characterizing solid-phase heterogeneous catalysts, all of these effects are averaged out as ensemble averages due to the inability to study the impact of the nanoparticles at a single-particle level of fidelity; this has facilitated the emergence of single-particle analysis.

Single-particle analysis of catalytic materials is a developing field of fundamental science that aims to study and model the underlying properties of nanoscopic particles for their catalytic use. The field comprises many promising techniques, such as X-ray microscopy, different types of electron microscopy (EM), and surface-enhanced Raman spectroscopy [9]. Traditionally, most of these techniques contain some fundamental flaws for the development of applicable research and modeling, namely the so-called "pressure gap" and "material gap" [3],[10]. These techniques often require model systems or ultra-high vacuum (UHV) conditions to function, both of which differ from realistic conditions. What is of interest is the development of single-particle analysis techniques that function at both high pressures and temperatures, that is in *operando* (or under operating conditions), as well as for realistic models system. For the future development of catalysis, it is essential to bridge both of these gaps, and a promising technique aiming precisely for that is nanoplasmonic sensing.

Some of the most commonly used metal nanoparticles in solid phase heterogeneous catalysts, such as platinum (Pt) and palladium (Pd), exhibit weak but detectable plasmonic signals [11]. By detecting changes in the plasmonic response due to changes in the local environment surrounding the nanoparticles, as well as structural changes, both of which influence plasmonic behavior, it is possible to probe and characterize the catalyst at a single-particle level. As the plasmonic response is not significantly impaired by high pressures and temperatures, a plasmonic signal can be detected *operando*. This approach, of using the plasmonic properties of the catalytic nanoparticles to probe the catalytic function, is referred to as nanoplasmonic sensing.

One of the most studied heterogeneous catalytic reactions is the CO-oxidation reaction, as this reaction plays an important role in removing combustion-related pollutants [5]. It is especially prevalent in the automotive industry, where it is used in catalytic converters to remove poisonous CO gas from exhaust by reacting it with O_2 and converting it into inert CO_2. To facilitate this reaction, a catalyst is required, and in catalytic converters, Pt nanoparticles are commonly used as the catalytic material. Owing to the extent to which this reaction has been studied and its importance from both industrial and environmental viewpoints, this reaction has become a model reaction for the characterization of heterogeneous catalytic

processes.

Finally, as shown by D. Albinsson et al. [3],[12], the combination of a nanofluidic reactor (or nanoreactor), that is, an isolated flow system retaining at least one dimension on the nanometer scale designed to host chemical reactions, with nanoplasmonic sensing allows for the integration of a quadrupole mass spectrometer (QMS) to measure the resulting outflow from the reactor. This allows for ensemble monitoring of the reaction in parallel with nanoplasmonic monitoring. Previous work using this setup was limited to isothermal measurements due to thermal expansion of the entire nanofluidic chip, causing the nanoparticles to drift out of focus from the camera used to capture the plasmonic signal. However, due to instrumental developments and an in-house-developed autofocusing script, it has become possible to investigate temperature-dependent systems, thus enabling the probing of temperature-programmed reaction dynamics.

1.1 Aim

Building upon established isothermal research combining nanofluidic reactors with nanoplasmonic sensing to achieve *operando* single-particle analysis, this thesis aims to investigate the introduction of temperature dependence into the system across different particle sizes and reactant ratios.

Utilizing new instrumental upgrades, as well as a newly developed in-house autofocusing script designed to counteract the thermal drift of the chip, nanoplasmonic sensing will be used to characterize and study the dynamics of the CO-oxidation reaction catalyzed by platinum nanoparticles (PtNPs). This on both the ensemble and single-particle levels for nanoparticles with radii ranging from 50 nm to 130 nm. To emulate the porosity of a real catalyst, the nanoparticles were ordered into arrays according to particle size and studied on the same nanofluidic chip to minimize cross-experimental error. Additionally, to characterize the effect of reactant ratios on the temperature-dependent dynamics, different $CO:O_2$ gas compositions will be investigated. The plasmonic response will be paired with QMS readings, allowing for monitoring of reaction productivity.

Lastly, a structural analysis of the nanoparticles will be conducted with the aim of investigating any reversible or irreversible morphological or crystalline changes, utilizing scanning electron microscopy (SEM) and hyperspectral imaging. This aim was added later in the project as a result of findings from the nanoplasmonic sensing measurements.

1.2 Scope of thesis

This thesis presents the *operando* characterization of single-particles as a function of temperature dependency and particle size. For this, only the CO-oxidation reaction catalyzed by Pt nanoparticles has been studied; as a model reaction. This has been carried out utilizing both nanoplasmonic sensing paired with QMS readings.

Additionally, in order to investigate potential temperature-dependent structural

changes that arose during the development of the project, a combination of hyperspectral imaging and SEM was used. As the nanoparticles were sealed within the nanofluidic chip by a lid blocking the electron beam used for SEM imaging, a control version of the nanoreactor without a lid was fabricated and treated with the same temperature and gas-flow exposure conditions as the main chip. This allowed SEM imaging to investigate structural changes that may have occurred throughout the experimental process.

Concerning the writing of the thesis, A.I. was used throughout the writing process, but strictly as a writing aid, in accordance with Chalmers' 2026 guidelines regarding the use of it. A.I. was only used to correct grammatical errors and occasionally improve the flow of paragraphs. No auto-generated text was used in this thesis, nor was A.I. used for data analysis or to draw any conclusions. For further assessment of this, and for an example of exactly how A.I. was used in this thesis, see Appendix A.

Chapter 2

Theory

The following chapter assesses key concepts necessary to provide the theoretical background for this thesis. First, the fundamentals of catalysis and catalyst characterization will be addressed, followed by the theory of nanoplasmonic sensing, the development of combining nanofluidics and single-particle techniques for catalytic characterization, and finally, a section providing the underlying basics of SEM theory.

2.1 Catalysis

Catalysis has been an essential to the field of chemistry since its conception by the hands of Elizabeth Fulhame in 1794 [13] and its coining by J. J Berzelius in 1836. A catalyst is a material that accelerates the rate of a reaction without itself being consumed [7],[14]. To understand how and why this matters, two key concepts in chemistry need to be considered: thermodynamics and kinetics. Thermodynamics is a very broad subject, but for this thesis it is important to note that thermodynamics determines which reactions can and cannot occur. If a reaction can occur, it will proceed in the direction that is most energetically stable, and thus most thermodynamically favorable. However, just because a reaction will occur does not mean that the speed at which it happens will be fast.

The most famous example used to illustrate the connection between thermodynamics and kinetics is diamond, which is thermodynamically unstable and will, over time, transform into graphite due to it being more thermodynamically favorable [14]. However, the rate at which this naturally occurs is so slow that it is essentially negligible unless heat is provided. Heat adds additional energy that allows the bonds in the carbon crystal to break more easily, thereby increasing the rate at which the diamond breaks down. The same is true for chemical reactions. The best way to illustrate this is by using a diagram, see Figure 2.1. Two compounds, **A** and **B**, where **B** is more energetically favorable (due to it having lower energy), are separated by an energy barrier E_a. To overcome this barrier a large amount of energy, often in the form of heat (as $E = k_B T$ where E is energy, T is temperature and k_b is the so-called Boltzmann constant), is needed. A statistical principle that

governs the probability that a species pass over the barrier is called Boltzmann distribution [15], $p_i \propto exp(-\frac{E_a}{k_B T})$.

A catalyst introduces intermediary steps that lowers the energy barrier [7], thus allowing the reactions to occur at a quicker rate, as illustrated in Figure 2.1. Importantly, the catalyst is not consumed in the reaction, and in principle once the reaction has occurred, the catalyst returns to its original state.

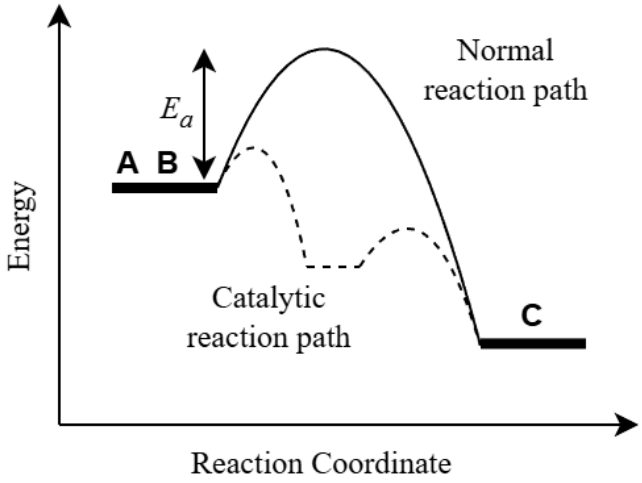

Figure 2.1: Diagram showcasing the catalytic reaction path (dashed line), contra the normal reaction path, for a reaction where reactants **A** and **B** reacts to become **C**.

2.1.1 Heterogeneous catalysts

Heterogeneous catalysts are a classification of catalysts in which the catalytic material and the reactants are in different phase states from each other [8],[7], typically with a solid catalyst and reactants in the liquid or gas phase. In these solid-phase heterogeneous catalysts, the reaction takes place at the phase boundary between the catalytic material and the reactants.

As the solid catalytic material terminates at the phase boundary, the outermost atoms at the surface are not fully surrounded by neighboring atoms and thus contain unsaturated orbitals, which make the boundary atoms much more reactive compared to those in the bulk material [1],[15]. The high reactivity of these surface atoms allows them to easily react with other species through different reaction mechanisms [16], mainly the Langmuir–Hinshelwood (LH) mechanism, where two reactants are adsorbed onto the surface and react with each other while attached, and the Eley–Rideal (ER) mechanism, where only one reactant is adsorbed and the other reacts with it from the bulk phase. The adsorption of the reactive species changes the electronic distribution of the reactants (as well as that of the catalytic bulk material), introducing an intermediary step into the reaction, lowering the activation energy required for the reaction to occur. The resulting product from the reaction again causes a change in the electronic structure, thus weakening the bond with the catalyst and allowing it to desorb from the surface.

For functional applications of solid-phase heterogeneous catalysts, it is imperative to maximize the surface area where reactions can occur [8], that is, to maximize the number of catalytic interfaces or active sites. This is achieved by utilizing nanoparticles of catalytically active metals such as Pt or Pd, due to their high reactivity when scaled down to the nanometer regime, dispersed throughout a porous and inert supporting matrix, typically made of Al_2O_3 or SiO_2.

As a prerequisite for heterogeneous catalysts to function, the catalytic interfaces cannot be impeded, which can occur if they are exposed to certain environments, such as exposure to a substance that may decrease the catalytic activity of the catalyst, which would then be referred to as surface "poisoning" [3],[17]. In a Langmuir–Hinshelwood-mechanism-based catalyst, which requires two reactants to be present at the catalytic interface, it may occur that only one is present due to imbalances in the reaction mixture, occupying all the active sites and thereby impeding the adsorption of the second reactant; hence, the reactant poisons its own catalyst.

2.1.2 Pt-catalyzed CO-oxidation

CO-oxidation by O_2 is one of the most well-studied catalytic reactions, due to its relevance within the automotive industry, where it is used in three-way catalytic converters to remove toxic CO emissions from exhaust by converting it into CO_2 gas through the following reaction,

$$\mathrm{CO} + \frac{1}{2}\,\mathrm{O_2} \longrightarrow \mathrm{CO_2} \tag{2.1}$$

To facilitate this reaction, Pt-based heterogeneous catalysts are used, owing to their selectivity for CO, robustness at high temperatures, and degradation resistance [18]. Due to the simplicity of the reaction, and the extent to which it has been researched, CO oxidation driven by Pt-based catalysis serves as an excellent benchmark for studying catalytic properties [3],[5]. At higher temperatures the reaction make use of the Langmuir-Hinshelwood-mechanism, where both CO and O_2 are adsorbed onto the catalytic surface, then diffuse across it and react with each other (due to the lowered potential energy of both reactants), and finally desorb as CO_2 gas. See Figure 2.2.

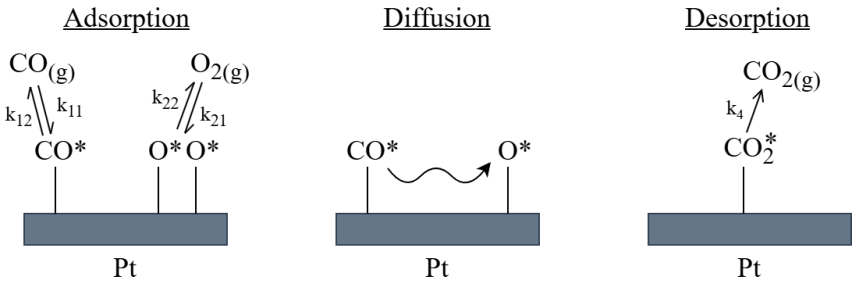

Figure 2.2: Diagram showcasing the three steps of a LH driven CO-oxidation reaction. First the adsorption of CO and O_2 into the catalytic surface, then the diffusion of the species across the catalyst, for them to finally react and desorbing as CO_2.

The reaction can be formulated through a series of intermediary steps. First the adsorption, where CO adsorption associative and O_2 adsorption dissociative (that is splits into two upon adsorption [19], see Figure 2.2),

$$\mathrm{CO_{(g)}} + * \underset{\mathrm{k_{12}}}{\overset{\mathrm{k_{11}}}{\rightleftharpoons}} \mathrm{CO*} \tag{2.2}$$

$$\mathrm{O_{2(g)}} + * \underset{\mathrm{k_{22}}}{\overset{\mathrm{k_{21}}}{\rightleftharpoons}} 2\,\mathrm{O*} \tag{2.3}$$

As the species diffuse across the surface, as seen in Figure 2.2, they may come across each-other leading to the CO-oxidation step.

$$\mathrm{CO*} + \mathrm{O*} \underset{\mathrm{k_{32}}}{\overset{\mathrm{k_{31}}}{\rightleftharpoons}} \mathrm{CO*} + * \tag{2.4}$$

The CO_2 affliction for Pt is very low, leading to the rapid desorbtion in a nonequilibrium step,

$$\mathrm{CO_2*} \xrightarrow[\mathrm{k_4}]{} \mathrm{CO_{2(g)}} + * \tag{2.5}$$

In these reactions, k_{ij} represents the reaction rate constants, related to the speed of the reaction, and $*$ represents the empty catalytic sites. From these reaction steps, it is possible to derive equations describing the time dependency of the surface coverages, θ,

$$\frac{d\theta_{CO}}{dt} = k_{11}\theta_* - k_{12}\theta_{CO} - k_{31}\theta_{CO}\theta_{\mathrm{O}} \tag{2.6}$$

$$\frac{d\theta_{O2}}{dt} = 2k_{21}\theta_*^2 - 2k_{22}\theta_{CO}^2 - k_{31}\theta_{CO}\theta_{\mathrm{O}} \tag{2.7}$$

where θ_{CO} and θ_{O2} are the CO and O_2 surface coverages, respectively, while θ_* is the free-site coverage, defined as $1 - \theta_{CO} - \theta_{O2}$. By assuming steady-state conditions, it is possible to obtain an analytical solution for the rate, r, of CO_2 production from these equations,

$$r_{\mathrm{CO_2}} = k_{31}\theta_{CO}\theta_{O2} \tag{2.8}$$

Equation 2.8 illustrates the strong correlation between the production of CO_2 and the surface coverage of the nanoparticles. Hence, it is of interest to account for effects or circumstances that may affect the surface coverage, such as temperature or partial pressure, when analyzing the catalytic behavior of the CO-oxidation reaction.

CO-poisoning

A known problem associated with CO-oxidation over Pt in three-way catalytic converters is the cold-start problem, where, at low temperatures, CO poisons the catalyst [20]. At lower temperatures, CO has a greater adsorption rate than O_2 and therefore adsorbs more easily onto the catalytic surface. This results in CO occupying all catalytic sites, blocking the adsorption of O_2 and stopping the catalytic reaction. As the temperature increases, the added thermal energy increases the rate constant k_{12}, resulting in an increase in the desorption of CO, thus opening up sites for the adsorption of O_2 and restarting the reaction. For a comprehensive overview of the poisoning process, see Figure 2.3.

Additionally, since O_2 dissociates (that is splits into atomic oxygen) upon adsorption, it requires two neighboring empty sites on the catalytic surface to adsorb [3]. Sites fulfilling this criteria are occupied more quickly than single sites, giving rise to a critical value at which no more O_2 can adsorb, even though the catalytic surface may not be fully covered.

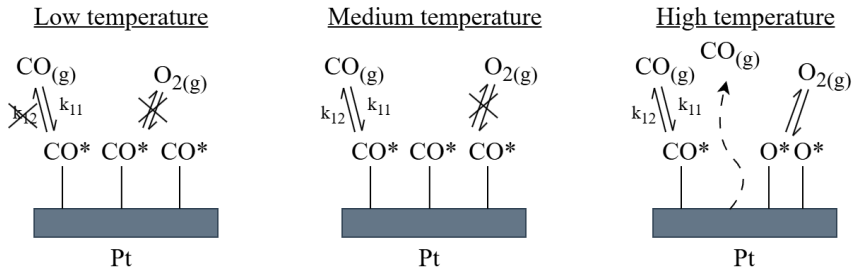

Figure 2.3: Diagram illustrating the CO-poisoning of Pt at different temperatures. At low temperatures the CO desorption rate constant, k_{11} is to small to allow sufficient desorption CO to make room for O_2 adsorption. At medium temperatures k_{11} has increase enough for and equilibrium exchange of adsorbed and desorbed CO, but as O_2 required two empty catalytic sites next to each other to adsorbed it is still insufficient. Finally at high temperatures the k_{11} is large enough for there to be excess catalytic sites for O_2 to adsorb, thus starting the catalytic reaction.

However, due to the exothemicity of the CO - O_2 reaction, additional heat is added to the system allowing the oxidation to be self-sufficient, once it has started, in some systems.

Kinetic phase transitions

Kinetic phase transitions are a type of analogue to normal (thermodynamical) phase transitions, but are instead driven by rate changes and surface coverage rather than thermal equilibrium [19]. Typically, for these types of phase transitions, a critical point can be observed as a result of a temperature or pressure sweep. If the transition occurs rapidly, similar to a step function, it is considered first order, see Figure 2.4a, while if it is a continuous transition, it is considered second order, see Figure 2.4b. Notably, for first-order phase transitions a shift in the position of the critical point

depending on whether the temperature or pressure sweep is performed forwards or backwards; this is called hysteresis. Within the hysteresis a bistable region consisting of a mix of both phases can be observed. See Figure 2.4 for diagrams showcasing first- and second-order phase transitions.

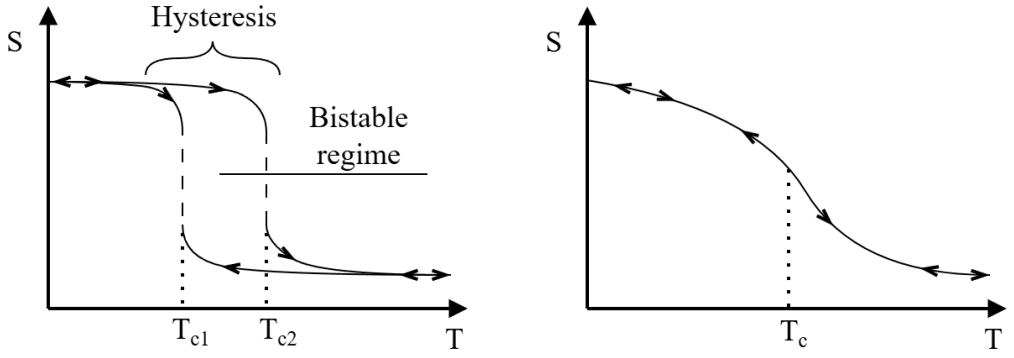

(a) First-order phase transition. **(b)** Second-order phase transition.

Figure 2.4: Graphical representation of first- and second-order kinetic phase transition. With the first-order phase transition displaying its characteristic discontinues change in phase, hysteresis effect, as well as were the critical temperatures would be extracted. The second-order phase transition on the other hand displays its characteristic continuous phase change as well as it's singular critical temperature.

In the case of CO-oxidation, studies of CO poisoning as a function of CO concentration have showcased the existence of a bistable phase region and hysteresis, indicative of a first-order kinetic phase transition [19]. This brings about anisotropy in the way the CO-oxidation reaction behaves depending on whether the reaction is approached from high temperatures/pressures or low ones. As a result, when the reaction is approached from a CO-poisoned surface, a higher oxygen concentration in the mixture is required to achieve catalytic ignition. The opposite is true when starting from an O_2-covered surface.

2.1.3 Characterization of Heterogeneous catalysis

There exists a variety of ways to study catalysts; from exposing a catalyst to different reactant compositions and monitoring the resulting outlet compositions, to the utilization of advanced probing tools to analyze the chemical and structural properties of the catalytic surface as well as its interior [21]. However, each procedure and each catalyst bring about their own challenges. Regarding the characterization of heterogeneous catalysis, two distinct challenges apply: the so-called "pressure gap" and "material gap" [3],[10],[22].

When characterizing solid-phase heterogeneous catalysts, it is typically of specific interest to probe the structural and electronic properties of the catalyst [21]. As these features are often smaller than the wavelength of light, it is common to probe catalysts using electrons going to or emitted from the sample [3]. A plethora of methods exist for utilizing electrons to probe catalysts, such as low-energy electron diffrac-

tion (LEED), Auger electron spectroscopy (AES), and electron beam microscopy. However, using electrons requires the samples to be in UHV; otherwise, the electrons scatter as they interact with molecules in the air, thus distorting the probing [23]. The same problem arises when using other techniques that have historically been used to study catalysts, such as diffraction- and higher-end spectroscopy techniques, where, even though electron beams are not used, UHV is required; otherwise, the signals become too weak and scattered when performed at ambient pressures. For heterogeneous catalysts, typical industrial operating conditions can exceed ambient pressures and are often performed at high temperatures. This renders modeling and laboratory-scale analysis less applicable for industrial applications, as they do not represent actual operating conditions; this is the so-called "pressure gap."

The "material gap", on the other hand, arises as the complexities of real-life catalysts are stripped away during the construction of laboratory models [3],[23]. Industrially used catalysts tend to consist of geometrically complex networks of varyingly sized and shaped nanoparticles within a complex supporting matrix.

Thus, both of these disconnects between industrial and laboratory conditions prevent the direct application of laboratory work to industrial applications. Hence, it is of great interest to study heterogeneous catalysts under operating conditions, that is, *operando*, meaning both at high pressures and temperatures, but also using as realistic representations of the working materials as possible.

To counteract the "pressure gap" and "material gap", advancements, mainly within photon-dependent measurement techniques such as different spectroscopy methods, including UV–Vis spectroscopy, IR spectroscopy, and X-ray diffraction (XRD), were made to enable probing at and above ambient pressures [21]. Additional developments were also made within the field of scanning probe microscopy, allowing for high-pressure scanning tunneling microscopy (STM) [24], as well as within electron beam microscopy, such as the development of environmental transmission electron microscopy (ETEM) [25]. However, a challenge still persists for most of these techniques, as measurements are often performed on arrays of catalytic nanoparticles rather than on individual particles. This results in what are called ensemble-averaging effects [3]. Since nanoparticles often differ significantly from one another, such as in size, shape, and crystallinity, they can therefore exhibit different individual properties within the catalytic array. This information is lost if only the entire array is studied. Thus, to achieve an even more fundamental level of characterization of heterogeneous catalysis, the field of single-particle analysis emerged.

Single-particle analysis for characterization

The field of single-particle analysis developed from the desire to investigate the higher-fidelity properties that individual particles within a catalyst may exhibit but which are lost through ensemble averaging [3]. The characterization of these single-particle dynamics is essential for the development of novel insights regarding catalysts. However, it is also important that techniques for single-particle analysis operate under *operando* conditions while remaining as non-invasive as possible. Utilizing electrons or high-intensity light can damage the nanoparticles and alter their

characteristics during

Some emerging techniques exist, such as ETEM, a modified version of conventional transmission electron microscopy (TEM) that enables microscopy of samples within both gaseous and liquid environments [26], and single-molecule fluorescence microscopy (SMFM), which is an extremely sensitive technique capable of detecting single fluorescent molecules, that is, molecules that emit light when excited, thus allowing monitoring of kinetic behaviors and single-molecule interactions [27]. However, both of these techniques have limitations. ETEM and many similar techniques possess a very high resolution, at the cost of a limited field of view [3], moreover, electron beam-based microscopy can also damage the samples. SMFM, on the other hand, requires either fluorescent reactants or products, which are relatively uncommon. Additionally, SMFM struggles at higher temperatures, which are typical operating conditions for catalysts [27].

Of interest in this thesis is the investigation of so-called nanoplasmonic sensing, a developing non-invasive single-particle technique that works in *operando* conditions. The method relies upon the innate plasmonic behavior of certain metallic nanoparticles to probe the electronic and structural composition of the catalytic surface.

2.2 Nanoplasmonics sensing

Central to the field of nanotechnology is the investigation of how material properties change as systems are scaled down to the nanometer regime (10^{-9} m) [1]. At this scale, the behavior and properties of individual electrons and atoms become increasingly significant, giving rise to new phenomena compared to those of the bulk material.

One important class of properties affected by the downscaling of dimensions to the nanometer regime is that of materials optical properties [28],[29]. The optical properties of a materials comes from how it interacts with visible light, that is, electromagnetic radiation with a wavelength between 400 and 700 nm. As the dimensions of a material are scaled down to be smaller than or comparable to these wavelengths of visible light, the optical properties of that material can change drastically. The study of such light–matter interactions at nanometer scales is referred to as nanophotonics.

2.2.1 Plasmonics

Plasmonics, or nanoplasmonics, is a sub-branch of nanophotonics that focuses on the study and applications of plasmons [28]. A plasmon is a quasi-particle representing the quantization of an electron oscillation (or plasma oscillation) within a material, comparable to how a photon is a quantization of an electromagnetic wave. The mechanisms underlying plasmons are derived from light–matter interactions, either through the more classical and conceptual approach using classical electromagnetism based on Maxwell's equations, or through the more rigorous second quantization approach [30]. Plasmons can exist either in bulk materials or at surfaces, and their behavior strongly depends on the geometry of the system [29]. For the purposes

of this thesis, only localized surface plasmons (LSP) will be considered, that is, plasmons in closed, isolated nanostructures.

LSPs are surface plasmons that arise at metal–dielectric interfaces of closed particles smaller than or comparable to the wavelengths of visible light, such as metallic nanoparticles [29]. From a classical perspective, LSP is an optical phenomenon derived from light interacting with a nanoparticle smaller than the incident wavelength. If the nanoparticle consists of a metal with high electron mobility, that is, a good conductor (such as the noble metals), then as light interacts with the nanoparticle, the electromagnetic wave pulls and pushes the free electron cloud of the nanoparticle in such a way that it begins to oscillate with the frequency of the incident electromagnetic wave, as seen in Figure 2.5. At certain wavelengths, the plasmon oscillations may resonate with the light, known as localized surface plasmon resonance (LSPR). In this case, the nanoparticle begins to scatter the electromagnetic wave that excites it, thus changing the optical properties of the nanoparticle.

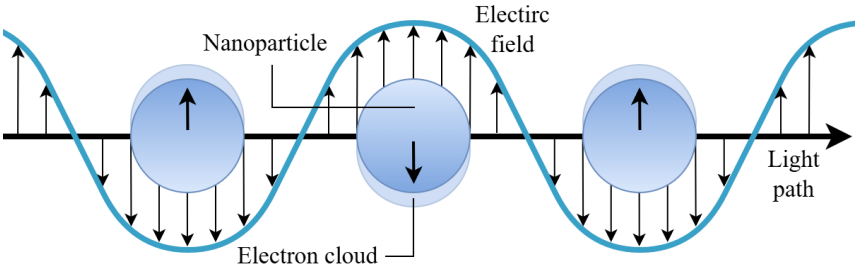

Figure 2.5: A schematic showcase of how LSPR arises as incident light passes over nanoparticles smaller than the wavelength of the light. Utilizing the classical electromagnetic explanation, as the electric field of the light passes over the nanoparticles, it induces movement of the electron cloud within the metallic nanoparticle, which in turn starts to oscillate with the electric field, giving rise to scattering effects.

There are several factors that impact the LSPR response of a nanoparticle, such as particle shape, size, and environmental factors [3],[29],[30]. Of importance to this thesis are the size- and temperature-dependent properties, as well as the oxidation state of the nanoparticle. For qualitative modeling of simple LSPR systems, Mie theory, an analytical solution to Maxwell's equations, is commonly used [3]. However, Mie theory only describes systems where the particles are homogeneous spheres with a radius, r, smaller than the wavelength of the incident light, λ. Still, this is a very powerful analogue that provides an overview of how different properties affect the plasmonic response, but it fails to capture the complete picture, which is often more complex than what the theory can handle.

By approximating the particle as a sphere smaller than the wavelength of the incident light, it can be assumed that the particle is exposed to a uniform electric field, $\overrightarrow{E_0}$, throughout the entire particle. This in turn induces a dipole moment;

$$\vec{P} = \varepsilon_d \alpha \vec{E_0} \tag{2.9}$$

where ε_d is the dielectric function of the surrounding medium and α is the polarizability of the nanoparticle. The polarizability can in turn be described using,

$$\alpha(\omega) = 4\pi r^3 \frac{\varepsilon_m - \varepsilon_d}{\varepsilon_m + 2\varepsilon_d} \tag{2.10}$$

where ε_m is the dielectric function of the nanoparticle metal. To quantify the interaction strength between the incident light and the nanoparticle, the optical cross-section, C, can be used. For a sphere, this cross-section is calculated as,

$$C_{absorption} = k\mathrm{Im}(\alpha(\omega)) = 4\pi k r^3 \mathrm{Im}\left(\frac{\varepsilon_m - \varepsilon_d}{\varepsilon_m + 2\varepsilon_d}\right) \tag{2.11}$$

$$C_{scattering} = \frac{k^4}{6\pi}|\alpha(\omega)|^2 = \frac{8\pi}{3} k^3 r^6 \left|\frac{\varepsilon_m - \varepsilon_d}{\varepsilon_m + 2\varepsilon_d}\right|^2 \tag{2.12}$$

$$C_{extinction} = C_{absorption} + C_{scattering} \tag{2.13}$$

for scattering, absorption, and extinction of light, respectively, where k is the incident light wavenumber, which is given by $k = \frac{2\pi}{\lambda}$. From equations 2.11 and 2.12, it is possible to extract the size-dependent effects of the LSPR. As the scattering scales with r^6 and the absorption scales with r^3, it can be determined that scattering effects dominate for larger particles, thus giving a stronger plasmonic response, while absorption is more prevalent for smaller particles, thus giving a weaker plasmonic response. Size can also cause a redshift of the plasmonic signal. If the nanoparticles are sufficiently large such that the electric field of the incident light can no longer be considered uniform across the whole particle, a retardation effect emerges, thus redshift the plasmonic signal.

As for the temperature dependence of the plasmonic response, it has been shown by O. Yeshchenko et al. [31] that, for Au nanoparticles, an increase in temperature causes a redshift in the plasmonic signal. This is explained as a consequence of three different mechanisms being influenced by the increase in temperature. The first mechanism is an increase in electron–phonon scattering, where a phonon is a second-quantization quasi-particle representative of a quantized wave or vibration throughout a crystal lattice. This increased scattering causes a damping of the plasmonic response, thus redshifting it. The second reason for the redshift is attributed to thermal expansion of the nanoparticles. As the nanoparticle expands, the free-electron density of the nanoparticle decreases, resulting in a lowering of the surface plasmon resonance energy and a redshift of the plasmon wavelength.

The last mechanism causing the redshift, as ascribed by O. Yeshchenko et al., is an increase in the permittivity of the supporting matrix as the temperature increases, that is, in most cases, the permittivity of SiO_2. As the plasmonic response is very

sensitive to the permittivity of the nanoparticle surroundings, an increase in the permittivity of the local environment can cause a redshift in the plasmonic signal.

2.2.2 Nanoplasmoic sensing for characterization of PtNPs

For the characterization of Pt nanoparticles, nanoplasmonic sensing has proven particularly useful. The method relies upon the inherent plasmonic traits that Pt nanoparticles exhibit when exposed to visible light. The plasmonic response for Pt nanoparticles is much weaker than for other nanoparticles [11], such as gold and silver, and has previously been studied using a nearby antenna nanoparticle aimed at enhancing the plasmonic response [32],[33],[34]. However, this type of setup is less desirable, as it does not accurately represent the *operando* environment of a catalyst. Nonetheless, the response remains detectable, although with a more diffuse peak when compared to Au nanoparticles [11].

Of particular interest to this thesis is that nanoplasmonic sensing has previously demonstrated its ability to be applied for single-particle analysis at high pressures and temperatures [12],[35],[36],[37]. As the plasmonic response mainly consists of light within the visible wavelengths, it is rarely prohibited by by gasses at high pressures and temperatures, allowing for excellent *operando* applications [3]. The response is also specific to each individual particle, enabling high-fidelity resolution at the single-particle level. The technique detects and makes use of how the plasmonic response can change as a result of alterations in the local environment, electronic composition, size, shape, and morphology of the particle, thus allowing for an in-depth analysis of individual particles. Additionally, since nanoplasmonic sensing is photon-based, it is an incredibly non-invasive technique.

Specifically, for monitoring the CO-oxidation reaction, nanoplasmonic sensing aims to characterize the kinetic phase changes that occur as the nanoparticles become covered with CO, that is, detecting and analyzing the transition of the nanoparticles from an oxidized to a reduced state [12],[38]. Previous experiments on this have mainly monitored the gas flow and studied how the plasmonic response reacts to different reactant compositions of the inlet flow compared to the outlet flow [3]. To achieve this, a new experimental setup was developed within the Langhammer group utilizing a nanofluidic reactor setup, that is, a nanofluidic system hosting a chemical reaction, both in an effort to emulate the porous nature inside real catalysts used in industrial applications in order to close the “material gap”, but also due to the decreased gas flow allowing for an outlet composition with a larger fraction of products compared to if a larger-scale reactor were used. This allows for the implementation of an extremely sensitive QMS, enabling close monitoring of the outlet flow composition, thus giving insight about the conversion rate of the reaction.

2.3 Nanofluidcs

Nanofluidics is a field dedicated to the study of how fluids behave when constrained within a system containing at least one nanoscale dimension (typically smaller than 100 nm). Similar to the related field of microfluidics, as the dimensions of fluidic

systems are scaled down, new phenomena emerge, such as changes in the effects that electrostatic and intermolecular forces have compared to those in bulk fluids [39]. Forces at phase boundaries also begin to play crucial roles in the fluidic behavior, such as the boundaries between the liquid or gaseous fluid and the solid walls of the nanochannels containing the fluid.

Nanofluidics is a flourishing field with many bioanalytical applications, such as DNA sequencing using fluorescence-based methods in combination with nanochannels to straighten out DNA [40], or for studying extracellular vesicle dynamics [41], but also for more fundamental material analysis applications [39]. The dimensional constraints applied to a nanofluidic system have proven useful in the development of so-called nanoreactors, that is, nanofluidic systems built to host chemical reactions [42]. The nanofluidic setup allows for very precise monitoring of the reactants and resulting products flowing into and out of the system, while also enabling specific targeting of reaction sites.

2.3.1 Nanoreactos and QMS for single-particle analysis

The integration of nanoreactors with nanoplasmonic sensing methods has been motivated by two main reasons. First, the nanoreactor allows for simulation of the nanoporous environment that may be present in certain reactor systems, such as industrially applicable solid-phase heterogeneous catalysts [3]. Therefore, the usage of nanoreactors as a model system allows for a closer analogue to the real system, thus helping to close the "material gap" challenge that is a common problem in many analysis methods dealing with these catalytic systems.

Secondly, the usage of a nanoreactor scales down the volumetric flow of reactants, allowing for a larger contrast in outlet composition between the reactants and the products produced within the reactor. This has proven useful, as it allows pairing with extremely sensitive mass spectrometers, such as QMS, for very precise readings of the mass flow, providing great insight into how the nanoreactor system is affected by different reactant compositions. It is the pairing of nanoreactors with QMS readings that has allowed for parallel reading of outlet composition, thus enabled a more in-depth analysis of nanoplasmonic sensing measurements.

Quadrupole Mass Spectrometry (QMS)

Mass spectrometry is an analytical method that relies on the detection and separation of ionized atoms, with respect to their masses, in order to assess the atomic composition of a sample [3],[43]. The simplest form of mass spectrometry, called time-of-flight mass spectrometry, utilizes the travel time for accelerated ions between two set points to calculate their velocity and, from that, their masses and corresponding ion species from the following equation,

$$v_i = \sqrt{\frac{E_k}{m_i}} = \sqrt{\frac{Uq}{m_i}} \tag{2.14}$$

where v_i and m_i correspond to the ion velocity and mass, respectively, with E_k

representing the kinetic energy, which for an ion with charge q traveling through an electric potential U equals $E_k = Uq$.

QMS is an advanced form of mass spectrometry that utilizes a so-called quadrupole as the mass analyzer unit [43]. Mass spectrometry uses the mass-to-charge ratio of an ion to determine the identity of the ion. To achieve this, the sample is first ionized and then accelerated parallel to the quadrupole, which utilizes an electric field to selectively filter ions with a specific mass-to-charge ratio, which are then detected. Several detection methods exist, with one of the most common being the use of a Faraday cup, which is a conductive cup designed to catch the charged particles and measures the charge carried through it.

2.4 Scanning Electron Microscope (SEM)

SEM is one of the most commonly used electron microscopy techniques for probing and characterizing nanoscale materials [44]. It samples the surface of a material by raster scanning an electron beam over it and detecting the resulting scattering. The electrons from the beam may interact with the atoms of the sample in different ways, allowing for different types of probing. Typically, for topological imaging, secondary electrons or back-scattered electrons are used to create high-resolution images of the sample.

As a result of the electron beam exciting and ejecting inner-shell electrons, it is possible to probe the X-ray emissions created as outer-shell electrons drop down to fill these vacancies. By utilizing these X-ray emissions, it is also possible to characterize the composition of the sample. However, this approach will not be used in this thesis, as SEM will only be used to investigate morphological changes in the nanoparticles.

Chapter 3

Methods

This chapter addresses the experimental setup and methods used to perform the experiments and acquire the nanoplasmonic sensing and structural analysis data, as well as the methods used to process and analyze the data in order to assess the temperature-dependent reaction dynamics.

3.1 Experimental setup

For *operando* characterization of platinum nanoparticles, a gas-phase nanoreactor chip, etched from a SiO_2 substrate, was designed by the Langhammer group before the start of the project. It contained five Pt nanoparticle arrays of varying sizes, each array consisting of nine identically sized particles in a 3×3 arrangement. The particles had a radii of 70, 90, 110, and 130 nm, for each array, respectively, with a spacing between the particles of 3 µm. All arrays were placed on the sample chip as to avoid cross-experimental errors, with a spacing of 40 µm between arrays.

Two microchannels are connected to the nanoreactor. On the inlet side was a U-shaped microchannel fed by the pressure controller unit, while the secondary microchannel was attached to a nanochannel connected to the outlet of the nanoreactor and fed into the QMS, see Figure 3.1. When measurements were performed, a vacuum was pulled over the chip from the QMS side, allowing the U-shaped microchannel to begin feeding the nanoreactor. The nanoreactor was 230 µm long, 20 µm wide, and tapered at the end to an 800 nm-wide outflow channel, as seen in Figure 3.1. The arrays were arranged within the nanoreactor from smallest to largest, with the smallest nanoparticles positioned closest to the inlet, while the largest were positioned closest to the outlet.

The whole chip was enclosed from the top with a transparent glass lid bonded to the underlying substrate. On the back of the chip was a resistive Pt heater allowing for an even temperature gradient and connected temperature reading.

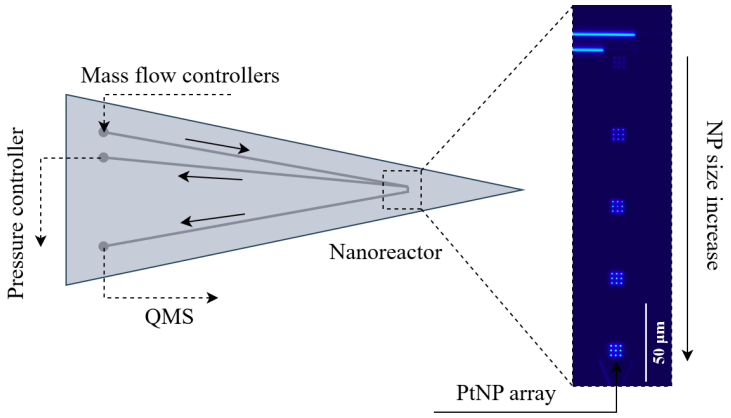

Figure 3.1: Schematic showcasing the nanofluidic-chip, and a image of the nanoreactor as taken by the microscope camera and displayed in the Silx Viewer graphic interface.

The chip was mounted on a specially designed ceramic chip holder featuring a six-contact temperature sensing configuration connected to a Lakeshore 335 temperature controller. The assembly was placed within a dark-field microscope, see Figure 3.2, and connected to a gas flow system.

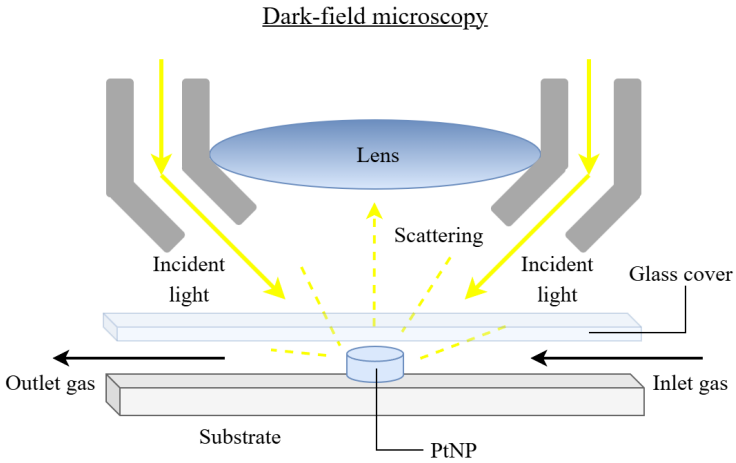

Figure 3.2: A schematic diagram of dark-field microscopy performed on an installed chip containing platinum nanoparticles. The solid yellow lines indicate the incident light illuminating the Pt nanoparticles, while the dotted yellow lines indicate the resulting scattered light, with part of the scattered light entering the microscope setup, i.e., the lens. The diagram also showcases the glass cover of the chip and gas flow present within it.

The gas flow system consisted of mass flow controllers (Bronkhorst), on the inlet side, one for each gas used in the reaction, and a UHV chamber together with a QMS unit (Hiden HAL/3F PIC) on the outlet side. The gas flow control units regulates the inlet flow and gas composition between four gases: Ar, O_2, CO, and H_2, and the mass flow is driven and regulated into the microchannel by a back-pressure regulator connected to the outflow of the microchannel feeding the reactor, see Figure 3.1. For a process flow diagram following the gas-flow see Figure 3.3.

For data collection, an electron-multiplying charge-coupled device (EM-CCD) camera (Andor iXon Ultra 888) was used. Nanoplasmonic sensing imaging was done with the camera mounted to the dark-field microscope in an upright position, while hyperspectral imaging was done with the camera placed in a horizontal position and with a Kurios liquid crystal (LC) filter placed in the beam path between the camera and the sample. This setup allowed for both nanoplasmonic sensing measurements and hyperspectral imaging, with the possibility of monitoring of the reactor output flow composition using the QMS.

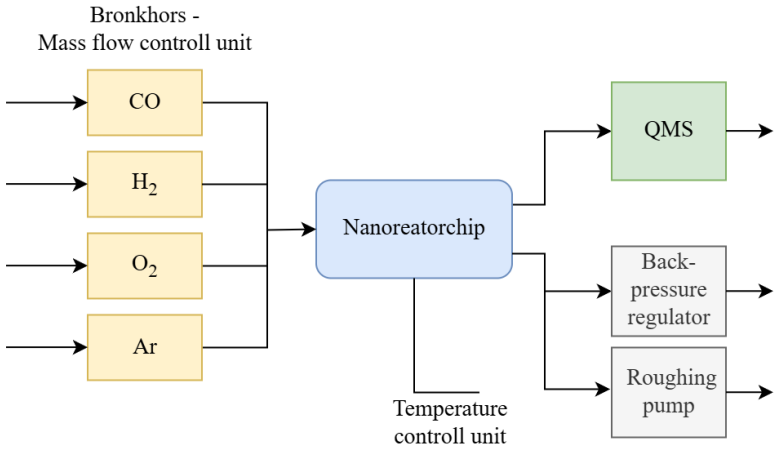

Figure 3.3: Process flow diagram showcasing an overview of the gas flow within the system. The Bronkhorst mass flow units and the assigned gas flows they control are shown in yellow, a black-box depiction of the nanoreactorchip is shown in blue, and the two outlet flows from the chip, as depicted in Figure 3.1, are included: one leading to the QMS in green and the other leading to the back-pressure regulator and roughing pump.

Throughout the experimental procedure, the temperature and gas mixture varied, but a constant pressure of 4 bar was maintained within the chip.

3.1.1 Chip fabrication and preparation

The nanoreactor-chip was designed in the Langhammer group and produced in the MC2 cleanroom facility by J. Fritzsche before the start of this thesis, and a thorough description of the fabrication method is beyond the scope of this thesis.

However, before measurements, the nanoparticles were thermally annealed at 400 °C in 2% H_2 at 1 bar for 20 hours. This was done to facilitate recrystallization of the Pt into a stable state and to relieve residual stresses that may persist as a result of the manufacturing process. Without annealing, the measured nanoplasmonic sensing may exhibit irreversible drift in the data due to thermal restructuring during experiments.

3.2 Experimental procedure

Three experimental procedures were used throughout the duration of this project: nanoplasmonic sensing, hyperspectral imaging, and SEM imaging. The core of this

project was to investigate and characterize the temperature-dependent reaction dynamics using temperature-programmed nanoplasmonic sensing. The characterization was to be performed at different gas compositions and particle sizes by monitoring changes in the plasmonic response as a function of temperature.

Additionally, based on findings from the nanoplasmonic sensing measurements, it became of interest to investigate whether any structural changes in the nanoparticles were induced throughout the measurement process. To do this, nanoplasmonic hyperspectral imaging and SEM imaging were used. As previously mentioned in Section 3.1, both the nanoplasmonic sensing and hyperspectral imaging procedures were performed in the same dark-field microscope, but with different detection configurations, while the SEM imaging, and preparation associated with it, were performed in separate setups.

To investigate and characterize any nanoparticle dynamics as a function of temperature during exposure to CO and O_2, a set of gas compositions was required. In order to avoid introducing too many variables, specific gas compositions were selected. First, a gas composition corresponding to a stoichiometric reactant ratio was used. From Equation 2.1, the stoichiometric ratio can be calculated as 1:0.5 CO to O_2. Additionally, a second reaction ratio of 1:0.25 CO to O_2, representing an O_2-deficient environment, was also investigated. To provide a reference point, gas compositions containing either no CO or no O_2, that is only Ar mixed with either O_2 or CO, were also investigated, with each respective reactant gas flow equivalent to those used in the 1:0.5 ratio experiments.

3.2.1 Nanoplasmonic sensing

In order to run the experiment, a program procedure was first written. A .csv file with the measurement instructions, including stabilization time, temperature (in °C), Ar–, CO–, H_2–, and O_2 flow rates (in mL/min), and the number of image acquisitions, was created. The flow rates were calculated to correspond to the intended gas compositions for each measurement. Since all mass flow controllers were calibrated for Ar flow from the instrument producer (Bronkhorst), some correction factors (found on the Bronkhorst manual) were applied to the mass flows, in order to account for the different physical properties of the gases involved in this thesis. Throughout the experiment, the temperature was ramped up or down. It was during these ramps that the nanoplasmonic sensing measurements were made in the form of image acquisitions of the plasmonic response, hence, the term temperature-programmed.

All nanoplasmonic sensing experiments followed the same program format: first, a stabilization and preemptive reduction phase, where the nanoparticles are reduced in CO, while the temperature was ramped down from 380 to 30 °C, this is done to ensure that all experiments are started with the particles surface in the reduced and CO-poisoned state. This is followed by a temperature sweep in only Ar, that serves to establish a baseline, where pure Ar is flown through the chip during a temperature sweep from 30 to 380 °C. After this an additional, but longer, reduction step in CO is performed from 380 to 30 °C.

The program then move on to the main set of measurements. A constant gas mixture of CO + O_2, at the given gas composition, is flowed through the chip as a temperature cycle from 30 to 380 °C and back again from 380 to 30 °C, is preformed. Two sweeps of the temperature cycle are done in order to monitor the reversibility and reproducibility of the experiment. Finally, the experiment is concluded by flowing Ar in the chip, purging it from CO and CO in preparation for the next experiment. See Figure 3.4 for a visual breakdown of the programmed procedure.

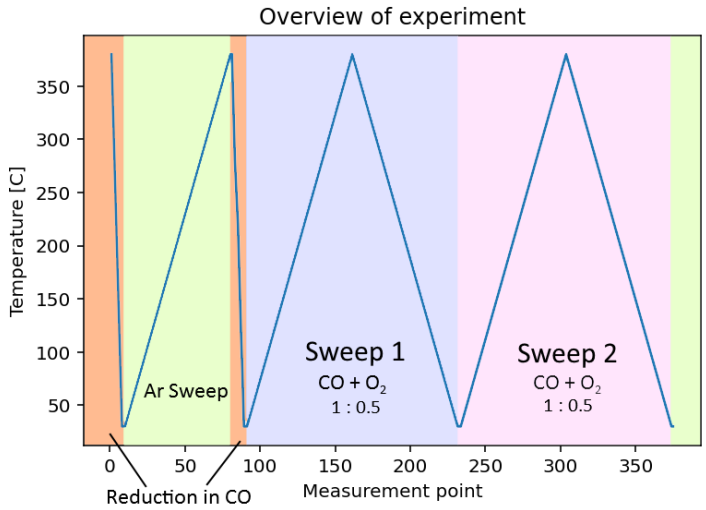

Figure 3.4: A graphical overview of each nanoplasmonic sensing measurement. The y-axis represents temperature as a function of time. The graph is divided into different regions corresponding to the experimental protocol. In orange are the reduction steps, during which only CO and Ar are flowed through the chip in order to reduce the Pt nanoparticles and act as a reset of the experimental conditions. The green region represents the period in which only Ar is flowed through the reactor. The blue and pink regions represent the first and second measurement sweeps, respectively, during which a gas mixture with a specified CO to O_2 composition (shown here as 1:0.5) is flowed through the chip while the temperature is swept from 30 to 380 °C and back down again.

However, it was found during the course of this project that, at lower temperatures ($<$ 50 °C), the temperature control unit provided unreliable readings due to the calibration being effective only in the high-temperature range (50 - 380 °C). This does not invalidate the findings in this thesis since most reaction temperature critical points have been found at temperatures greater than 100 °C.

3.2.2 Structural analysis

Based on findings from the nanoplasmonic sensing data, a decision was made to investigate whether any structural changes of the Pt nanoparticles were present as a response to the environmental exposure the nanoparticles were subjected to. This was achieved by first studying whether the plasmonic spectra changed as a result of the gas flow composition using hyperspectral imaging. For a complementary structural analysis to the hyperspectral imaging, SEM imaging was used.

For SEM imaging, an additional control chip was fabricated, as the main chip is fully enclosed by a glass lid, preventing direct SEM imaging of the nanoparticles. The objective was to monitor how gas exposure could alter the Pt nanoparticle structure; therefore, the control chip was exposed to the same temperature and gas flow history as the main chip in order to replicate any structural changes that may have occurred, with intermediate SEM imaging performed between exposure steps.

Nanoplasmonics hyperspectral imaging

For the hyperspectral imaging, the camera was moved into an alternative configuration which allowed the placements of a LC filter in the light path between the chip and the camera. The LC filter allowed for selective imaging of specific wavelengths scattered by the nanoparticles. The peak wavelength of nanoplasmonic response is size-dependent, but for a fixed nanoparticle size, changes in the plasmonic resonance would correspond to structural and/or morphological changes.

The hyperspectral imaging was performed at ambient temperature with only Ar flowing through the chip, at wavelengths between 470 and 700 nm. However, prior to hyperspectral imaging, the chip was subjected to different gas exposures and temperature cycles. This was done to evaluate whether any structural changes were present and whether such changes were reversible. Hence, the chip was first exposed to a full experimental cycle, containing the same temperature ramps and gas flow, corresponding to a 1:0.5 experiment, as used in measurements pertaining to Figure 3.4, but without any O_2 present, that is, only CO (and Ar), in order to reduce the Pt surface. Subsequently, this was followed by another 1:0.5 experimental cycle, this time without any CO, that is, with only O_2 (and Ar) present. Finally, a second experiment without O_2 was performed to investigate the structural reversibility. Hyperspectral imaging was carried out between each exposure cycle, the results of which are presented in Section 4.2.1. See Figure 3.5 for an overview of the exposure and imaging history.

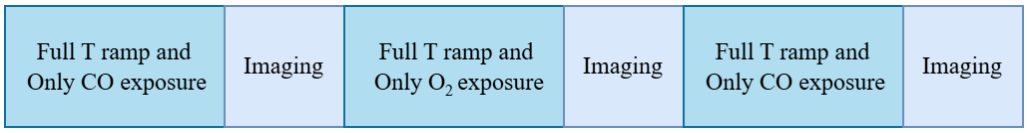

Figure 3.5: A diagram giving an overview of the hyperspectral imaging procedure and the intermittent nanoplasmonic measurements, at a given gas composition, in order to evaluate the impact of the intermittent gas compositions on the nanoparticle structure.

SEM imaging of control samples

As mentioned, due to the chip being enclosed by a glass lid bonded to the substrate, it is not possible to perform SEM imaging of the Pt nanoparticles in this sample, as the electrons cannot pass through the glass. Additionally, the lid cannot be removed once bonded to the chip. Hence, to study structural changes using SEM, a control chip was fabricated. The control sample consisted of a SiO_2/Si substrate with no nanofluidic and no lid. Pt nanoparticle of the same size as in the nanofluidic chip were deposited on such substrate.

To simulate the exposure history of the main chip, the control chip was placed in a so-called "pocket reactor" and exposed to similar conditions of gas compositions and temperature that the nanofluidic chip had experienced during the experiments shown in this thesis. Due to time constraints, only the first few experiments performed on the main chip were able to be replicated on the control chip. Throughout the exposure process, the control chip was sequentially imaged using SEM to monitor structural changes.

3.3 Processing of data

The results acquired from both the nanoplasmonic sensing and the structural analysis measurements were in the form of images, which required pre-processing before further qualitative or quantitative analysis could be performed. The hyperspectral images were pre-processed in the same way since it was based on the same dark field microscope. However, since the SEM measurements were intended to serve as supporting evidence for the structural analysis, no quantitative evaluation was performed, and instead the SEM data was qualitatively evaluated.

The dark-field microscopy data, that is, the nanoplasmonic sensing and hyperspectral imaging measurements, were suitable for both single-particle analysis and larger ensemble analysis of all particles in the same array. The ensemble analysis provided a broader overview of the observed trends, while the single-particle analysis enabled a more detailed investigation of individual particle behavior.

Additionally, a statistical analysis was performed to support the observed dynamics and the characterization derived from the nanoplasmonic measurements. The details and methods of which will be presented at the end of Section 3.3.1.

3.3.1 Dark field microscopy data

The data acquired from the dark-field microscopy consisted of images of the entire nanoreactor, containing all five nanoparticle arrays; see Figure 3.1. Of interest with this image processing was to extract the scattering intensity, corresponding to the pixel brightness, both for each nanoparticle array as a whole, used for ensemble analysis, and for each individual nanoparticle, used for single-particle analysis. For the hyperspectral imaging measurements, the scattering intensity was recorded as a function of the wavelength selected by the LC filter, while for the nanoplasmonic sensing measurements, the intensity would be as a function of temperature.

At each acquisition temperature/wavelength, a number of images were recorder, allowing for a statistical analysis, which will be presented later. For the nanoplasmonic sensing measurements, 25 images were acquired at each temperature point, while 10 images were acquired at each wavelength for the hyperspectral imaging measurements. All images were recorded within a stack had to be aligned before further processing, that is, stabilized, before further processing. To do this an in-house-developed stabilization script was used, which also removed scattering artifacts resulting from scattering at the nanoreactor border. The stabilization was necessary to counteract the thermally induced translation of the chip caused by

heating, which otherwise resulted in misalignment of the images within the stack.

After stabilization, the intensity as a function of temperature or wavelength was extracted using the image-processing software Fiji (ImageJ). The region of interest, corresponding to the full nanoparticle array for ensemble analysis and to a single nanoparticle for single-particle analysis, was marked using the square selection tool. The "Plot Z-axis Profile" function was then used to extract the intensity profile across the image stack. This represented how the intensity of the marked area varies through the image stack as a function of temperature or wavelength. This is also why the images in the stack had to be aligned, as any misalignment would lead to inconsistencies in the z-axis profile as the array/nanoparticle drift in and out of the region of interest.

All intensities at the same temperature step, that is, acquired from the same set of 25 images, were averaged in such a way to obtain one intensity per temperature step. In this way, any intensity extracted from a particle within the stack of images represented the plasmonic response as a function of temperature. Similarly, in the hyperspectral imaging analysis, subsequent intensities at the same wavelength were averaged.

For the nanoplasmonic sensing measurements, the acquired mean intensity across all 25 images, as well as the corresponding standard deviation at each temperature step, was then plotted against temperature, for each array (and later nanoparticle), resulting in the plots shown in Figure 4.1. Similarly, for the 10 hyperspectral imaging measurements, the mean intensities were exacted and plotted as a function of wavelength, resulting in Figure 4.13.

It is important to note that single extreme outliers in the data were omitted after manual review of the data. As the stabilization code used to stack the images on top of each other, in order to extract the "Z-axis Profile", was not designed to stabilize images consisting of several arrays displaying different intensities, extreme mismatches could, in fringe situations, occur. As this was often only present in a single frame, the error was observed as an extreme peak in the standard deviation. After manual review of these outlier frames, the average intensity of the preceding and succeeding frames was calculated and used to replace the outlier. Of the results presented in this thesis, only 5 frames of 9165 from the 1:0.25 dataset were omitted in this way.

Statistical analysis

As mentioned, the acquisition of 25 images at each temperature point allowed for a statistical evaluation of the acquired data. In order to analyze the measurements, different regression models were fitted to the data. This was done in an effort to quantitatively evaluate changes in the intensity, specifically to identify and quantify any inflection points, as these could indicate potential phase transitions and thus correlate with the critical temperature, T_c, of such a transition.

Initially, a lack-of-fit test was considered in order to evaluate how well the models

described the data and to provide insight into the statistical significance of the extracted inflection points, thus strengthening the argument that they possess a real physical meaning. However, owing to the large amount of data, the lack-of-fit test became extremely sensitive to minor discrepancies between the model and the measurements, making it statistically unsuitable.

In order to increase the robustness in the evaluation of the models and in the extracted inflection points, the bootstrap method was used. The bootstrap method works by resampling the data into randomly selected smaller subsets at each data point, and then fitting the regression model to each resampled dataset before evaluating the point of interest using the new model. This procedure is repeated many times until a distribution of predicted values are acquired. If the model type fits the data well, the evaluated points will exhibit only a small spread, but if the model does not fit the data well, the distribution of evaluated points will be more spread out. See Figure 3.6 for a graphical overview of the bootstrap method.

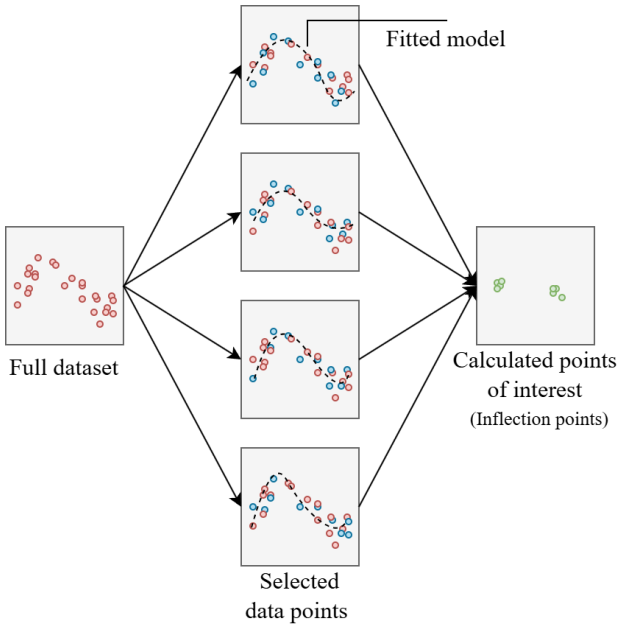

Figure 3.6: A schematic illustration of the bootstrap method. The left plot represents the full dataset (shown in red) containing all measured values. The center plots showcase the resampling and how a subset of values (shown in blue) is randomly selected and used to fit a model. The right plot shows the resulting calculated points of interest (shown in green), which for this thesis correspond to the inflection points, clustered together. A narrow clustering indicates good statistical relevance in both the fitted model and the calculated values.

In the case of this thesis, the resample size consisted of 10 randomly selected intensity values out of the 25 available at each temperature point, with the model being refitted to these points 1000 times. The calculated values that were assessed were the zero points of the second derivative for each model, as these correspond to the inflection points and thus any potential phase transitions. Additionally, to extract

the inflection points, once a distribution of calculated points was obtained, the mean value was calculated together with a corresponding confidence interval.

3.3.2 SEM

As the SEM images are used for a qualitative assessment, very little data processing was performed. The main form of post-processing involved increasing the contrast of surface features of the nanoparticles in order to assess any changes in crystallinity or morphology as the Pt nanoparticles were exposed to the CO and O_2 environments at different temperatures.

The images were processed in Fiji (ImageJ), where the nanoparticles were selected using the circular selection tool and the contrast was enhanced within the selected region. For qualitative analysis, different surface features could have been further examined, for example by evaluating grain size and tracking how it changes as a function of exposure, or through a grain boundary analysis. However, these approaches are beyond the scope of this thesis, with the SEM images instead intended to complement the hyperspectral imaging analysis.

Chapter 4

Results and analysis

In the following chapter, the nanoplasmonic sensing and structural analysis results are presented and analyzed. The temperature-dependent nanoplasmonic sensing data are assessed at both the ensemble and single-particle levels. Both approaches are qualitatively and quantitatively compared across different particle sizes and gas compositions. This is followed by a structural analysis of the nanoparticles based on both hyperspectral imaging and SEM data.

4.1 Nanoplasmonic sensing

The nanoplasmonic sensing analysis is divided into ensemble analysis, in which an entire 3×3 particle array of a given particle size is assessed, and single-particle analysis, in which individual nanoparticles are assessed. Of interest in this thesis is the extraction of the temperature-dependent dynamics, characteristics, and potential kinetic phase transitions, and comparing these between the ensemble and single-particle levels of analysis. Additionally, on both levels of analysis, different gas compositions were compared, with particular focus on the stoichiometric ratio of 1:0.5 ($CO:O_2$) and the CO-deficient reactant mixture of 1:0.25 ($CO:O_2$). Gas compositions containing only O_2 and only CO were also assessed to provide a more comprehensive analysis of the reaction dynamics; see Section 3.2 for a further breakdown of the gas compositions. For each gas composition, two temperature sweeps were performed in succession, from 50 to 380 °C and from 380 to 50 °C; see Section 3.2.1 and Figure 3.4.

In order to extract trends from the otherwise noisy data, curves were fitted to the measurements. As mentioned in Section 3.3.1, the aim of this was to extract critical temperatures, T_c, allowing for quantitative analysis of the kinetic phase transitions. In theory, the inflection points of a curve correctly fitted over a kinetic phase transition would correspond to the critical temperatures of said phase transition. Several methods were tested, as mentioned in Section 3.3.1, to evaluate any inflection points. Initially, fitting a model using a statistical lack-of-fit test was assessed, but due to the large amount of data, this type of test was not suitable for the application. Instead, a bootstrap analysis was performed, as explained in Section 3.3.1, extract

the inflection points. The main analysis was carried out, both on an ensemble and single-particle level, by subtracting the Ar sweep from the measurements in an effort to remove the background and allow for easier fitting of the data.

Additionally, it is worth noting that all these measurements were taken from a chip containing all the nanoparticle arrays to prevent cross-experimental error, so that any potential systematic errors applies to particles of all sizes.

4.1.1 Ensemble analysis

The ensemble data was extracted as described in Section 3.3.1, representing the average intensity of the array, for particles of the same size. At each temperature step, 25 images corresponding to 25 ensemble intensities were acquired, from which a mean intensity and standard deviation were calculated. This was done for each array, that is, for each particle size, and each gas composition. For a gas composition of 1:0.5, the resulting ensemble data for each array can be seen in Figure 4.1.

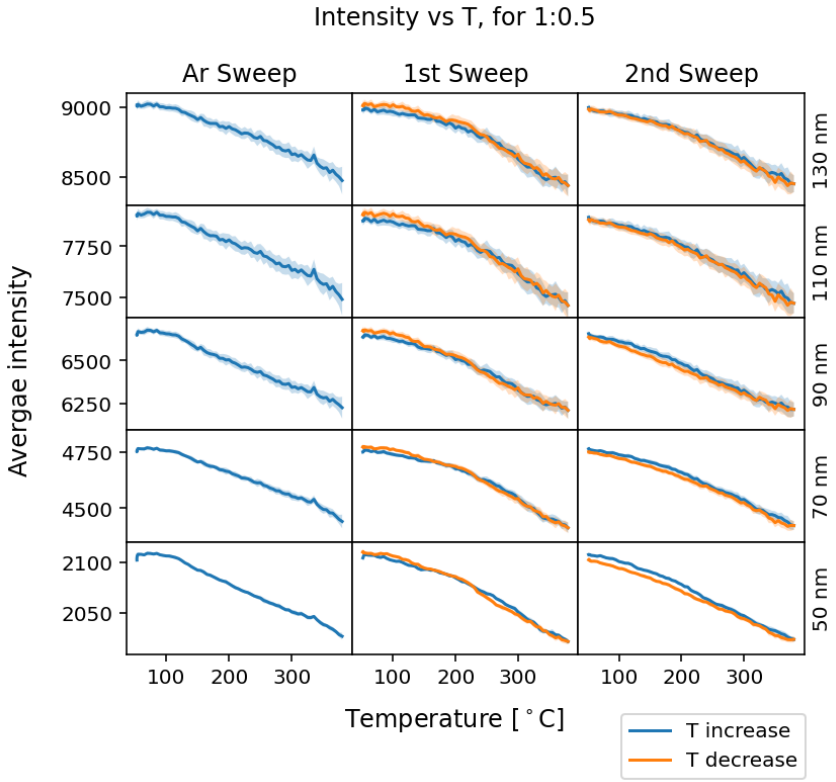

Figure 4.1: Showcases the mean intensity vs the mean temperature for the Ar and two main sweeps, at a stoichiometric gas composition (1:0.5) of CO to O_2, this for each receptive nanoparticle radius, as shown to the right of the plots. In the two main sweeps, displayed in blue is the temperature-increasing part of the sweep, while the temperature-decreasing part is displayed in orange. The shaded area corresponds to the standard deviation derived from 25 consecutive acquisitions at them same temperature.

Figure 4.1 represents a general overview of the nanoplasmonic sensing measurements, displaying the temperature dependence of the plasmonic response. The figure rep-

resents the different measurement regimes (introduced in Section 3.2.1, Figure 3.4) at a gas composition of 1:0.5 ($CO:O_2$): first the Ar sweep, followed by two main measurement sweeps at the set gas composition, while exposed to a full temperature cycle from 50 to 380 °C and back. As mentioned previously, additional gas compositions of 1:0.25, only O_2, and only CO were also measured. Figure 4.1 only represents the 1:0.5 composition, as its purpose is to provide an overview of the nanoplasmonic sensing results and highlight trends that will later be discussed and compared with the datasets obtained for the other gas compositions. Similar complementary plots of Figure 4.1 for the remaining gas compositions can be found in Appendix B.1.

The nanoplasmonic sensing measurements, as presented in Figure 4.1 and the corresponding figures in Appendix B.1, were analyzed from two key perspectives. First being; general trends present in the measurement data, regardless of the gas environment, and the second being; dynamics arising from the presence of the reactants, with the aim of quantitatively characterizing the size- and temperature-dependent behavior derived by the reaction environment. For the analysis of the general trends, focus is placed on the Ar measurement sweeps, with observed trends consisting of thermally and/or size-dependent properties that persist throughout each measurement. For the analysis of the reactant-derived dynamics, focus instead lies on the two main measurement sweeps. These dynamics are not as general as the previously mentioned trends and are instead highly dependent on the gas composition. Furthermore, these dynamics are harder to make out from the data as presented in Figure 4.1 and require additional data treatment or alternative ways of presenting the data.

Derived from the data presented in Figure 4.1, as well as in Appendix B.1, three general trends were identified. First, and most notably, a decreasing intensity of the nanoplasmonic response is observed as the temperature increases, and vice versa, an increasing intensity is observed as the temperature decreases. This is the dominant thermally induced dynamic in the measurements, clearly present in the Ar sweep and persisting throughout each of the main measurement sweeps. Moreover, this trend is observed for all other gas compositions in Appendix B.1 and likely arises from electron–phonon interactions. As the temperature increases, the phonon population inside the nanoparticles increases, resulting in enhanced electron–phonon scattering. Such scattering reduces the mobility of electrons within the nanoparticle, leading to a damping of the collective electron oscillations and thus to a weaker LSPR response and reduced plasmonic scattering. In the Ar measurement sweep, that is, in the absence of reaction-induced dynamics, this effect is expected to be approximately linear, a behavior that can be observed in the Ar sweeps for temperatures above 100 °C.

The two additional general trends are; first, an decrease in plasmonic response with decreasing nanoparticle size. This is a well-established characteristic of plasmonic nanoparticles, with the underlying theory presented in Section 2.2.1. The second trend being that the standard deviation appears to decrease with decreasing nanoparticle size, which is highly unanticipated. A possible explanation, discussed further in Section 4.2, is that the effect is related to structural differences between

the nanoparticles. As shown by the SEM images in Figure 4.16, smaller nanoparticles consist of fewer grains, when compered to the larger ones in Figure 4.15. This simpler microstructure may give rise to more uniform plasmonic responses, resulting in the smaller standard deviations observed.

Investigating the reactant-derived dynamics, two main points of interest could be derived from the two main measurement sweeps in Figure 4.1. The first dynamic to note is that, for both the first sweep and second sweep, a drift in intensity between the start and end points of each temperature sweep can be observed. That is, the intensity does not return to its initial value as the temperature increases and then decreases, therefore, the intensity at 50 °C differs between the beginning and the end of each respective sweep. Based on this observation, it became of interest to investigate any structural changes of the nanoparticles that may occur as they are exposed to CO and/or O_2 at the given temperatures, as this could explain this anomalous behavior. However, it has previously been shown that the addition of O_2 at higher temperatures has resulted in structural changes in Pt nanoparticles [45]. Thus, a structural analysis was conducted, as described in Section 3.2.2, with results reported in Section 4.2. For a further illustration of the reported drift, see Appendix C, where a comparison of the drift between gas compositions is reported but not used in any further analysis.

The second point of interest concerns the effect that the addition of CO and O_2, and the subsequent CO oxidation over the Pt nanoparticles, has on the plasmonic response as a function of temperature. Of specific interest is the identification and characterization of any kinetic phase transitions that may occur during heating and cooling, as well as the comparison of these transitions between differently sized nanoparticles and under different CO and O_2 gas compositions. Traditionally, kinetic phase transitions are highly substrate- and size-dependent. A possible first-order phase transition for Pt nanoparticles with a size of around 60 nm on a SiO_2 substrate has been reported at approximately 200 °C [12], while Pt bulk-facilitated CO-oxidation has been reported to have ignition temperatures between 350 and 460 °C [46]. These transitions are attributed to the transition between the CO-poisoned and active states of the Pt nanoparticles.

The following section aims to investigate and compare the previously mentioned characterization of any kinetic phase transitions and qualitatively and quantitatively assess the impact that the gas composition has on the temperature- and size-dependent plasmonic response.

Characterization of the plasmonic response

To investigate the impact of gas composition and particle size on the plasmonic response, it is of interest to quantitatively evaluate any critical temperature corresponding to a kinetic phase transition and characterize the dynamics that arise in the presence of the reactants. To isolate the plasmonic response induced by the reactants, the Ar measurements (see Figure 4.1) representing the temperature-dependent plasmonic response of thoroughly CO-poisoned nanoparticles, were subtracted from the main measurements. For gas compositions containing a sufficiently high O_2 con-

centration, distinct kinetic phase transitions were expected to manifest as distinct changes in the plasmonic response

For the evaluation of the phase transitions, fourth-degree polynomials were fitted to the data, where the potential critical temperatures of the phase transitions correspond to the inflection points of the fitted curves. See Section 3.3.1 under *Statistical analysis* for further inquirer regarding this approach, as well as Figure 2.4 for a reference to the critical temperature of a phase transition. The Ar measurements were subtracted from each of the gas compositions, with Figure 4.2, representing the 1:0.5 and 1:0.25 measurements, and Figure 4.3, representing the only CO and only O_2 measurements.

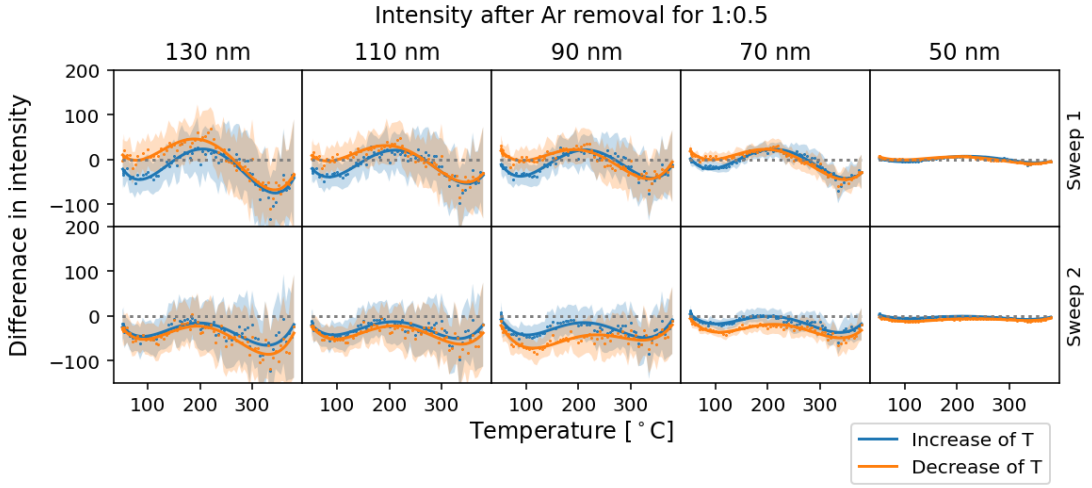

(a) 1:0.5 composition.

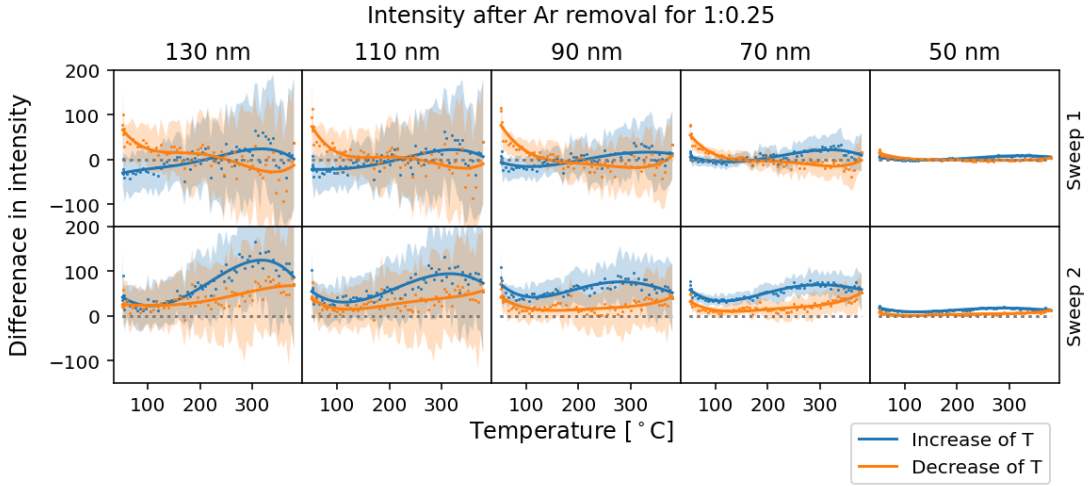

(b) 1:0.25 composition.

Figure 4.2: Plots showcasing fourth-degree polynomials (solid lines) for both main sweeps, fitted to the mean plasmonic response (dots) at each temperature step, with the corresponding Ar sweep subtracted. Two gas compositions are displayed: **(a)** 1:0.5 and **(b)** 1:0.25. The shaded areas represent the standard deviation after removing the Ar background.

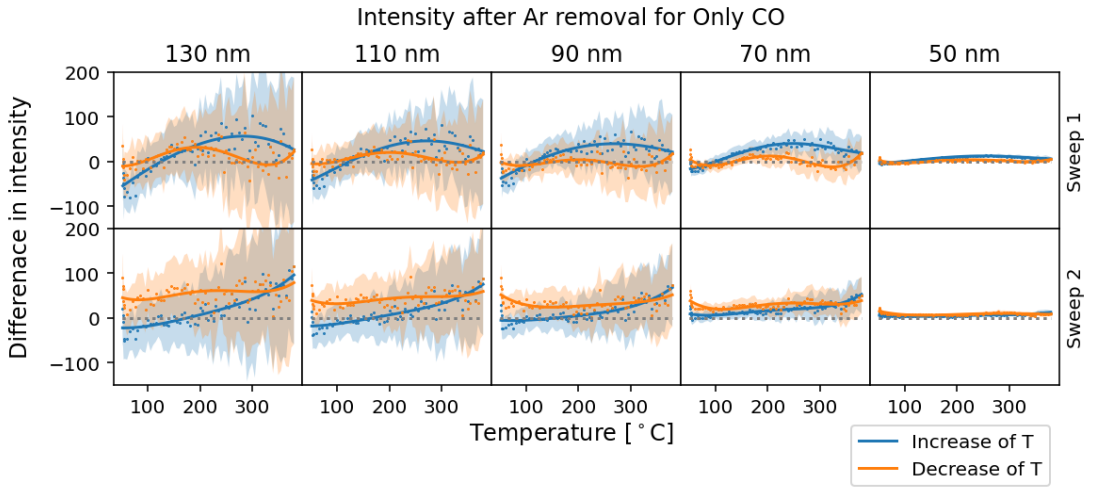

(a) Only CO composition.

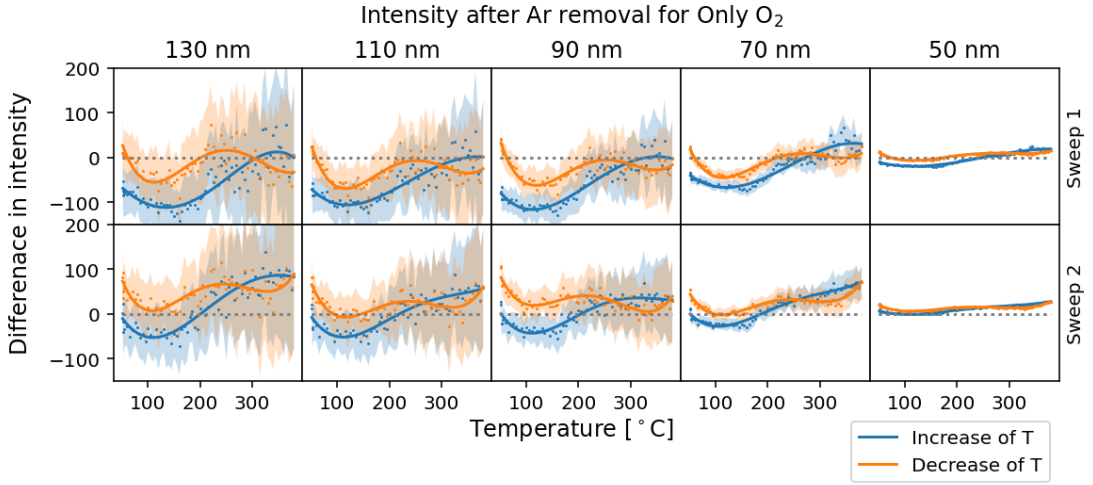

(b) Only O_2 composition.

Figure 4.3: Plots showcasing fourth-degree polynomials (solid lines) for both main sweeps, fitted to the mean plasmonic response (dots) at each temperature step, with the corresponding Ar sweep subtracted. Two gas compositions are displayed: **(a)** only CO and **(b)** only O_2. The shaded areas represent the standard deviation after removing the Ar background.

Several methods were evaluated to fit the data presented in Figure 4.2 and Figure 4.3. The aim of fitting the data with a model was to highlight trends, allowing for a qualitative assessment of the data, but also to extract potential inflection points, which could correspond to the critical temperatures of kinetic phase transitions, in order to enabling a quantitative analysis and investigation of the underlying dynamics. The complex responses, which will be addressed in the following qualitative analysis, as well as the clear differences between datasets, made it difficult to fit a single general model. Initially, a sigmoidal model was tested, as this is commonly used when studying phase transitions, but this method was highly sensitive to the chosen fitting boundaries and resulted in cherry-picking boundaries to achieve any

fit. Additionally, this approach failed for some gas compositions and could only describe one transition at a time, where as the data in Figure 4.2 and 4.3 indicated several possible transitions. Transitions which will also be further assessed in the qualitative analysis.

Fitting the data with cubic splines was also attempted. This approach was robust and flexible, but produced a large number of inflection points due to overfitting the data. Attempts to negate this by increasing smoothness resulted instead in underfitting crucial features.

Finally, a fourth-degree polynomial was fitted to the data. The main limitation of polynomial fitting is the sensitivity of the inflection points, meaning that small deviations in the data can significantly affect the extracted critical points. However, due to its robustness and simplicity, it was chosen as the model of choice. Higher-order polynomials were also considered, but based on the qualitative evaluation of the 1:0.5 data, in which phase transitions were most likely to express themselves, a fourth-degree polynomial was chosen. To keep the analysis consistent between gas compositions, fourth-degree polynomials were also used to fit these datasets as no major deviations in fitting was observed.

Qualitative characterization

Before addressing a quantitative evaluation of the fitted data, a qualitative assessment was made. As seen in Figure 4.2 and Figure 4.3, clear differences in response between gas compositions can be observed, with the data displaying unexpected result. Starting with the 1:0.5 gas compositions, a single phase transition, corresponding to a decrease in plasmonic response as the Pt nanoparticles transition from their reduced, more metallic-like, CO-poisoned state to their oxidized active state, was expected. However, two potential phase transitions appear to be present: a lower-temperature transition around 150 °C and a higher-temperature transition at approximately 280 °C.

As mentioned in Section 4.1.1, a high-temperature phase transition is likely to exist for particles of these sizes between approximately 200 °C [12] and 460 °C [46], which possibly corresponds to the 280 °C transition observed in Figure 4.2a. However, a secondary lower-temperature transition and subsequent lower-temperature phase are not accounted for in previous literature. Comparing the different gas compositions, the higher-temperature transition is absent from the only CO and 1:0.25 measurements, while the lower-temperature transition is present for all gas compositions. If the higher-temperature phase transition is the previous mentioned transitions from CO-poisoned to active state, then the absence of the higher-temperature transition in the only CO measurements is expected due to the lack of O_2. Which further supports the notion that the high-temperature transition, in the 1:0.5 measurements, being a real phase transition. The presence of the lower-temperature transition in the only CO measurements, also indicate that it is not a real phase transition. Additionally, the absence of the higher-temperature phase transition in the 1:0.25 measurements could suggest that the O_2 concentration is too low to induce a phase transition at temperatures below 380 °C at this concentration.

Furthermore, when assessing the only CO measurements, additional anomalous behavior can be observed. The main point of interest is that the only CO measurements should closely resemble the Ar measurements, as the Ar measurements consist of fully CO-poisoned nanoparticles with Ar flowing through the reactor, while the only CO measurements also consist of fully CO-poisoned nanoparticles, but with CO diluted with Ar flowing through the reactor instead. Therefore, it was expected that subtracting the Ar measurements from the main measurements would result in a flat line centered around zero. Yet, as observed in Figure 4.3a, the response is not just non-zero but also, as previously mentioned, possessing a low temperature phase transition. For further inquiry regarding this, the following plots were made, representing the second sweep of the main measurements overlaid with the corresponding Ar measurements for nanoparticles with a radius of 130 nm, for each gas composition. The second sweeps are assessed, as these measurements seemingly exhibit more stable dynamics, with these nanoparticles having already been exposed to the reactant gas mixture, thus being more representative of a catalyst in *operando* conditions.

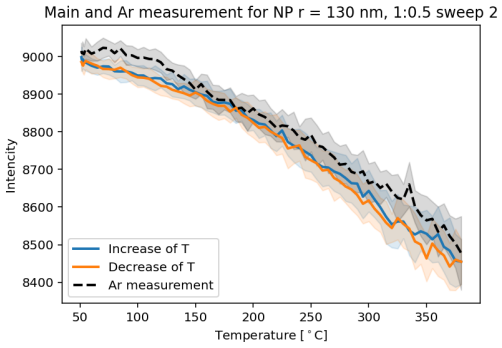

(a) The 1:0.5 gas composition.

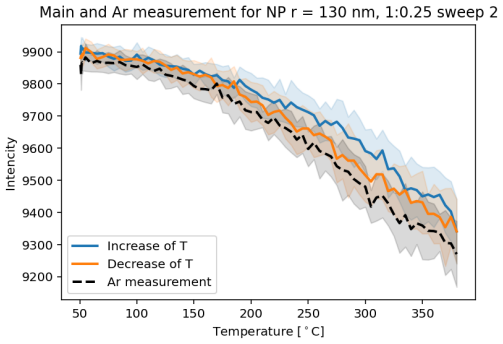

(b) The 1:0.25 gas composition.

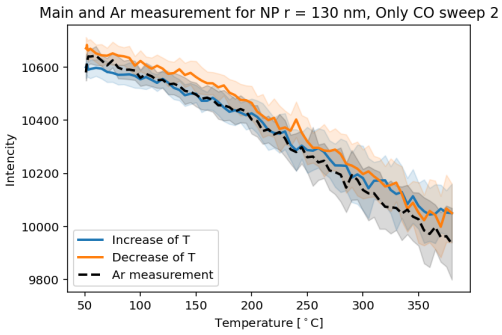

(c) The only CO gas composition.

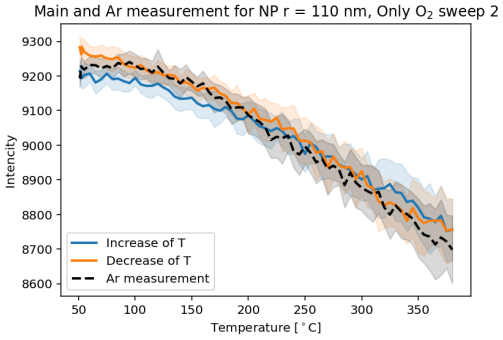

(d) The only O_2 gas composition.

Figure 4.4: Showcases the mean intensity vs mean temperature, similar to Figure 4.1, with the Ar sweep (the black dashed line) overlaid on the second sweep measurements. Displayed in blue and orange are the temperature-increasing and temperature-decreasing parts of the sweep cycle, respectively, for the particles with a radius of 130 nm. The shaded area represents the standard deviation of the plotted mean intensity. Each plot represents a different gas composition, with **(a)** being 1:0.5 ($CO:O_2$), **(b)** being 1:0.25, **(c)** only CO, and **(d)** only O_2.

From Figure 4.4, two points of note becomes evident. First, the lower-temperature transitions appears to be an artifact brought about by a sudden and increased response in the low-temperature regime of the Ar measurement, rather then a change in the main measurement. This is most evident in the 1:0.5 measurement presented in Figure 4.4a. This could indicate some form of temperature-dependent but gas-independent transition in the nanoparticles, or it maybe a measurement artifact. As stated in Section 3.2.1, the temperature control unit never measured temperatures below 50 °C, even though the sample was at ambient temperature, most likely due to a lack of calibration after changing to the chip used in this project. This lower-temperature artifact may thus be an additional error introduced by the inadequate calibration.

The second point of note is that the inclusion of the Ar measurements further highlights and supports the notion discussed in Section 4.1.1, that a drift is present in the system. As this drift is most prevalent in the only CO and 1:0.5 measurements, it may indicate that whatever is causing it could be O_2-independent. Perhaps, in the reduced state, the Pt nanoparticles are more prone to temperature-dependent reconstruction, however, O_2-induced structural changes, such as sintering, are well reported in Pt nanoparticles [45],[47], although often at temperatures above 400 to 600 °C. These results further underline the need for a structural analysis, which was conducted and reported in Section 4.2.

Perhaps the deviation from the Ar measurement in both of these measurements, which is responsible for the non-zero centering discussed when assessing Figure 4.3a, could be induced by a change in the plasmonic response based on the medium surrounding the nanoparticles. As presented in the theory, Section 2.2.1, the nanoplasmonic response is highly sensitive to the medium surrounding the particles, and perhaps the introduction of CO into the Ar flow increases the plasmonic response even for already CO-poisoned nanoparticles.

Quantitative characterization

Moving on to the quantitative analysis, this section aims to evaluate potential phase transitions and, through the characterization of these, generate further insight into the dynamics of the systems.

As presented when introducing Figure 4.2 and Figure 4.3, after subtracting the Ar measurement from the main measurements, the resulting data were fitted with fourth-degree polynomials. The following analysis aims to statistically evaluate the inflection points obtained from this fitting in order to validate potential critical temperatures representing a phase transition. A lack-of-fit test was initially considered, however, due to the large number of data points, the lack-of-fit test proved to be too sensitive and did not provide any useful statistical insights. Hence, it was replaced by the bootstrap approach, as described in Section 3.3.1 under *Statistical analysis*. This method relies upon resampling the data points, with replacement, at each temperature step into a randomly selected subset of points, which for this thesis consisted of 10 randomly selected intensity values out of 25 at each temperature step, calculating the mean of the resampled dataset, and fitting a selected

model to those means. This process was repeated 1000 times, with the inflection points extracted for each fitted model and used to produce the distributions shown in Figure 4.5 and Figure 4.6.

Since the aim of this analysis is to evaluate potential critical temperatures, the absolute values on the y-axis are of little importance. Thus, the intensity data were normalized using the z-score for better clustering of y-values, allowing for ease of comparison.

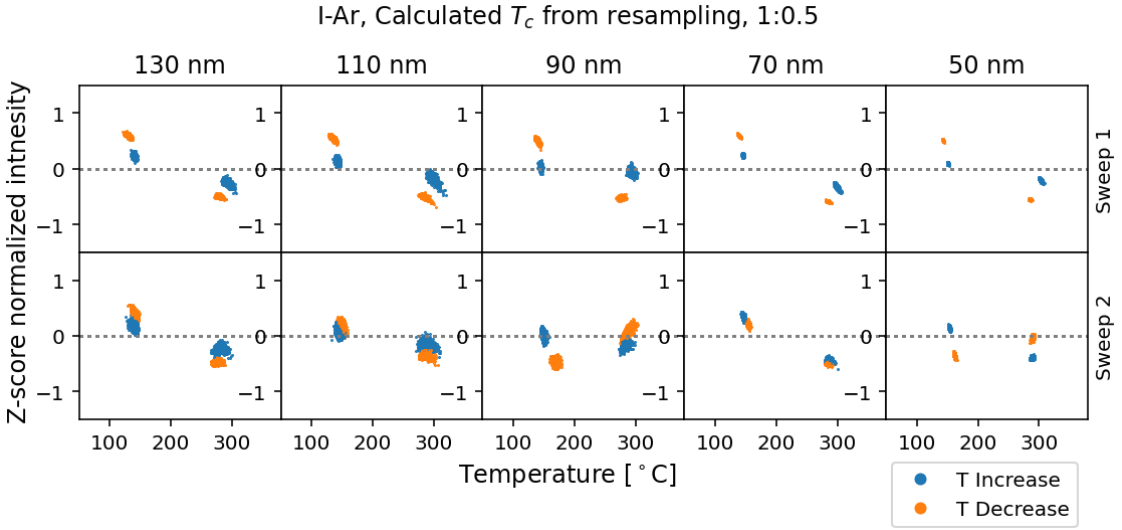

(a) 1:0.5 ratio.

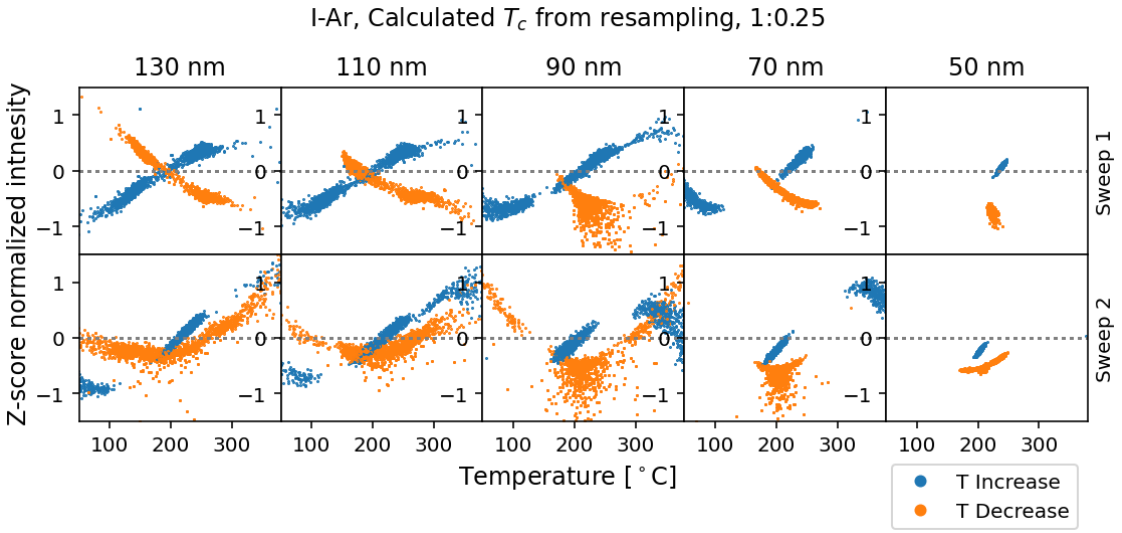

(b) 1:0.25 ratio.

Figure 4.5: Plots showcasing bootstrap approach for fourth-degree polynomials at gas compositions 1:0.5 and 1:0.25, the calculated inflection-points for both temperature increase and decease of each sweep. When the data is closely bundled then that correlates to a good statistical value for the model, while spread points correlates to a poor statistical value of the model.

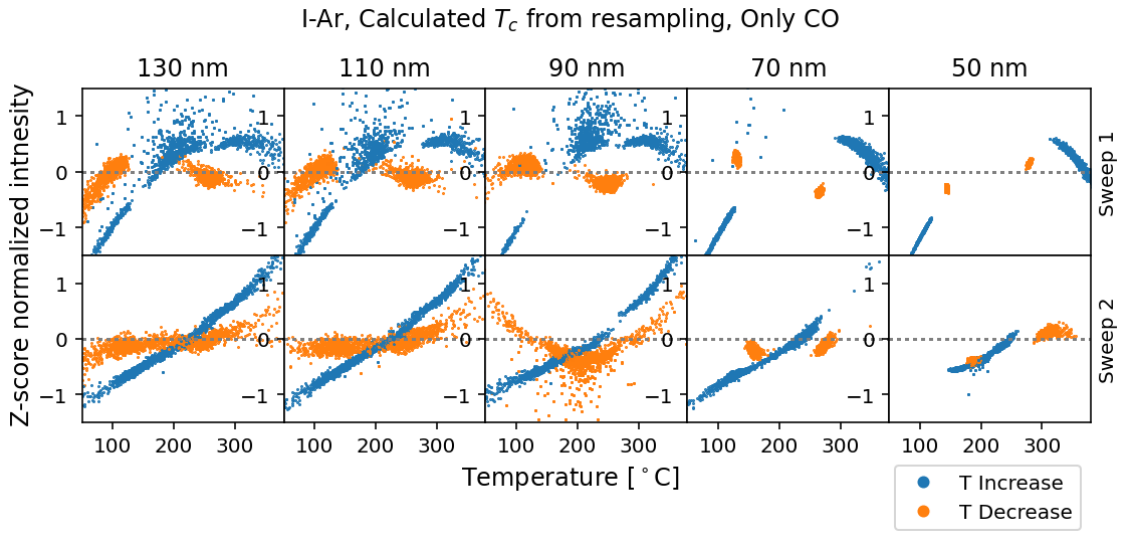

(a) Only CO.

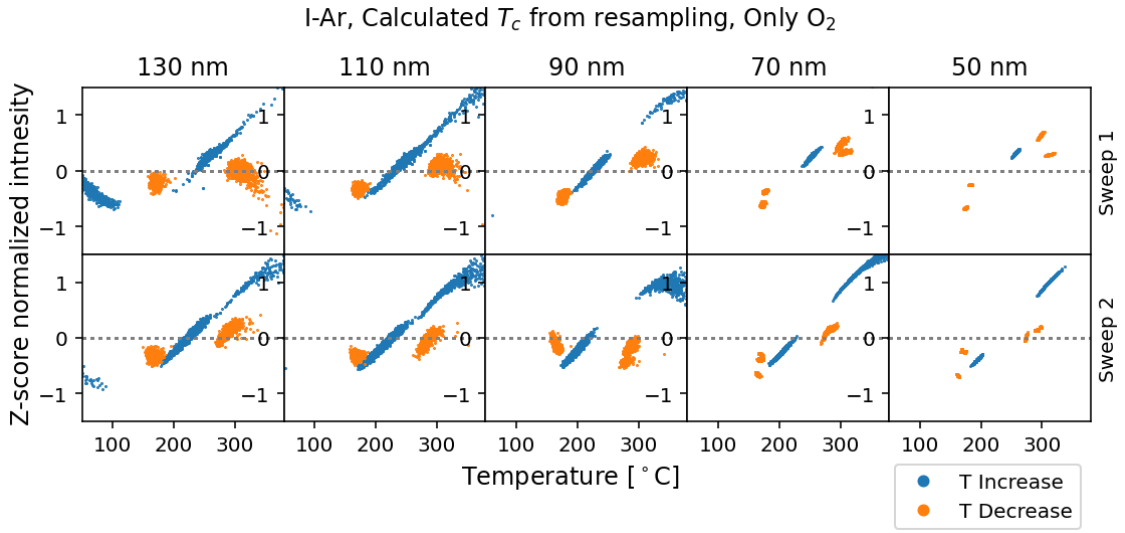

(b) Only O_2.

Figure 4.6: Plots showcasing bootstrap approach for fourth-degree polynomials at gas compositions only O_2 and only CO, the calculated inflection-points for both temperature increase and decease of each sweep. When the data is closely bundled then that correlates to a good statistical value for the model, while spread points correlates to a poor statistical value of the model.

As previously mentioned, a smoothing cubic spline was also considered for fitting the data. Contained within Appendix B.2 is the inflection point distribution, evaluated using the same bootstrap approach used when assessing the fourth-degree polynomial, but applied to a cubic spline, in order to further highlight how unsuitable this model is for identifying and evaluating potential critical temperatures.

From Figure 4.5 and Figure 4.6, it is possible to evaluate the quality of the inflection points obtained from the fitted model. The clustering of the bootstrap-derived inflection points along the x-axis indicates stable inflection points, suggesting that the identified inflection points may correspond to real physical properties, such as critical temperatures. Starting with the 1:0.5 gas ratio presented in Figure 4.5a, the relatively small spread of both bootstrap-derived inflection points in both sweeps could indicate that they represent real physical phenomena. Furthermore, the only O_2 measurements, in Figure 4.6b, showcase some clustering of the evaluated inflection points for the temperature-decreasing part of the sweep cycle, but none for the temperature-increasing part, indicating potentially unstable phase transitions. An unstable transitions was expected from the qualitative analysis and is possibly due to the O_2 in the gas reacting with the CO covering the nanoparticles. However, these transitions would likely drift and diminish if additional sweeps were performed, as the nanoparticel become progressively more oxidized and the CO covering the nanoparticles is consumed.

However, for the 1:0.25 ratio and only CO measurements, Figure 4.5b and Figure 4.6a, respectively, a greater spread of bootstrap-derived inflection points can be observed, indicating a poorer model fit and suggesting that the evaluated inflection points may not correspond to any real physical properties. As discussed in the qualitative assessment, this was expected for the only CO measurements, as the absence of O_2 would not induce a phase transition between the CO-poisoned and active states of the Pt nanoparticles. For the 1:0.25 measurements, the greater spread in bootstrap-derived inflection points likely indicated an insufficient O_2 concentration for the reaction to occur, as derived in the qualitative evaluation of 1:0.25 measurements. For a more conclusive assessment of the effect O_2 concentration has on the temperature-dependent dynamics, future experiments could introduce more intermediate O_2 concentration steps between gas compositions of 1:0.5 and 1:0.25.

Assessing the lower-temperature phase transition, starting with the qualitative analysis, where it was proposed that the lower-temperature inflection point may not represent a reactant-induced phase transition. As seen in Figure 4.2 and Figure 4.3, the lower-temperature inflection point is present for each gas composition, even the only CO measurements, which completely lack the presence of O_2. Thus, this lower-temperature transition was considered to potentially represent a measurement artifact or a CO-induced transition. Yet, as shown in the quantitative assessment, this inflection point is stable in the 1:0.5 measurements when evaluated using the bootstrap approach, presented in Figure 4.5a, while it is unstable in the only CO measurements, presented in Figure 4.6a. This could indicate that the fourth-degree polynomial is not a sufficient fit for the only CO data, but it could also indicate that no transition is present within this dataset, thus suggesting that the lower-temperature transition is, in fact, reactant dependent.

To help determine whether the observed lower-temperature transition is a real kinetic phase transition, a structural change within the particles, or a measurement/data-treatment artifact, further analysis is required. A first step for a conclusive assessment would be using other single-particle *operando* measurement techniques,

such as ETEM, which is capable of directly probing both the plasmonic and electronic properties of the catalyst. However, if the lower-temperature transition is shown not to correspond to a real phenomenon, but instead is caused by a measurement or data-treatment error, alternative data-treatment methods should first be considered, with the aim of accentuating the real phase transitions while mitigating artifacts. If the artifact is not caused by the data-treatment method, and the lower-temperature transition persists in future temperature-dependent measurements, then this could indicate that the current nanoplasmonic sensing setup may not be suitable for lower-temperature measurements, possibly due to inadequate calibration, as previously discussed. Additional analysis of the lower-temperature transition will be conducted at the single-particle level, presented in Section 4.1.2.

Continuing with the analysis of Figure 4.5 and Figure 4.6, it is worth noting that, for all gas compositions, a decrease in particle size corresponds to more clustered bootstrap-derived inflection points. This is could possible be due to the same reason that the standard deviation appears to decrease with particle size, as presented in Section 4.1.1.

Moving on to assessing potential size-dependent dynamics of the bootstrap-derived inflection points. Treating the derived inflection points as critical temperatures, the mean critical temperatures and corresponding 95% confidence intervals for each gas composition, sweep, and particle size were calculated. Reported in Table 4.1 and Table 4.2 are the derived critical temperatures and confidence intervals for both transitions of the 1:0.5 measurements, as the following analysis of the dynamics will focus on these measurements. The results for the other gas compositions can be found in Appendix B.3.

	Sweep 1							
	Up T_1		Down T_1		Up T_2		Down T_2	
NP [nm]	T_c	C.I.	T_c	C.I.	T_c	C.I.	T_c	C.I.
130	140.41	±0.11	130.91	±0.15	292.26	±0.23	278.70	±0.16
110	142.59	±0.11	136.09	±0.15	298.04	±0.31	284.66	±0.23
90	145.02	±0.09	140.54	±0.12	292.62	±0.19	275.72	±0.15
70	145.94	±0.05	139.72	±0.06	299.84	±0.14	284.86	±0.10
50	151.15	±0.03	143.30	±0.04	303.14	±0.08	285.32	±0.05

Table 4.1: Table of mean critical temperatures, and their respective 95% confident intervals (C.I.), calculated from the bootstrap-derived inflection points presented in Figure 4.5a. Listed are both evaluated critical temperatures (with the lower T_c presented as T_1 and the upper T_c as T_2), for both the temperature-increasing and temperature-decreasing parts of the first measurement sweep, at a gas composition of 1:0.5.

	Sweep 2							
	Up T_1		Down T_1		Up T_2		Down T_2	
NP [nm]	T_c	C.I.	T_c	C.I.	T_c	C.I.	T_c	C.I.
130	139.29	±0.19	140.56	±0.15	279.14	±0.29	275.06	±0.21
110	144.24	±0.17	150.06	±0.15	285.51	±0.37	286.33	±0.30
90	149.30	±0.13	168.32	±0.22	282.67	±0.24	286.41	±0.31
70	146.25	±0.08	154.47	±0.08	286.98	±0.17	286.08	±0.15
50	153.76	±0.05	162.18	±0.05	288.56	±0.09	288.83	±0.08

Table 4.2: Table of mean critical temperatures, and their respective 95% confident intervals (C.I.), calculated from the bootstrap-derived inflection points presented in Figure 4.5a. Listed are both evaluated critical temperatures (with the lower T_c presented as T_1 and the upper T_c as T_2), for both the temperature-increasing and temperature-decreasing parts of the second measurement sweep, at a gas composition of 1:0.5.

For a quantitative analysis of the size-dependent dynamics, the first sweep of both the upper and lower critical temperatures, as reported in Table 4.1, were plotted against the nanoparticle radius. This resulted in Figure 4.7.

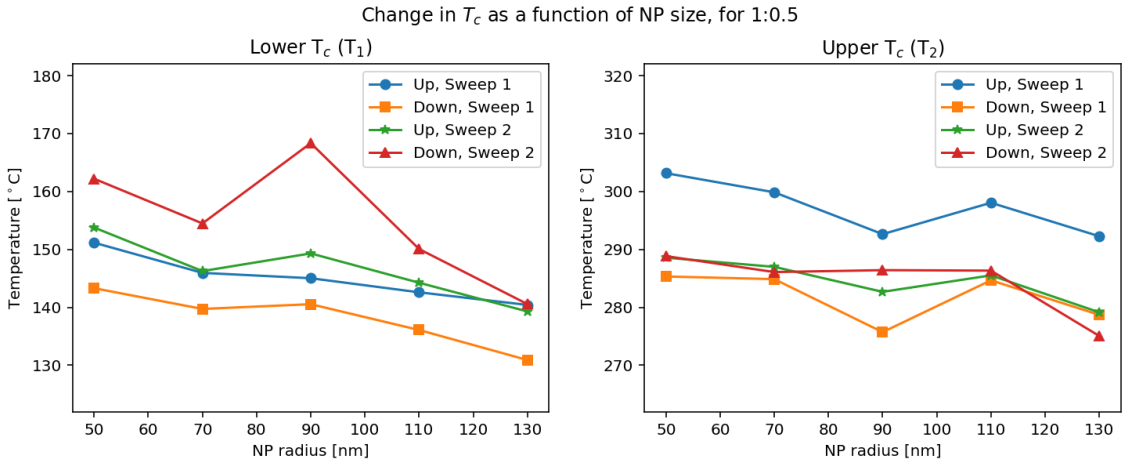

Figure 4.7: Showcases plots representing the evaluated critical temperature, T_c, as a function of the Pt nanoparticle size. The critical temperatures are taken from Table 4.1 and Table 4.2, with the left plot representing the lower T_c (or T_1 in the tables) and the right plot representing the upper T_c (or T_2 in the tables). Shown in these two plots are the T_c values evaluated for both the temperature-increasing and temperature-decreasing parts of both measurement sweep cycles.

Displayed in Figure 4.7, a linear trend between the evaluated critical temperatures and particle size can be observed, showcasing a potential dynamic relationship. With a decrease in particle size correlating with an increase in critical temperature. The linearity of this trend appears more distinctly for the lower critical temperatures than for the upper critical temperatures, with an outlier observed in both trends for nanoparticles with a radius of approximately 90 nm.

These observed trends could arise due to several factors and may either represent real physical dynamics or trends introduced by the experimental setup. If this is a measurement artifact, one possible explanation could be that a laminar flow developed inside the nanoreactor, resulting in insufficient mixing of the reactants, products, and Ar. Hence, as the gas flow progressed across the nanoparticle arrays, the reactants were linearly consumed, creating a reactant gradient along the nanoreactor. This could, in turn, give rise to the linear trend observed in Figure 4.7, with the largest nanoparticles being closest to the outlet of the nanoreactor and the smallest near the inlet. To rule out this possibility, new experiments with randomly ordered nanoparticle arrays should be considered, thus validating if these trends represent any real physical dynamics.

4.1.2 Single-particle analysis

Having established the general trends at the ensemble level in Section 4.1.1, this assessment is omitted for the single-particle analysis due to redundancy, with the focus instead being directly on analyzing reaction dynamics and characterizing potential phase transitions brought about by the presence of the reactants. Through this characterization, the aim of this section is to compare the results obtained from the single-particle analysis with those from the ensemble-level analysis.

As stated in the method, Section 3.1, the nanoparticles were arranged in 3×3 particle arrays within the nanoreactor for each particle size. Additionally, the experimental measurements used for the ensemble-level analysis were the same measurements used for the single-particle analysis, for each respective gas composition. The single-particle nanoplasmonic responses were obtained using a smaller region of interest around the individual particles, instead of around the whole ensemble array, and extracted employing the ImageJ tool "Z-axis Profile", as described in Section 3.3.1. Hence, the ensemble responses represents the superposition of single-particle responses. The following single-particle analysis mainly focuses on the 1:0.5 measurements, as it represents the most promising dataset in terms of detectability of kinetic phase transitions.

Figure 4.8 showcases the first nanoplasmonic measurement sweep, with the Ar background removed, for each nanoparticle with a radius of 130 nm at a 1:0.5 stoichiometric gas ratio within the 3×3 particle array. For corresponding figures representing the second sweep, as well as remaining particle sizes, see Appendix D.1.

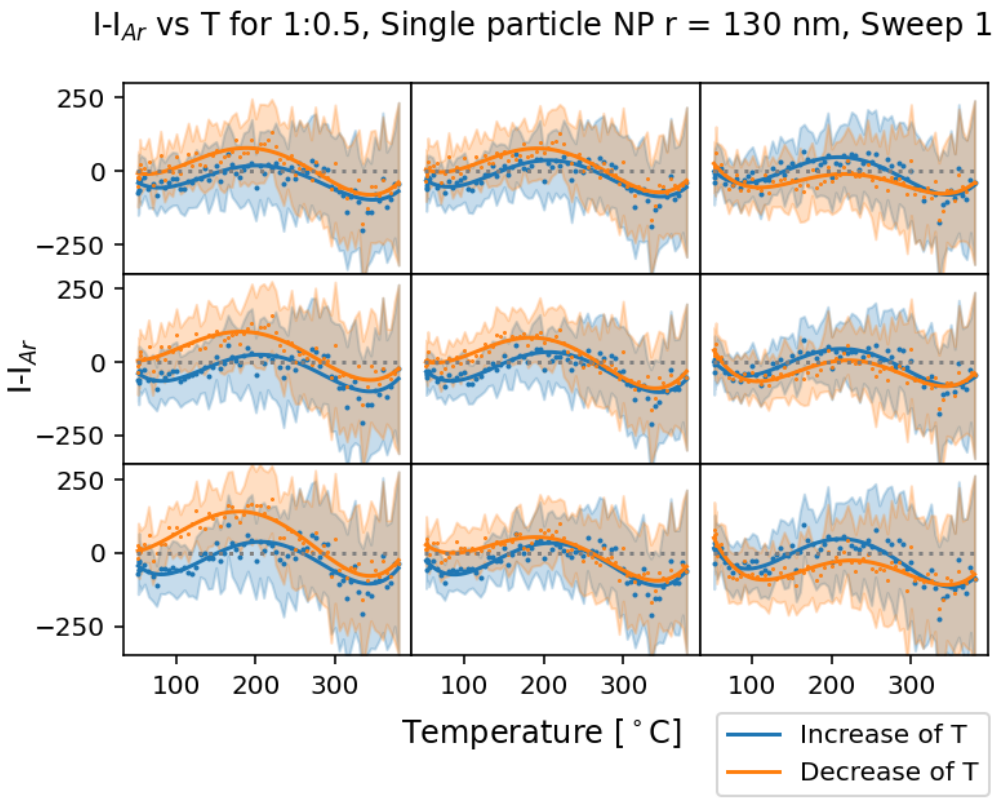

Figure 4.8: A figure showcasing fourth-degree polynomials fitted to the mean nanoplasmonic response data, after subtracting the Ar measurement response, for each nanoparticle within the 130 nm array as a function of temperature. Displayed in blue is the data recorded during the heating part of the sweep cycle, while orange represents the cooling part of the cycle. The shaded area showcases the calculated standard deviation of the calculated mean intensity. The data correspond to a gas composition of 1:0.5 ($CO:O_2$). Only the first sweep is displayed; the second sweep, as well as the data for the remaining particle sizes, can be found in Appendix D.1.

Comparing the ensemble data, found in Figure 4.8, with the data for each individual single-particle, found in Figure 4.2a, slight deviations can be observed between them. This was expected due to the previously mentioned superposition relation between the datasets, where, in an ideal case, adding up all single-particle measurements should result in the ensemble results.

Using the bootstrap approach to refit the 1:0.5 data, presented in Figure 4.8 and Appendix D.1, bootstrap-derived inflection points were extracted and plotted following the same procedure used to evaluate the measurements at the ensemble level in Section 4.1.1 under *Quantitative characterization*. Figure 4.9 presents the corresponding first sweep for the 1:0.5 measurements, while the second sweep is presented in Appendix D.2.

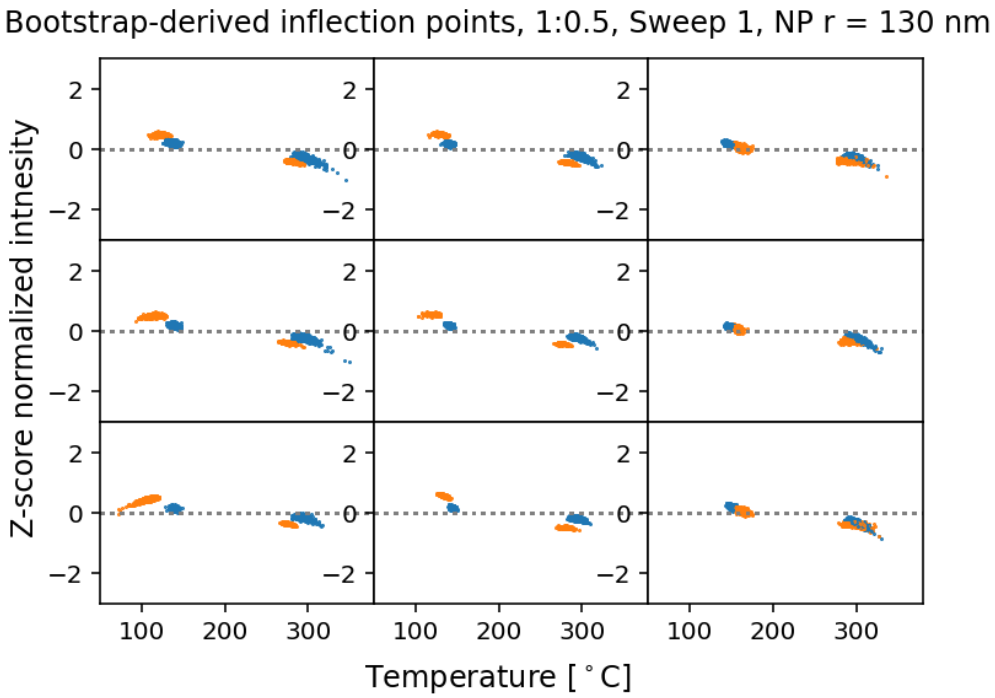

Figure 4.9: Plots showcasing the clustering of the evaluated inflection points of refitted fourth-degree polynomials from the bootstrap approach, for each nanoparticle in the 130 nm particle array at a gas composition of 1:0.5 ($CO:O_2$). These inflection points are derived from the nanoplasmonic sensing data presented in Figure 4.8 using the bootstrap approach. Only the first sweep is presented, with the second sweep found in Appendix D.2. Blue represents the inflection points from the temperature-increasing part of the sweep cycle, while orange represents the temperature-decreasing part of the cycle. The data have been z-score normalized along the y-axis, with the x-axis representing the temperature.

Consistent with the results from the ensemble analysis, both an upper and a lower inflection point are stable, for both the temperature-increasing and temperature-decreasing parts of the sweep cycle, as observed in Figure 4.9. This observation is consistent for both measurement sweeps and all particle sizes, as found in Appendix D.2. Treating these inflection points as critical temperatures, the mean critical temperatures and corresponding confidence intervals were calculated using these bootstrap-derived inflection points, as had also been done at the ensemble level of analysis in Section 4.1.1, under *Quantitative characterization*.

The mean critical temperatures and confidence intervals evaluated, for both the temperature-increase and temperature-decrease parts of each measurement sweep cycle, are presented as bar chart in Figure 4.10.

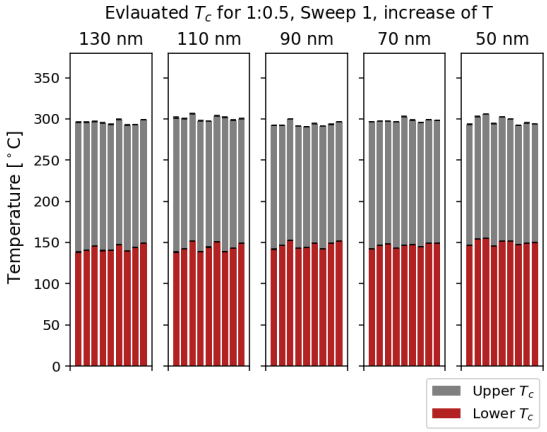

(a) Sweep 1, temperature-increasing.

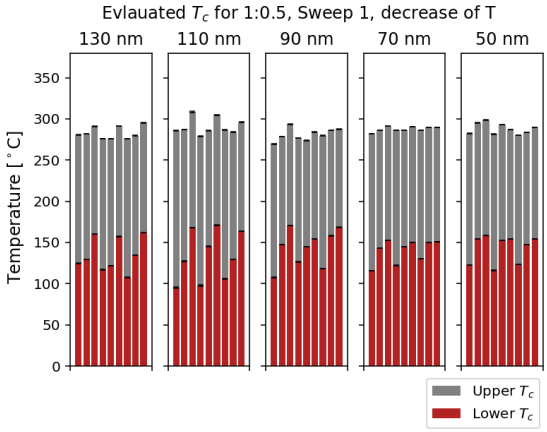

(b) Sweep 1, temperature-decreasing.

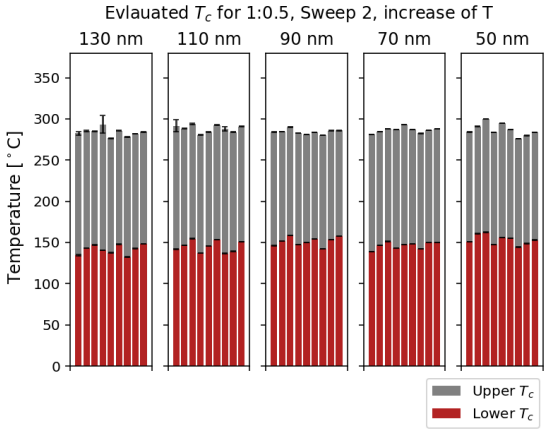

(c) Sweep 2, temperature-increasing.

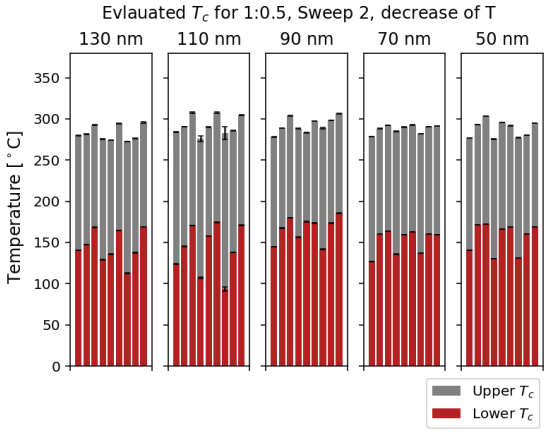

(d) Sweep 2, temperature-decreasing.

Figure 4.10: Bar charts of the evaluated critical temperatures for each nanoparticle, at a gas composition of 1:0.5, divided into their respective nanoparticle arrays. The lower critical temperature is presented in red, while the upper critical temperature is presented in gray. The evaluated confidence intervals are shown as black error bars. Charts **(a)** and **(b)** shows the temperature-increasing and temperature-decreasing part of the first sweep cycle, respectively, while charts **(c)** and **(d)** shows the temperature-increasing and temperature-decreasing part of the second sweep cycle.

Assessing Figure 4.10, it becomes clear that both the upper and lower critical temperatures behave similarly, especially during the temperature-decreasing part of the sweep cycles, for both the first and second sweeps. This could indicate that both critical temperatures are of a similar nature, thus strengthening the argument, as discussed in Section 4.1.1 under *Quantitative characterization*, that the lower critical temperature may represent a real physical phase transition. However, as also mentioned in the previous section, some observations point to the contrary, and the lack of evidence in the literature supporting such a phase transition means that further experimental studies are needed before any conclusive assessment can be made.

Additionally, when comparing Figure 4.10a and Figure 4.10c with Figure 4.10b

and Figure 4.10d, it can be observed that the critical temperatures evaluated for the temperature-decreasing parts of both sweep cycles are less uniform between particles of the same size than those for the temperature-increasing parts of both sweep cycles. Ascribing a physical phenomenon to this discrepancy between the temperature-increasing and temperature-decreasing parts of the sweep cycle is difficult. However, when comparing the critical temperatures during the temperature-decreasing parts of the first and second sweep cycles, shown in Figure 4.10b and Figure 4.10d, respectively, both between particle arrays and within each array, a pattern emerges in which particles occupying the same positions across arrays behave similarly compared to the other particles within each array. For example, the third particle in each size array in Figure 4.10d appears as a similar outlier in each array from 130 nm to 50 nm, when compared to the other nanoparticles within each array. This strongly indicates that the non-uniform responses in the temperature-decreasing part of the sweep cycle are related to the particle placement and surroundings within each differently sized array.

This observation of positional symmetry across serval arrays could possibly be related to an idea presented in Section 4.1.1 under *Quantitative characterization*, when assessing Figure 4.7, that poor mixing of reactants along the reactor may create streams of unbalanced reactant mixtures along the gas flow. Returning to Figure 4.10b and Figure 4.10d, outliers can be observed in each array, matching each other for every third particle, which aligns with particles arranged after each other in the array having similar responses. This behavior is also observable in Figure 4.9, where the clusters next to each other in the array appear similar when aligned in the direction of the gas flow. With this behavior being observed across arrays, it gives more validity to this explanation.

On a general note, throughout the experimental procedure, clear differences in the behavior of the plasmonic response of the nanoparticles are observed when comparing the first and second sweeps. This can be explained by the fact that the particles in the first sweep start out in pristine CO-reduced states, whereas the particles in the second sweep have already been exposed to O_2. This difference is most noticeable in the single-particle results presented in Figure 4.10, but is also evident in the ensemble analysis, see Figure 4.2 and Figure 4.3. This discrepancy between the first and second sweeps makes it difficult to draw conclusions regarding the dynamics of the phase transitions. To better emulate *operando* conditions, future temperature-dependent nanoplasmonic sensing measurements aimed at characterizing phase-transition dynamics should investigate whether the response stabilizes after the second sweep. If so, measurements could be performed on nanoparticles that have been pre-exposed to both reactants to more accurately emulate the working conditions of a real catalyst, which may go through many reaction cycles.

Continuing with the single-particle analysis, a particle was picked in each array, at the same relative position, to assess the relationship between the evaluated critical values and particle size, just as was done at the ensemble level in Figure 4.7. Presented in Figure 4.11 is the whole nanoreactor with each array of differently sized nanoparticles. Marked in red are the selected particles to be assessed in the analysis.

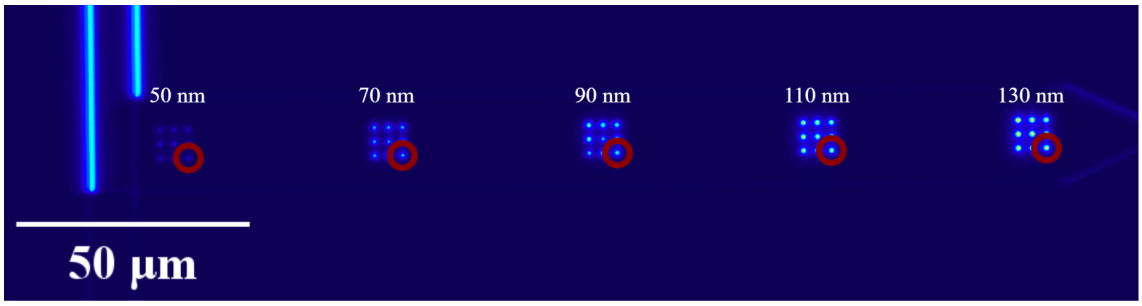

Figure 4.11: Showcases the five nanoparticle arrays within the nanoreactor and the radius of the nanoparticles within each respective array. Marked in red is a randomly selected nanoparticle, consistent across all arrays, chosen for further single-particle analysis.

Evaluated mean critical temperatures and corresponding confidence intervals of the marked nanoparticles in Figure 4.11 were extracted from Figure 4.10, for both sweeps and for both the temperature-increasing and temperature-decreasing parts of the sweep cycles. Thus, resulted in Table 4.3 and Table 4.4.

	Sweep 1							
	Up T_1		Down T_1		Up T_2		Down T_2	
NP [nm]	T_c	C.I.	T_c	C.I.	T_c	C.I.	T_c	C.I.
130	145.46	±0.14	160.36	±0.23	296.90	±0.37	291.22	±6.86
110	151.54	±0.16	167.83	±0.26	306.40	±0.52	308.45	±12.1
90	152.54	±0.12	170.38	±0.23	299.81	±0.32	293.67	±6.14
70	148.44	±0.04	152.31	±0.05	297.37	±0.11	291.18	±1.78
50	154.92	±0.06	158.84	±0.09	305.75	±0.18	298.44	±3.34

Table 4.3: Table of acquired critical temperatures and receptive confident interval of the from Figure 4.10a and Figure 4.10b, representing the first sweep.

	Sweep 2							
	Up T_1		Down T_1		Up T_2		Down T_2	
NP [nm]	T_c	C.I.	T_c	C.I.	T_c	C.I.	T_c	C.I.
130	147.17	±0.23	168.22	±0.23	285.13	±0.48	292.58	±6.59
110	154.54	±0.23	170.51	±0.22	294.03	±0.57	307.56	±9.23
90	158.62	±0.21	179.86	±0.23	289.72	±0.43	303.37	±7.40
70	151.20	±0.07	163.92	±0.06	287.86	±0.14	292.04	±1.87
50	162.32	±0.12	172.39	±0.11	299.95	±0.29	303.27	±3.83

Table 4.4: Table of acquired critical temperatures and receptive confident interval of the from Figure 4.10c and Figure 4.10d, representing the second sweep.

By plotting the corresponding critical temperatures reported in Table 4.3 and Table 4.4 as a function of particle size, the plots shown in Figure 4.12, were acquired. For comparison between the single-particle and ensemble analyses, the results from the ensemble analysis, reported in Figure 4.7, were desaturated and overlaid onto the single-particle results in Figure 4.12.

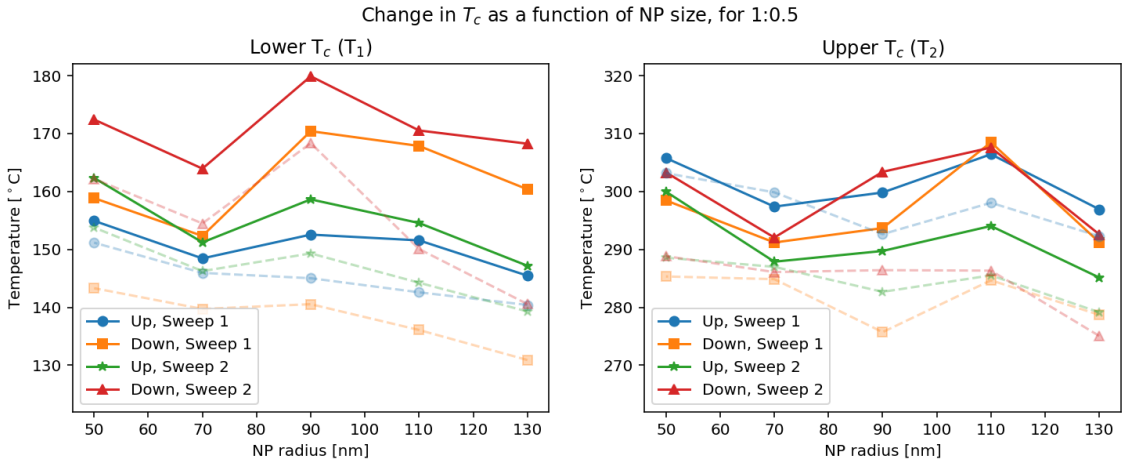

Figure 4.12: Figure showcasing plots representing the evaluated critical temperature, T_c, as a function of the Pt nanoparticle size taken from Table 4.3 and Table 4.4. The left plot representing the lower T_c (or T_1 in the tables) and the right plot representing the upper T_c (or T_2 in the tables). Shown in these two plots are the T_c values evaluated for both measurement sweeps and both temperature-increasing and temperature-decreasing parts of each respective sweep. Overlaid and represented by the desaturated dashed lines are the corresponding results from the ensemble level analysis, presented in Figure 4.7, for ease of comparison.

Comparing the single-particle data, presented in Figure 4.12, with the ensemble results, a clear distinction between the size-dependent relationships can be seen. What was described as a potential linear relationship when assessing Figure 4.7 can instead be observed, for both the upper and lower critical temperatures, to behave in accordance with a third-degree polynomial. This could invalidate the interpretation previously discussed regarding how a linear decrease in critical temperature as a function of size could imply that the reactants are consumed as a function of position along the nanoreactor.

This discrepancy between single-particle and ensemble analysis highlights the necessity of single-particle analysis to investigate phenomena and characteristics hidden by ensemble averaging.

4.2 Structural analysis

Following the motivation given in Section 4.1.1, a structural analysis was conducted in accordance with the method presented in Section 3.2.2 to evaluate any potential morphological changes in the nanoparticles. This analysis was performed using hyperspectral imaging to probe changes in the plasmonic scattering wavelength and was complemented by SEM imaging to visualize any potential topological changes.

4.2.1 Hyperspectral imaging

Hyperspectral imaging was performed at the ensemble level, as described in Section 3.2.2, *Hyperspectral imaging*, at wavelengths between 470 and 700 nm. For the analysis of the results, presented in Figure 4.13, it is essential to consider the tem-

perature and gas composition history to which the nanoparticles had been exposed prior to imaging. Before each hyperspectral imaging session, the nanoparticles had been exposed to a full measurement cycle with gas flows corresponding to a 1:0.5 measurement, but with only CO, only O_2, and then only CO, respectively, see Figure 3.5. Additionally, to compare the response between particle sizes, the plots were min-max normalized.

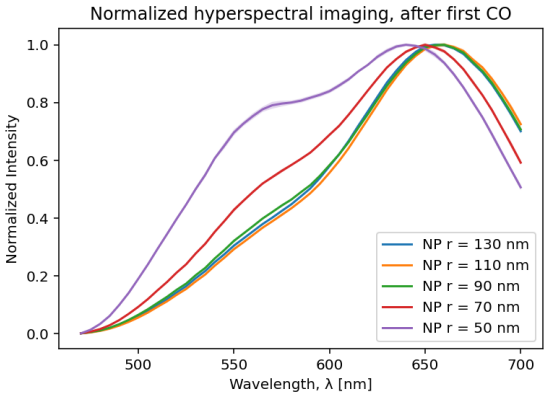

(a) Normalized hyper spectral imaging, after first CO

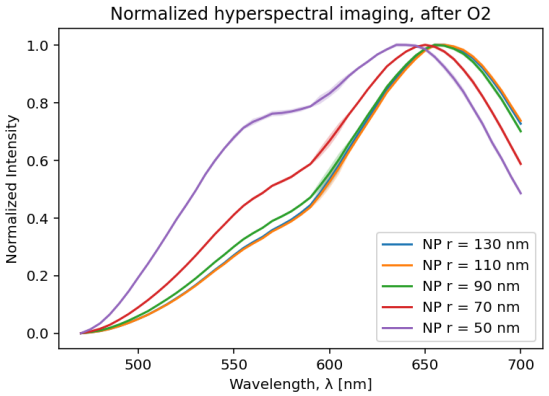

(b) Normalized hyper spectral imaging, after O2

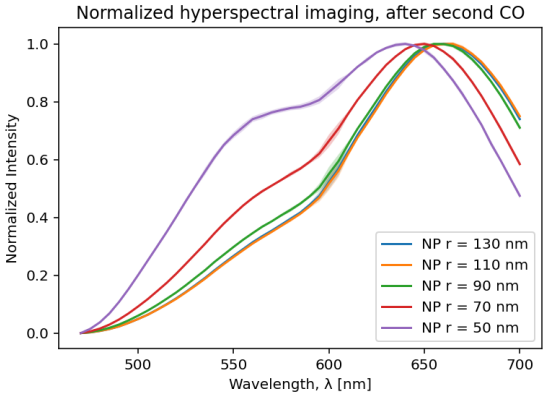

(c) Normalized hyper spectral imaging, after second CO

Figure 4.13: Three hyperspectral imaging plots, containing the min-max normalization mean spectral response for each of the five nanoparticle sizes, are displayed in this figure. Each plot represents the response after the nanoparticles had been exposed to a gas composition containing either only Ar-diluted CO or only Ar-diluted O_2, following the procedure described in Section 4.2.1 with reference to Figure 3.5. Contained within **(a)** is the spectral response after only CO exposure, **(b)** shows the spectral response after only O_2 exposure, and finally **(c)** shows the spectral response after only CO exposure again. The shaded area, for each particle size, represents the standard deviation of the mean spectral response.

The spectral responses in Figure 4.13 are all affected by a systematic error due to an interfering spectrum from the light source within the spectral range used for acquisition. In addition to the broadening of the plasmonic scattering peaks of particles at these sizes [48], the resulting hyperspectral responses appear to possess more than one plasmonic peak. However, since all spectra are affected by the same systematic error, comparative analyses with respect to particle size are still possible.

For ease of comparing the three measurements presented in Figure 4.13, particles of sizes 130 and 110 nm were selected and compared to each-other, resulting in Figure 4.14.

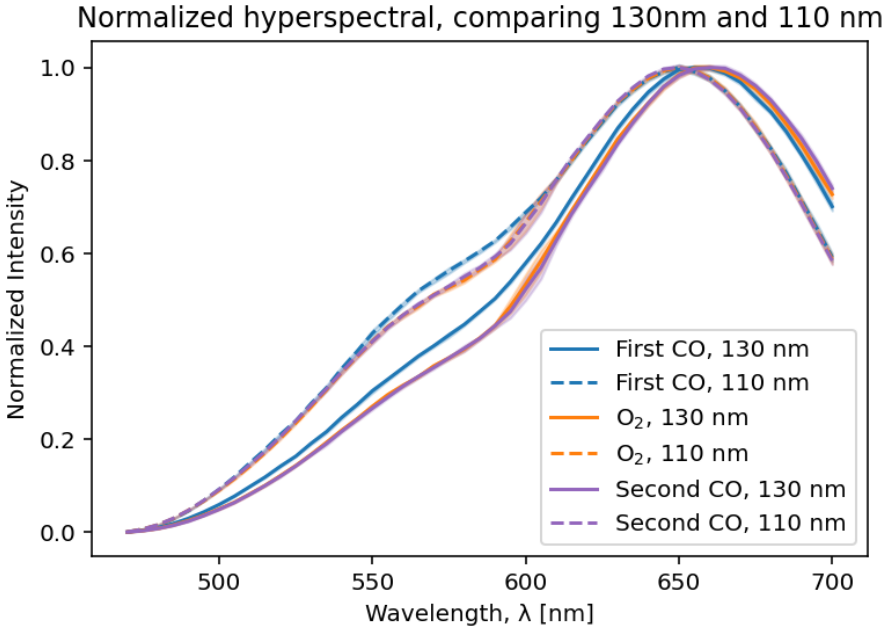

Figure 4.14: Represents the mean max-min normalized hyperspectral imaging responses for selected nanoparticles of radius 130 nm (the solid lines) and 110 nm (the dashed lines) for each of the three plots presented in Figure 4.13. Presented in blue is the response from Figure 4.13a, representing the spectral response after the first round of exposure to only CO, barely viable, but presented in orange is the spectral response from Figure 4.13b, showing the response after only O_2 exposure, and finally, overlayed on the orange graph, is the purple graph, representing the spectral response after the second round of only CO exposure. The shades area represent the standard deviation of the mean spectral response for each measurement.

The only CO measurements in Figure 4.14 overlap perfectly with the only O_2 measurements, but not the first CO measurements, although the variation is small. This is true for both particle sizes. This indicates not only that the full experimental cycle, together with the addition of O_2, seems to alter the plasmonic response wavelengths and thus, by extension, most likely changes the nanoparticle structure. Additionally, this process seems to be irreversible, as if it were a reversible process, then the first and second only CO measurements would overlap with each other. It

is previously known that the addition of O_2 to Pt nanoparticles at high temperature can edit the surface morphology of the nanoparticles, but it was not expected to have such a drastic effect after just one experimental cycle and at these concentrations.

To complement these findings and see if any visible changes can be observed in the nanoparticles as they are exposed to a given gas environment, SEM images were taken.

4.2.2 SEM imaging

As stated in Section 3.2.2, SEM imaging could not be performed on the main chip due to the glass lid enclosing the nanoreactor, which blocked the SEM electron beam. Instead, a control replica of the main chip, but without the glass lid, was fabricated. In order to investigate the impact that the gas and temperature exposure had on the main chip, the exposure history was to be repeated on the post-annealed reference sample. However, due to time constraints and the long measurement times to which the main chip was exposed, only an extremely limited replication of the exposure history was possible.

Showcased in Figure 4.15 and Figure 4.16 are the acquired SEM images post-annealing, as well as after around 40 h of Ar exposure under conditions resembling a 1:0.5 gas composition between 30 and 380 °C, followed by an additional 72 h of CO and O_2 exposure at a 1:0.5 gas ratio and a temperature of 350 °C, for particles with radii of 130 and 50 nm, respectively. For ease of visualization, the contrast was increased in the following images to reveal potential structural changes, such as sintering.

It is important to note that these measurements were performed over a limited exposure time, with technical issues present, and were not conducted on the same nanoparticles used for the nanoplasmonic sensing measurements and hyperspectral imaging. The results presented here are complementary and not sufficiently extensive to draw any conclusive conclusions.

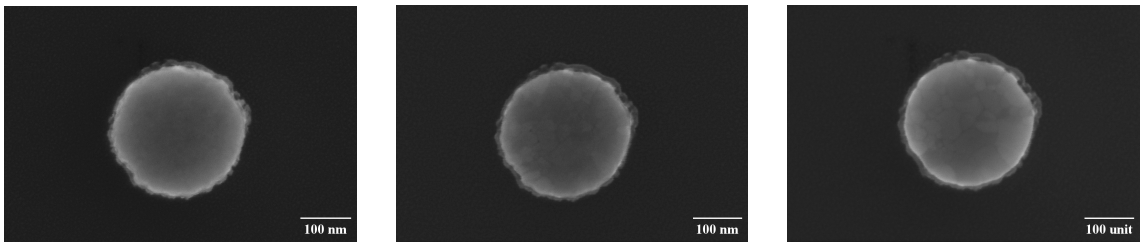

(a) SEM, post-annealing. **(b)** SEM, after 40 h. **(c)** SEM, after 112 h.

Figure 4.15: SEM images of the same nanoparticle with radii 130 nm after different exposer history. **(a)** showcase how to particle looks post-annealing. **(b)** is the particle after around 40 h of Ar exposure and two full measurement temperature cycles. **(c)** showcase the particle after extensive CO and O_2 exposer for around and additional 72 h, for a total of 112 h.

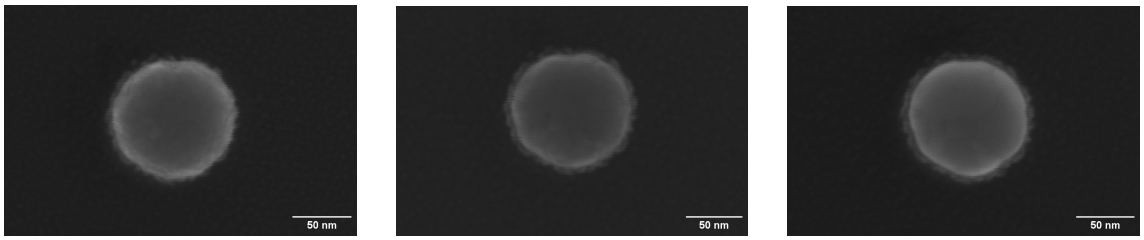

(a) SEM, post-annealing. **(b)** SEM, after 40 h. **(c)** SEM, after 112 h.

Figure 4.16: SEM images of the same nanoparticle with radii 50 nm after different exposer history. **(a)** showcase how to particle looks post-annealing. **(b)** is the particle after around 40 h of Ar exposure and two full measurement temperature cycles. **(c)** showcase the particle after extensive CO and O_2 exposer for around and additional 72 h, or a total of 112 h.

From the images presented in Figure 4.15 it is possible to discern structural changes in the morphology of the nanoparticle, as larger grain like structures form. In the post-annealing image, Figure 4.15a, the particle can be observed looking uniform and milky, with no distinct grain boundaries. This is attributed to the particle consisting of a large amount of small grains instead of a uniform crystal. As the particle is exposed to the reactants and temperature cycles, larger grain structures seems to form, growing larger in relationship with exposure time. With grain size increasing and more distinct between Figure 4.15b and Figure 4.15c. This could indicated that the particles becomes more uniformly crystalline thought the measurement process.

The observed structural changes and aging-like process of the nanoparticles, as shown in Figure 4.15, could potentially explain several of the previously observed results. Those being; the irreversible structural changes observed in the hyperspectral imaging results, Figure 4.14, as well as the intensity drift between the heating and cooling part of each measurement sweep, as observed in Section 4.1.1. Regarding the drift process, as described in the aforementioned section, the absolute intensity of the plasmonic response is higher at 50° C, that is, after a measurement sweep, when compared to before the sweep. If it is so that the nanoparticle becomes more uniformly crystalline as a as a result of aging throughout the measurement process, this drift could be explained by the formation of larger crystalline grains, resulting in higher electron mobility. Additionally, a increase in electron mobility results, would yield a stronger plasmonic response as a result of the electrons more easily travel across the nanoparticel and oscillate with the incident light.

Furthermore, in Section 4.1.1, a general trend was observed in which smaller nanoparticles yield a proportionally smaller standard deviation in the nanoplasmonic response. As mentioned, as the nanoparticles age throughout the measurement cycles, grains and regions of different crystallinity seem to grow. As seen in Figure 4.16, for smaller nanoparticles, these grains are proportionally larger when compared to the larger nanoparticles in Figure 4.15. Hence, smaller nanoparticles may exhibit a more uniform plasmonic response, resulting in a smaller standard deviation.

To conclude the structural analysis, the observed aging-like irreversible process, as reported throughout this thesis and in the hyperspectral imaging, most likely indicates insufficient annealing. Annealing is done in an effort to prevent these types of structural changes, however, as seen in Figure 4.15 and Figure 4.16, crystalline grains continue to grow throughout the exposure process, even post-annealing. This could indicate that the annealing process, as reported in Section 3.1.1, may be insufficient.

Chapter 5

Conclusion

Catalysis, and the research surrounding it, are essential for the proliferation of several different industries. In this thesis, nanoplasmonic sensing has been assessed as a technique for studying catalytic Pt nanoparticles during CO-oxidation, a catalytic reaction that is essential to understand for the development of next-generation catalytic converters and other pollution-removing devices needed for a cleaner environment. Specifically, the aim of this thesis has been to study the CO-oxidation reaction over Pt nanoparticles using a temperature-programmed nanoplasmonic sensing setup to perform both ensemble and single-particle analyses of the temperature-dependent reaction dynamics under *operando* conditions. The continued development of nanoplasmonic sensing and other single-particle *operando* measurement techniques is key to facilitating the development of new catalytic materials.

Investigated in this project was how the plasmonic response from the nanoplasmonic sensing measurements varied as a function of temperature, within the range of 30 to 380 °C, depending on the particle size and the $CO{:}O_2$ reactant ratio. The measurements were performed on a nanoreactor chip installed in a dark-field microscopy setup, with an attached QMS to monitor the gas composition exiting the nanoreactor. The nanoreactor was etched into a SiO_2 substrate and was composed of five Pt nanoparticle arrays enclosed by a glass lid. Each array consisted of a 3×3 arrangement of equally sized nanoparticles with radii of 130, 110, 90, 70, or 50 nm, respectively. To complement the findings from the nanoplasmonic sensing measurements, a structural analysis was conducted, consisting of hyperspectral imaging and SEM imaging on a replica chip, which was fabricated and exposed to a measurement history similar to that of the main chip in order to replicate any potential morphological changes that such exposure may have caused.

The following conclusions were derived from the findings reported in Chapter 4, *Results and Analysis*. These conclusions are divided into three parts to accommodate the abundance of results. First, nanoplasmonic sensing is assessed as a single-particle *operando* technique for studying temperature-dependent reaction dynamics. This is

followed by an evaluation of the methodology and potential improvements thereof, and finally by a summary of the observed temperature-dependent reaction dynamics specific to CO-oxidation when facilitated by Pt nanoparticles.

Starting with the assessment of nanoplasmonic sensing as a technique for studying temperature-dependent reaction dynamics at the single-particle level under *operando* conditions. Demonstrated in this thesis was that nanoplasmonic sensing, when applied to a nanoreactor system with QMS monitoring, is capable of observing temperature-dependent reaction dynamics in the CO-oxidation reaction catalyzed by Pt nanoparticles, owing to the implementation of the autofocusing scrip. This is mainly supported by the observation of a kinetic phase transition in Pt nanoparticles during CO-oxidation around the expected temperature, as well as by the characterization of the dynamics of this phase transition at both an ensemble and single-particle level of analysis. Additionally, as shown in Figure 4.12, when assessing the relationship between particle size and kinetic phase transitions at the single-particle level, differences in dynamics were reviled when compared to the ensemble analysis, thus demonstrating the necessity for single-particle analysis to counteract ensemble averaging effects.

However, as reported in Section 4.1.1 under *Quantitative characterization*, the appearance of two transitions, both exhibiting similar behavior, was unexpected and requires further analysis. It was suggested that if the anomalous of these transitions, specifically the lower-temperature transition, proves not to represent a real phenomenon after further analysis, then it may be a measurement/data-treatment artifact, potentially caused by inadequate calibration of the temperature control unit, as mentioned in Section 4.1.1 under *Qualitative characterization*. Yet, if no measurement/data-treatment artifact is found, this could indicate that this nanoplasmonic sensing setup may not be suited for lower-temperature measurements.

Overall, the methodology used in this thesis proved sufficient, and the addition of the bootstrap method to evaluate potential phase transitions using a given model showcased its potential as a useful approach for future investigations of temperature-dependent phase transitions. However, several potential improvements were identified. Two of these, as previously mentioned, were the investigation of new data-treatment methods should the lower-temperature phase transition prove not to represent a real phenomenon, as well as acquitted calibration of the temperature control unit in future experiments using this experimental setup. In addition to these, three additional potential improvements were identified.

The first and most important improvement would be the development of a method to counteract the drift in plasmonic response when comparing the plasmonic intensity before and after the measurement sweep cycle. In the structural analysis, Section 4.2, this drift is attributed to irreversible structural changes as observed in the hyperspectral imaging, shown in Figure 4.14. This makes it critical to solve, as this aging-like effect makes it difficult to compare results between measurements. The hyperspectral imaging findings were complemented by the SEM imaging in Section 4.2.2, where it was observed that the nanoparticles were polycrystalline after the

annealing process and subsequently transitioned into single-crystalline grains as they were exposed to the nanoplasmonic sensing measurement process. This indicates that the annealing process, as described in Section 3.1.1, may be insufficient for the nanoparticles and experimental setup used in this project. Further investigations into increasing the annealing temperature and duration, or modifying the annealing environment, should be considered.

The second improvement would be the modification of the stabilization script. This script was used to counteract the spatial drift of the chip that occurs during image acquisition and to align the images so that the intensities could be extracted across all acquisitions using the ImageJ "Z-axis Profile" tool. However, as this script was not designed to treat multiple arrays at the same time, mismatches between images could occur, leading to outliers in the data. Hence, editing of the script to accommodate future measurements of multiple nanoparticle arrays should be considered.

Third, clear differences in the plasmonic responses were observed when comparing the first and second measurement sweeps, which was observed at both the ensemble and single-particle levels. This can be explained by the first sweep starting in an already CO-reduced state, whereas during the second sweep the nanoparticles have already been exposed to O_2, which may cause residual effects. However, real catalysts may experience several temperature sweeps in their working environment. Hence, in an effort to close the material gap, future experiments could pre-expose the nanoparticles to the gas mixture at high temperature or investigate the effect that multiple sweep cycles have on the plasmonic response.

The following conclusions concern the characterization of the temperature-dependent reaction dynamics of the CO-oxidation reaction catalyzed by Pt nanoparticles, as observed using nanoplasmonic sensing, with particular regard to the identification of phase transitions and the characterization of their dynamics.

As mentioned when assessing nanoplasmonic sensing as a measurement technique to study temperature-dependent reaction dynamics, two potential phase transitions were unexpectedly observed. These transitions persisted for both ensemble and single-particle levels of analysis and expressed themselves most definitively at a gas composition of 1:0.5, once the Ar background had been removed. The higher-temperature transition aligns with an expected phase transition between approximately 200 and 460 °C for nanoparticles of these sizes supported on a SiO_2 substrate, and would then correspond to the kinetic phase transition of the nanoparticles from their CO-poisoned state to the active state. This observation, together with the absence of a clear higher-temperature transition in the measurements containing only CO, indicates that the higher-temperature transition is a real kinetic phase transition. In contrast, the lower-temperature transition was previously unaccounted for at these particle sizes in the literature and is also present in the measurements containing only CO. This indicates that, even though both changes in the plasmonic response are stable across particle sizes and behave similarly, only the higher-temperature transition seems to represent a real kinetic phase transition. As suggested in Section 4.1.1, further studies of the lower-temperature transition,

using other single-particle *operando* techniques such as ETEM, are required for any conclusive assessment and characterization of this transition. Hence, the following conclusion regarding the temperature-dependent reaction dynamics will focus on the higher-temperature transition.

Regarding the effect of gas composition, starting with the ensemble observations, gas compositions of 1:0.25 are shown to lack any stable inflection points and exhibit similar dynamics to the only CO measurements. These observations are complemented by the single-particle analysis. Thus, it can be concluded that a gas composition of 1:0.25 likely does not provide sufficient oxygen to facilitate the CO-oxidation reaction. It was suggested that, for a more conclusive assessment of the effect O_2 concentration has on the temperature-dependent dynamics, more intermediary concentrations between 1:0.5 and 1:0.25 could be introduced in future experiments. As for the only O_2 measurements, unstable clustering of bootstrap-derived inflection points suggests the presence of a phase transition. However, this transition was expected to diminish if more sweep cycles were performed, as the adsorbed CO on the catalytic surface is consumed.

As for the size-dependent effects, two primary observations were made. First, the evaluated critical temperatures of the phase transitions were plotted as a function of particle size, at both the ensemble and single-particle levels of analysis, in order to identify any potential relationship between them. At the ensemble level was a linear decrease with increasing particle size was observed. This linearity could represent a real relationship between particle size and critical temperature. However, an alternative possibility was proposed; that a reactant gradient may develop along the length of the reactor as the reactants are consumed, and that this could influence the critical temperatures of the phase transitions. Further assessment of this relationship would require a secondary experiment with particle arrays not ordered according to particle size along the length of the reactor. However, the single-particle analysis revealed a new, nonlinear relationship between particle size and critical temperature. This observation showcases how the addition of single-particle analysis helps highlight effects that are averaged out when analyzing data at an ensemble level. Conversely, a possible spatial-dependent relationship was still observed in the single-particle analysis. When comparing particles aligned along the gas flow direction and located within the same array, similar responses were observed, which could indicate that a longitudinal gradient may still be present. A potential way to study the presence of this gradient would be to randomly distribute the particles within each array, instead of placing them in a grid pattern. This setup may also better emulate the more random distribution of nanoparticles within real catalytic systems.

The secondary size-dependent observation was that smaller nanoparticles exhibited more stable plasmonic responses, as well as a decrease in standard deviation with decreasing particle size. This observation was unexpected and may be an effect of insufficient annealing of the nanoparticles. Observed in the SEM analysis is that, for smaller nanoparticles, the single-crystalline grains cover a proportionally larger area of the nanoparticles compared to the larger particles, which in turn may result

in a more uniform plasmonic response.

As a closing statement, the study of single-particle *operando* techniques, such as nanoplasmonic sensing, is not only important for the investigation of the CO-oxidation reaction but also for the development of new techniques to enable future analysis of temperature-dependent reaction dynamics. With the prevalence of catalysts in society, this thesis has aimed at bringing insights that facilitate the development and design of novel and more effective catalysts, in order to promoting a cleaner environment.

Bibliography

[1] L. Cademartiri and G. A. Ozin, *Concepts of Nanochemistry*. Weinheim, Germany: Wiley-VCH, 2009, ISBN: 978-3-527-32597-9.

[2] S. Bayda, M. Adeel, T. Tuccinardi, M. Cordani, and F. Rizzolio, "The history of nanoscience and nanotechnology: From chemical-physical applications to nanomedicine," *Molecules*, vol. 25, no. 1, p. 112, 2019. DOI: 10.3390/molecules25010112.

[3] D. Albinsson, "Operando single particle catalysis: Combining a nanoreactor and plasmonic nanospectroscopy," Doctoral Thesis, Chalmers University of Technology, Gothenburg, Sweden, 2020, ISBN: 978-91-7905-380-2.

[4] V. E. Babicheva, Y.-J. Lu, A. Shalin, and D. Late, "Introduction to advances in nanophotonics, plasmonics, and nano-optics," *Nanoscale Advances*, vol. 7, no. 21, pp. 6674–6676, Nov. 2025, ISSN: 2516-0230. DOI: 10.1039/d5na90067k.

[5] M. Di, "Co oxidation over oxide supported platinum catalysts," Doctoral Thesis, Chalmers University of Technology, Gothenburg, Sweden, 2023, ISBN: 978-91-7905-804-3.

[6] M. A. Abah et al., "Sustainable catalysis: A review of green catalysts and their applications," *Journal of e-Science Letters*, vol. 6, no. 4, pp. 37–44, 2025, ISSN: 3041-5454. DOI: 10.51470/eSL.2025.6.4.37.

[7] I. Chorkendorff and J. W. Niemantsverdriet, *Concepts of Modern Catalysis and Kinetics*, 2nd ed. Weinheim, Germany: Wiley-VCH Verlag GmbH & Co. KGaA, 2007, ISBN: 978-3-527-31672-4. DOI: 10.1002/9783527610044.

[8] J. K. Nørskov, F. Studt, F. Abild-Pedersen, and T. Bligaard, "Catalyst structure," in *Fundamental Concepts in Heterogeneous Catalysis*. John Wiley Sons, Ltd, 2014, ch. 9, pp. 138–149, ISBN: 9781118892114. DOI: https://doi.org/10.1002/9781118892114.ch9.

[9] Z. Ma and F. Zaera, "Characterization of heterogeneous catalysts," in *Surface and Nanomolecular Catalysis*, R. M. Richards, Ed., CRC Press, 2006, ch. 1, pp. 1–37, ISBN: 9781574444810. DOI: 10.1201/9781420015751.ch1.

[10] H.-J. Freund, H. Kuhlenbeck, J. Libuda, G. Rupprechter, M. Bäumer, and H. Hamann, "Bridging the pressure and materials gaps between catalysis and surface science: Clean and modified oxide surfaces," *Topics in Catalysis*, vol. 15, pp. 201–209, 2001, ISSN: 1022-5528. DOI: 10.1023/A:1016686322301.

[11] C. Langhammer, Z. Yuan, I. Zorić, and B. Kasemo, "Plasmonic properties of supported pt and pd nanostructures," *Nano Letters*, vol. 6, no. 4, pp. 833–838, 2006. DOI: 10.1021/nl060219x.

[12] D. Albinsson, S. Bartling, S. Nilsson, H. Ström, J. Fritzsche, and C. Langhammer, "Shedding light on CO oxidation surface chemistry on single Pt catalyst nanoparticles inside a nanofluidic model pore," *ACS Catalysis*, vol. 11, no. 4, pp. 2021–2033, 2021, ISSN: 2155-5435. DOI: 10.1021/acscatal.0c04955.

[13] C. Jarvis, "Elizabeth fulhame, a forgotten chemistry pioneer," *Physics Today*, Jun. 2020. DOI: 10.1063/PT.6.4.20200617a. [Online]. Available: https://physicstoday.aip.org/news/elizabeth-fulhame-a-forgotten-chemistry-pioneer.

[14] P. Atkins, L. Jones, and L. Laverman, *Chemical Principles: The Quest for Insight*, 7th ed. W. H. Freeman and Company, 2016, ISBN: 9781319154196.

[15] J. K. Nørskov, F. Studt, F. Abild-Pedersen, and T. Bligaard, "The potential energy diagram," in *Fundamental Concepts in Heterogeneous Catalysis*. John Wiley Sons, Ltd, 2014, ch. 2, pp. 6–25, ISBN: 9781118892114. DOI: 10.1002/9781118892114.ch2.

[16] D. Kiani and I. E. Wachs, "Practical considerations for understanding surface reaction mechanisms involved in heterogeneous catalysis," *ACS Catalysis*, vol. 14, no. 22, pp. 16 770–16 784, Oct. 2024, ISSN: 2155-5435. DOI: 10.1021/acscatal.4c05188.

[17] C. H. Bartholomew, "Mechanisms of catalyst deactivation," *Applied Catalysis A: General*, vol. 212, no. 1, pp. 17–60, 2001, Catalyst Deactivation, ISSN: 0926-860X. DOI: 10.1016/S0926-860X(00)00843-7.

[18] M. Omrani, M. Goriaux, Y. Liu, S. Martinet, L. Jean-Soro, and V. Ruban, "Platinum group elements study in automobile catalysts and exhaust gas samples," *Environmental Pollution*, vol. 257, p. 113 477, 2020, ISSN: 0269-7491. DOI: https://doi.org/10.1016/j.envpol.2019.113477.

[19] V. Zhdanov and B. Kasemo, "Kinetic phase transitions in simple reactions on solid surfaces," *Surface Science Reports*, vol. 20, no. 3, pp. 113–189, 1994, ISSN: 0167-5729. DOI: 10.1016/0167-5729(94)90009-4.

[20] P.-A. Carlsson and M. Skoglundh, "Low-temperature oxidation of carbon monoxide and methane over alumina and ceria supported platinum catalysts," *Applied Catalysis B: Environmental*, vol. 101, no. 3, pp. 669–675, 2011, ISSN: 0926-3373. DOI: 10.1016/j.apcatb.2010.11.008.

[21] G. Lin, G. Chen, and J. Lu, "In-situ characterization techniques for investigations of heterogeneous catalysis," *Journal of Alloys and Compounds*, vol. 1010, p. 177 552, 2025, ISSN: 0925-8388. DOI: 10.1016/j.jallcom.2024.177552.

[22] N. Zhao, F. Dong, Y. Kang, L. Wu, and Z. Tang, "Research progress and future challenges of co oxidation catalysts: Preparation, catalytic performance, reaction mechanism and anti-poisoning strategies," *Journal of Materials Chemistry A*, vol. 14, no. 19, pp. 11 083–11 117, Mar. 2026, ISSN: 2050-7488. DOI: 10.1039/d5ta09749e.

[23] S. Zhang, L. Nguyen, Y. Zhu, S. Zhan, C.-K. (Tsung, and F. (Tao, "In-situ studies of nanocatalysis," *Accounts of Chemical Research*, vol. 46, no. 8, pp. 1731–1739, Apr. 2013, ISSN: 0001-4842. DOI: 10.1021/ar300245g.

[24] R. T. Vang, E. Lægsgaard, and F. Besenbacher, "Bridging the pressure gap in model systems for heterogeneous catalysis with high-pressure scanning tunnel-

ing microscopy," *Physical Chemistry Chemical Physics*, vol. 9, no. 27, pp. 3460–3469, Jan. 2007, ISSN: 1463-9076. DOI: 10.1039/b703328c.

[25] E. D. Boyes, A. P. LaGrow, M. R. Ward, T. E. Martin, and P. L. Gai, "Visualizing single atom dynamics in heterogeneous catalysis using analytical in situ environmental scanning transmission electron microscopy," *Philosophical Transactions of the Royal Society A: Mathematical, Physical and Engineering Sciences*, vol. 378, no. 2186, p. 20 190 605, 2020, ISSN: 1364-503X. DOI: 10.1098/rsta.2019.0605.

[26] S. W. Chee, T. Lunkenbein, R. Schlögl, and B. Roldán Cuenya, "Operando electron microscopy of catalysts: The missing cornerstone in heterogeneous catalysis research?" *Chemical Reviews*, vol. 123, no. 23, pp. 13 374–13 418, Nov. 2023, ISSN: 0009-2665. DOI: 10.1021/acs.chemrev.3c00352.

[27] Q. Yan, X. Li, J. Luo, and M. Zhao, "Single-molecule fluorescence imaging of energy-related catalytic reactions," *Chemical Biomedical Imaging*, vol. 3, no. 5, pp. 280–300, Mar. 2025, ISSN: 2832-3637. DOI: 10.1021/cbmi.4c00112.

[28] G. Barbillon, "Plasmonics and its applications," *Materials*, vol. 12, no. 9, p. 1502, 2019, ISSN: 1996-1944. DOI: 10.3390/ma12091502.

[29] Y.-F. Chou Chau, "Nanophotonic materials and devices: Recent advances and emerging applications," *Micromachines*, vol. 16, no. 8, p. 933, 2025, ISSN: 2072-666X. DOI: 10.3390/mi16080933.

[30] R. L. M. Gieseking, "Plasmons: Untangling the classical, experimental, and quantum mechanical definitions," *Materials Horizons*, vol. 9, no. 1, pp. 25–42, Jan. 2022, ISSN: 2051-6347. DOI: 10.1039/d1mh01163d.

[31] O. Yeshchenko, I. Bondarchuk, V. Gurin, I. Dmitruk, and A. Kotko, "Temperature dependence of the surface plasmon resonance in gold nanoparticles," *Surface Science*, vol. 608, pp. 275–281, 2013, ISSN: 0039-6028. DOI: 10.1016/j.susc.2012.10.019.

[32] Y. Aoki, T. Ishida, and T. Tatsuma, "Plasmon-induced photocatalysis based on pt–au coupling with enhanced oxidation abilities," *ACS Applied Nano Materials*, vol. 5, no. 3, pp. 4406–4412, 2022. DOI: 10.1021/acsanm.2c00509.

[33] V. Amendola, R. Pilot, M. Frasconi, O. M. Maragò, and M. A. Iatì, "Surface plasmon resonance in gold nanoparticles: A review," *Journal of Physics: Condensed Matter*, vol. 29, no. 20, p. 203 002, Apr. 2017. DOI: 10.1088/1361-648X/aa60f3.

[34] C. Langhammer, E. M. Larsson, B. Kasemo, and I. Zorić, "Indirect nanoplasmonic sensing: Ultrasensitive experimental platform for nanomaterials science and optical nanocalorimetry," *Nano Letters*, vol. 10, no. 9, pp. 3529–3538, 2010. DOI: 10.1021/nl101727b.

[35] K. M. Mayer and J. H. Hafner, "Localized surface plasmon resonance sensors," *Chemical Reviews*, vol. 111, no. 6, pp. 3828–3857, Jun. 2011, ISSN: 0009-2665. DOI: 10.1021/cr100313v.

[36] C. Martín-Sánchez, A. Sánchez-Iglesias, J. A. Barreda-Argüeso, A. Polian, L. M. Liz-Marzán, and F. Rodríguez, "Behavior of au nanoparticles under pressure observed by in situ small-angle x-ray scattering," *ACS Nano*, vol. 17, no. 1, pp. 743–751, Dec. 2022, ISSN: 1936-0851. DOI: 10.1021/acsnano.2c10643.

[37] E. M. Larsson, S. Syrenova, and C. Langhammer, "Nanoplasmonic sensing for nanomaterials science," *Nanophotonics*, vol. 1, no. 3–4, pp. 249–266, 2012, ISSN: 2192-8614. DOI: 10.1515/nanoph-2012-0029.

[38] S. Liu et al., "In situ plasmonic nanospectroscopy of the co oxidation reaction over single pt nanoparticles," *ACS Nano*, vol. 13, no. 5, pp. 6090–6100, May 2019, ISSN: 1936-0851. DOI: 10.1021/acsnano.9b02876.

[39] L. Bocquet and E. Charlaix, "Nanofluidics, from bulk to interfaces," *Chemical Society Reviews*, vol. 39, no. 3, pp. 1073–1095, Mar. 2010, ISSN: 0306-0012. DOI: 10.1039/b909366b.

[40] S. Kk, F. Persson, J. Fritzsche, J. P. Beech, J. O. Tegenfeldt, and F. Westerlund, "Fluorescence microscopy of nanochannel-confined dna," in *Single Molecule Analysis: Methods and Protocols*, ser. Methods in Molecular Biology, I. Heller, D. Dulin, and E. J. G. Peterman, Eds., vol. 2694, New York, NY: Humana Press, 2024, pp. 175–202, ISBN: 978-1-0716-3377-9. DOI: 10.1007/978-1-0716-3377-9_9.

[41] T. W. Young, M. P. Kappler, N. M. Hockaden, R. L. Carpenter, and S. C. Jacobson, "Characterization of extracellular vesicles by resistive-pulse sensing on in-plane multipore nanofluidic devices," *Analytical Chemistry*, vol. 95, no. 45, pp. 16 710–16 716, Nov. 2023, ISSN: 0003-2700. DOI: 10.1021/acs.analchem.3c03546.

[42] S. H. Petrosko, R. Johnson, H. White, and C. A. Mirkin, "Nanoreactors: Small spaces, big implications in chemistry," *Journal of the American Chemical Society*, vol. 138, no. 24, pp. 7443–7445, Jun. 2016, ISSN: 0002-7863. DOI: 10.1021/jacs.6b05393.

[43] C. Orahoske, H. Lusk, S. C. Pickard, and A. H. B. Wu, "Fundamentals of mass spectrometry," in *Practical Guide to Implementing Liquid Chromatography Mass Spectrometry in Clinical Laboratories*, Y. V. Zhang and U. Garg, Eds. Cham: Springer Nature Switzerland, 2025, pp. 15–38. DOI: 10.1007/978-3-032-03852-4_2.

[44] W. Zhou, R. Apkarian, Z. L. Wang, and D. Joy, "Fundamentals of scanning electron microscopy (sem)," in *Scanning Microscopy for Nanotechnology: Techniques and Applications*, W. Zhou and Z. L. Wang, Eds. New York, NY: Springer New York, 2007, pp. 1–40, ISBN: 978-0-387-39620-0. DOI: 10.1007/978-0-387-39620-0_1.

[45] P. T. Z. Adibi, "In situ studies of platinum catalyst sintering," Doctoral Thesis, Chalmers University of Technology, Gothenburg, Sweden, 2016, ISBN: 978-91-7597-334-0.

[46] K. McCrea, J. Parker, and G. Somorjai, "High-pressure co dissociation and co oxidation studies on platinum single crystal surfaces using sum frequency generation surface vibrational spectroscopy," in *Surface Chemistry and Catalysis*, A. F. Carley, P. R. Davies, G. J. Hutchings, and M. S. Spencer, Eds. Boston, MA: Springer US, 2002, pp. 55–78, ISBN: 978-1-4757-6637-0. DOI: 10.1007/978-1-4757-6637-0_4.

[47] P. Tabib Zadeh Adibi, V. P. Zhdanov, C. Langhammer, and H. Grönbeck, "Transient bimodal particle size distributions during pt sintering on alumina

and silica," *The Journal of Physical Chemistry C*, vol. 119, no. 2, pp. 989–996, Dec. 2014, ISSN: 1932-7447. DOI: 10.1021/jp506586g.

[48] Y. Hang, A. Wang, and N. Wu, "Plasmonic silver and gold nanoparticles: Shape- and structure-modulated plasmonic functionality for point of-caring sensing, bio-imaging and medical therapy," *Chemical Society Reviews*, vol. 53, no. 6, pp. 2932–2971, 2024, ISSN: 0306-0012. DOI: 10.1039/D3CS00793F.

Appendix A

On the use of A.I.

Throughout the writing of this thesis, A.I. was used as a writing aid in accordance with Chalmers' guidelines[1] on the use of A.I. Before writing this thesis, a proposal was written, outlining exactly how A.I. would be used in this thesis and which was agreed upon by both examiner and supervisor.

A.I. was exclusively used to enhance the grammar, by correcting spelling mistakes and punctuation, and to provide inspiration for minor sentence restructuring, in order to fix the flow of sentences. All A.I.-assisted edits were monitored and manually edited prior to implementation. No auto-generated text was ever used, nor was A.I. used to draw any constitutions or analyze the data.

The following workflow, shown in Figure A.1, showcase the exact procedure of how A.I. was used for a paragraph in the abstract.

[1] "Regulations for the use of AI tools in thesis work", *Chalmers*, Last updated: Dec. 2024. [Online]. Available: https://www.chalmers.se/en/education/your-studies/masters-and-bachelors-thesis/regulations-for-the-use-of-ai-tools/

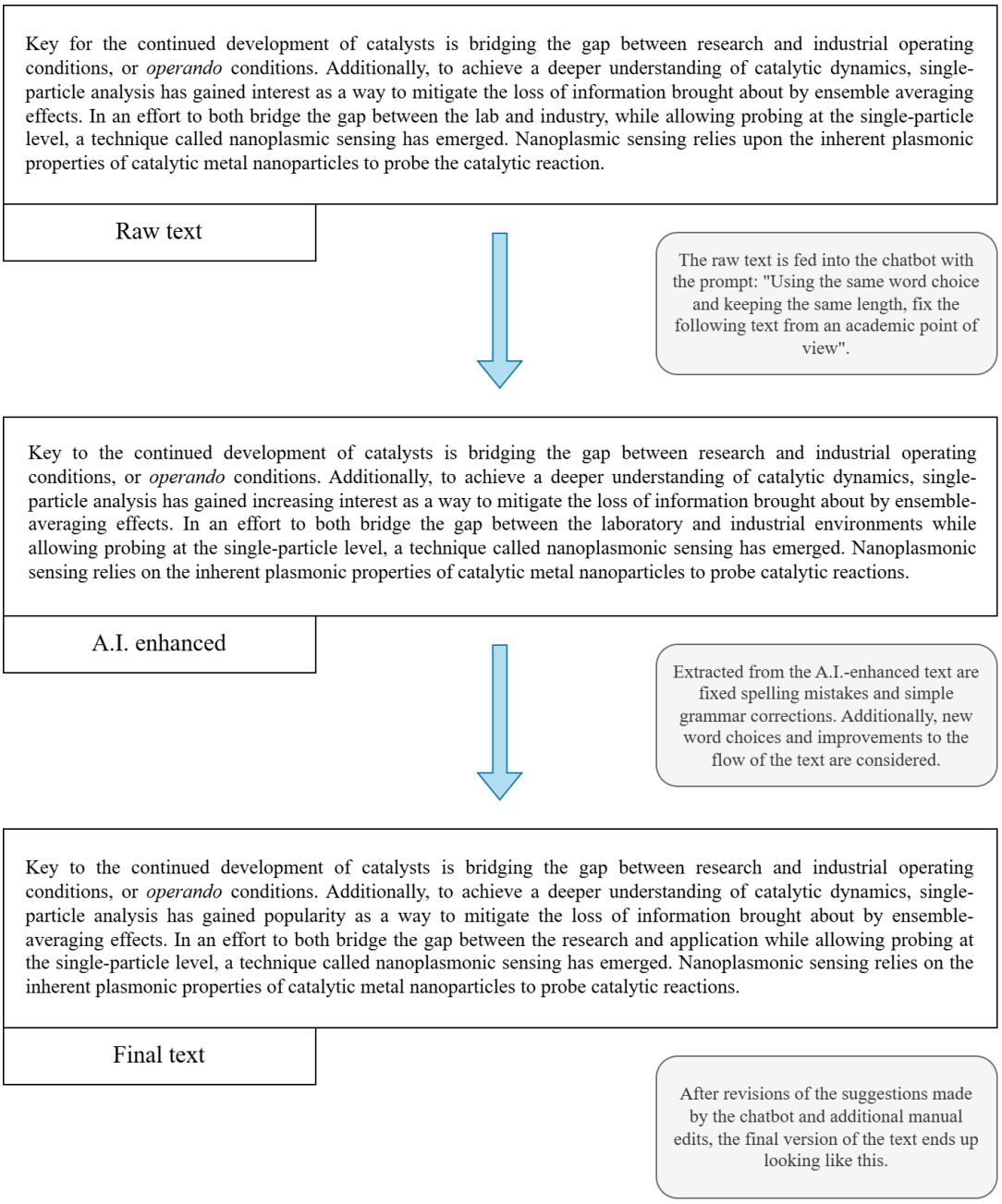

Figure A.1: An example workflow showcasing the use of A.I.

Appendix B

Complementary data: Ensemble analysis

The following appendix consists of complementary data for the nanoplasmonic sensing ensemble analysis. The data presented in this appendix are divided with respect to each part of the analysis presented in the main text in Section 4.1.1.

Presented in Appendix B.1 are the complementary figures to Figure 4.1, for the gas compositions 1:0.25, only CO, and only O_2. Appendix B.2 showcases the bootstrap-derived inflection points obtained when a cubic spline is used instead to fit the data once the Ar background has been removed. Lastly, Appendix B.3 contains complementary tables to Table 4.1 and Table 4.2, hosting the calculated critical temperatures and confidence intervals for gas compositions of 1:0.25, only CO and only O_2.

B.1 Complementary figures to Figure 4.1

Presented bellow are the complementary figures to Figure 4.1, for gas compositions of 1:0.25, in Figure B.1a, only CO, in Figure B.1b, and only O_2, in Figure B.1c.

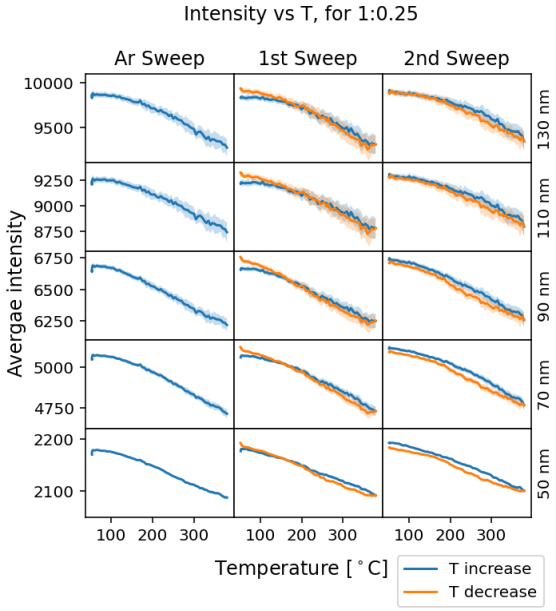

(a) Gas composition of 1:0.25.

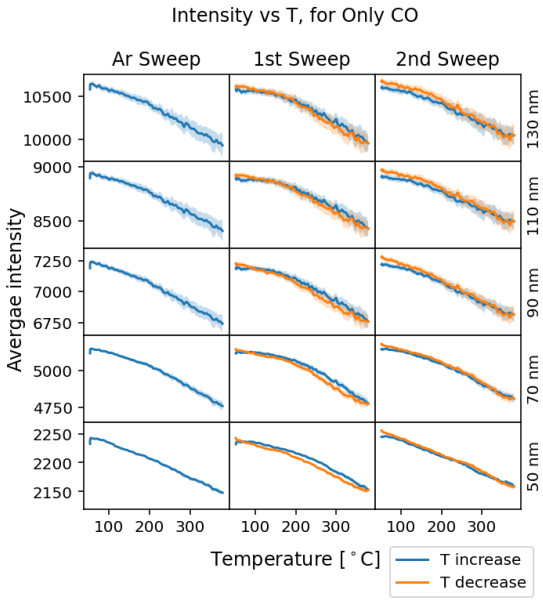

(b) Gas composition of only CO.

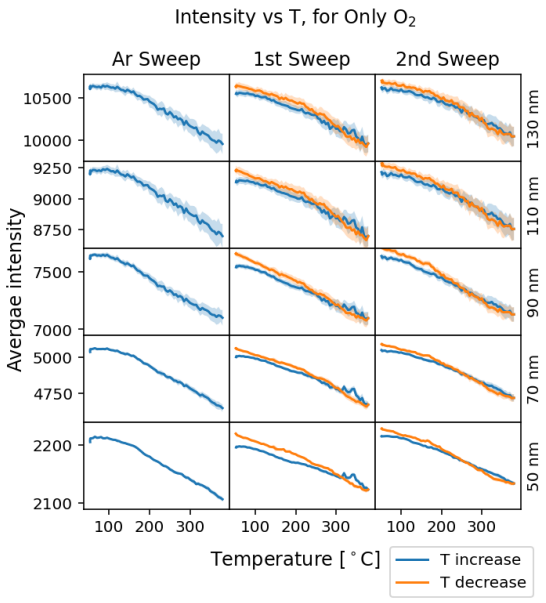

(c) Gas composition of only O_2.

Figure B.1: Complementary figures to Figure 4.1 for gas compositions of 1:0.25, only CO, and only O_2. For each subfigure, the mean intensity as a function of temperature for the Ar, first and second sweeps, are presented for each particle size. The blue and orange lines represent the temperature-increasing and -decreasing parts of the sweep cycle, respectively. The shaded area represents the standard deviation of the mean intensity.

B.2 Bootstrap-derived inflection points of cubic spline fits

The following are complementary figures to Figure 4.5 and Figure 4.6, representing the bootstrap-derived inflection points evaluated using a smooth cubic spline instead of fourth-degree polynomials. Presented in Figure B.2 are the 1:0.5 and 1:0.25 measurements, while the measurements for only CO and only O_2 are presented in Figure 4.6.

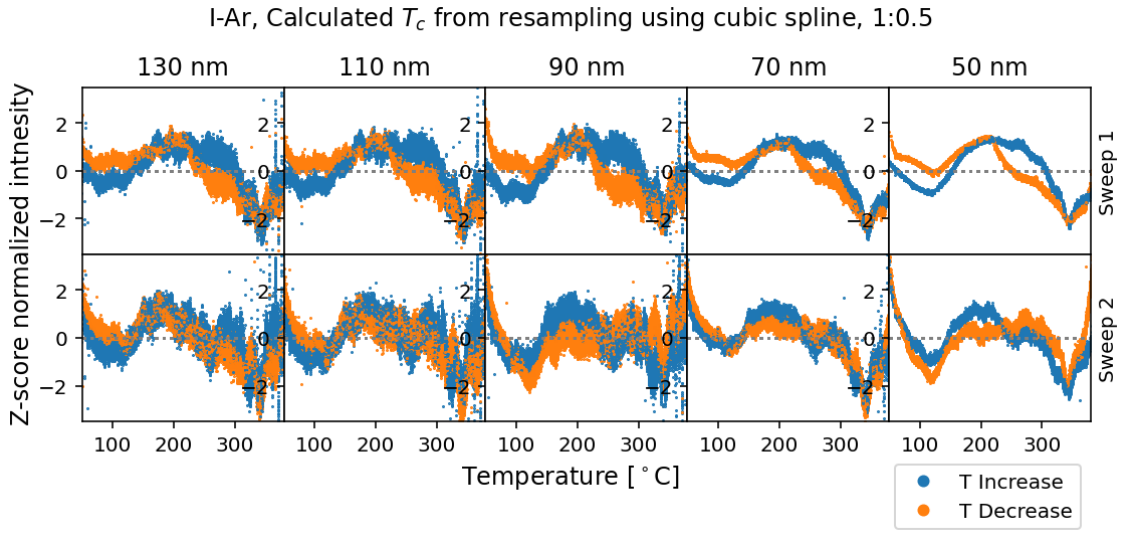

(a) 1:0.5 ratio.

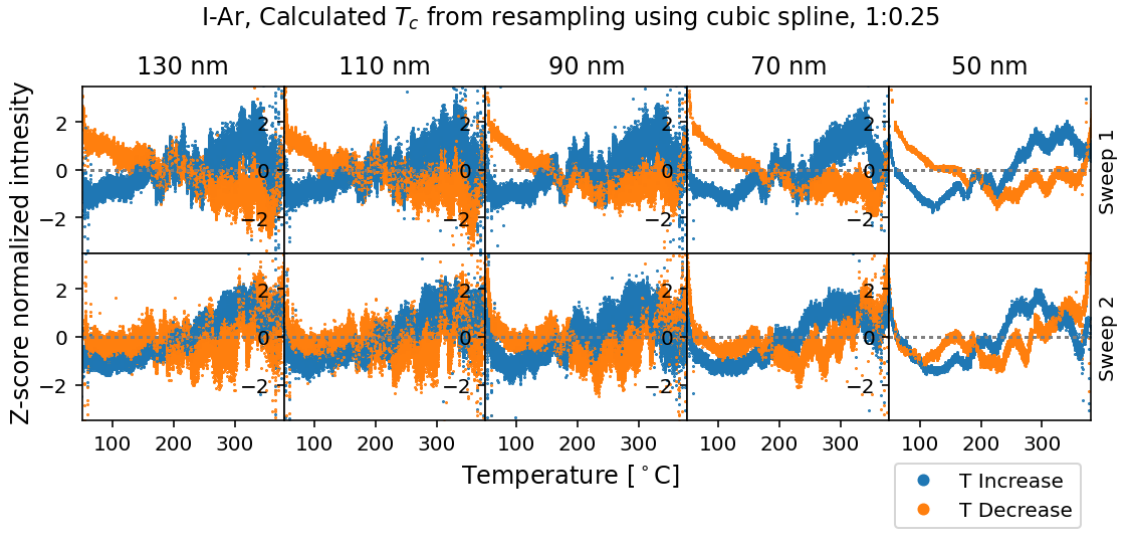

(b) 1:0.25 ratio.

Figure B.2: Plots showcasing bootstrap approach for cubic splines at gas compositions 1:0.5 and 1:0.25, the calculated inflection-points for both temperature increase and decease of each sweep. When the data is closely bundled then that correlates to a good statistical value for the model, while spread points correlates to a poor statistical value of the model.

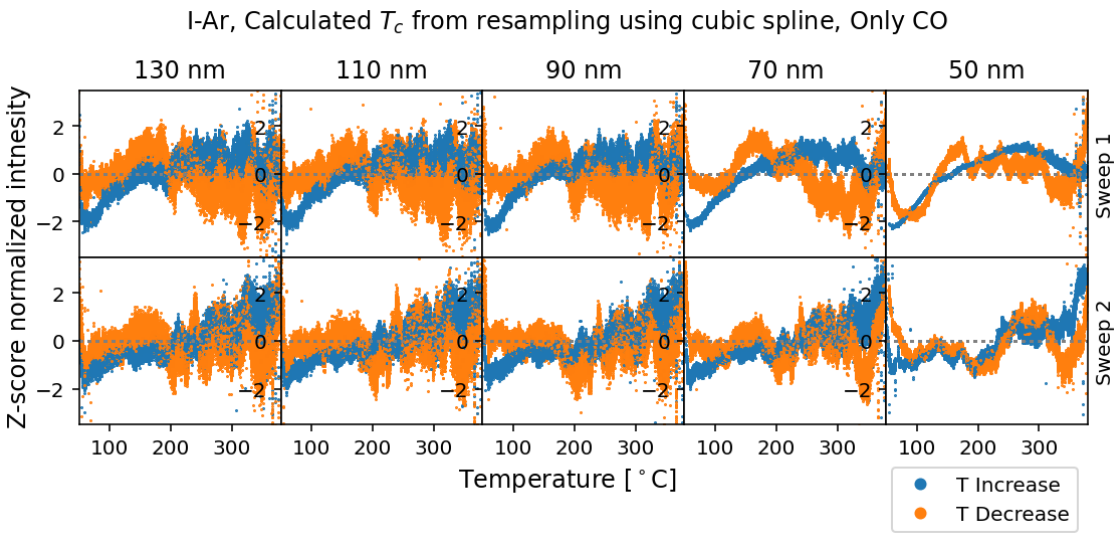

(a) Only CO.

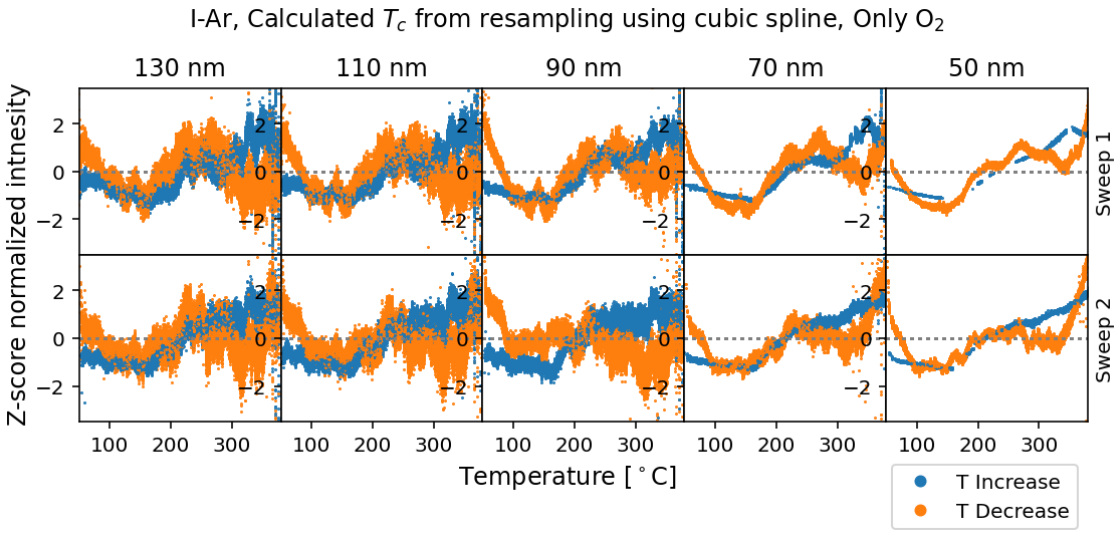

(b) Only O_2.

Figure B.3: Plots showcasing bootstrap approach for cubic splines at gas compositions only O_2 and only CO, the calculated inflection-points for both temperature increase and decease of each sweep. When the data is closely bundled then that correlates to a good statistical value for the model, while spread points correlates to a poor statistical value of the model.

B.3 Complementary tables to Tables 4.1 and 4.2

The following are complementary to Table 4.1 and Table 4.2, containing the evaluated critical temperatures and corresponding 95 % confidence intervals for both the lower- and upper-temperature transitions, for both sweeps and for the temperature-increasing and temperature-decreasing parts of the sweep cycle. Presented in Appendix B.3.1 are the results for a gas composition of 1:0.25, found in Appendix B.3.2 are the results for a gas composition of only CO and finally contained in Appendix B.3.3 are the results for a gas composition of only O_2.

B.3.1 Evaluated T_c at a gas composition of 1:0.25

Listed in Table B.1 are the evaluated critical temperatures and corresponding 95% confidence intervals for the first sweep, for both the upper- and lower-temperature transitions, at a gas composition of 1:0.25. Present in B.2 are the corresponding results for second sweep.

	Sweep 1							
	Up T_1		Down T_1		Up T_2		Down T_2	
NP [nm]	T_c	C.I.	T_c	C.I.	T_c	C.I.	T_c	C.I.
130	131.50	±1.46	131.50	±1.46	253.37	±15.86	258.06	±1.16
110	113.69	±2.79	113.69	±2.79	273.53	±41.76	277.41	±3.40
90	83.28	±5.65	83.28	±5.65	168.05	±107.98	233.05	±15.91
70	41.03	±4.39	41.03	±4.39	194.65	±63.72	246.79	±0.63
50	165.26	±9.86	165.27	±9.86	-605.14	±389.74	222.17	±0.16

Table B.1: Table of mean critical temperatures, and their respective 95% confident intervals (C.I.), calculated from the bootstrap-derived inflection points presented in Figure 4.5b. Listed are both evaluated critical temperatures (with the lower T_c presented as T_1 and the upper T_c as T_2), for both the temperature-increasing and temperature-decreasing parts of the first measurement sweep, at a gas composition of 1:0.25.

	Sweep 2							
	Up T_1		Down T_1		Up T_2		Down T_2	
NP [nm]	T_c	C.I.	T_c	C.I.	T_c	C.I.	T_c	C.I.
130	84.09	±8.41	84.10	±8.41	3280.72	±4809.72	241.24	±282.39
110	137.87	±7.51	137.86	±7.51	151.26	±310.18	288.92	±55.91
90	187.87	±1.89	187.87	±1.89	443.94	±104.32	157.65	±146.67
70	197.14	±0.37	197.15	±0.37	445.13	±7.99	206.38	±1.14
50	203.12	±0.16	203.12	±0.16	503.23	±3.69	223.34	±0.64

Table B.2: Table of mean critical temperatures, and their respective 95% confident intervals (C.I.), calculated from the bootstrap-derived inflection points presented in Figure 4.5b. Listed are both evaluated critical temperatures (with the lower T_c presented as T_1 and the upper T_c as T_2), for both the temperature-increasing and temperature-decreasing parts of the second measurement sweep, at a gas composition of 1:0.25.

B.3.2 Evaluated T_c at a gas composition of only CO

Listed in Table B.3 are the evaluated critical temperatures and corresponding 95% confidence intervals for the first sweep, for both the upper- and lower-temperature transitions, at a gas composition of of only CO. Present in B.4 are the corresponding results for second sweep.

	Sweep 1							
	Up T_1		Down T_1		Up T_2		Down T_2	
NP [nm]	T_c	C.I.	T_c	C.I.	T_c	C.I.	T_c	C.I.
130	141.74	±7.97	78.28	±3.56	268.24	±109.60	261.41	±46.10
110	129.09	±8.02	94.84	±3.54	350.45	±132.98	196.41	±105.42
90	165.79	±10.72	111.85	±1.29	-108.44	±620.30	251.17	±1.51
70	99.43	±1.37	131.01	±0.11	337.86	±35.54	265.59	±0.11
50	105.23	±0.37	143.76	±0.05	361.42	±1.40	278.02	±0.08

Table B.3: Table of mean critical temperatures, and their respective 95% confident intervals (C.I.), calculated from the bootstrap-derived inflection points presented in Figure 4.6a. Listed are both evaluated critical temperatures (with the lower T_c presented as T_1 and the upper T_c as T_2), for both the temperature-increasing and temperature-decreasing parts of the first measurement sweep, at a gas composition of only CO.

	Sweep 2							
	Up T_1		Down T_1		Up T_2		Down T_2	
NP [nm]	T_c	C.I.	T_c	C.I.	T_c	C.I.	T_c	C.I.
130	132.25	±3.32	107.17	±4.31	234.11	±77.55	382.46	±190.64
110	131.68	±3.61	130.48	±3.16	456.31	±766.75	285.34	±73.74
90	131.01	±3.69	180.05	±4.83	9291.95	±18069.41	243.17	±16.17
70	127.09	±1.58	156.03	±0.22	196.23	±66.40	272.29	±0.27
50	173.09	±0.89	187.19	±0.22	230.58	±0.92	307.39	±0.49

Table B.4: Table of mean critical temperatures, and their respective 95% confident intervals (C.I.), calculated from the bootstrap-derived inflection points presented in Figure 4.6a. Listed are both evaluated critical temperatures (with the lower T_c presented as T_1 and the upper T_c as T_2), for both the temperature-increasing and temperature-decreasing parts of the second measurement sweep, at a gas composition of only CO.

B.3.3 Evaluated T_c at a gas composition of only O_2

Listed in Table B.5 are the evaluated critical temperatures and corresponding 95% confidence intervals for the first sweep, for both the upper- and lower-temperature transitions, at a gas composition of of only O_2. Present in B.6 are the corresponding results for second sweep.

	Sweep 1							
	Up T_1		Down T_1		Up T_2		Down T_2	
NP [nm]	T_c	C.I.	T_c	C.I.	T_c	C.I.	T_c	C.I.
130	43.08	±6.48	168.38	±0.24	139.48	±117.51	305.94	±0.65
110	154.64	±9.00	170.13	±0.20	2375.21	±4280.93	301.17	±0.48
90	204.82	±5.40	174.77	±0.17	74.25	±500.58	301.28	±0.38
70	166.93	±10.61	172.37	±0.09	-128.99	±1130.71	299.87	±0.18
50	257.00	±0.10	174.74	±0.05	-1187.02	±2758.87	297.37	±0.09

Table B.5: Table of mean critical temperatures, and their respective 95% confident intervals (C.I.), calculated from the bootstrap-derived inflection points presented in Figure 4.6b. Listed are both evaluated critical temperatures (with the lower T_c presented as T_1 and the upper T_c as T_2), for both the temperature-increasing and temperature-decreasing parts of the first measurement sweep, at a gas composition of only O_2.

	Sweep 2							
	Up T_1		Down T_1		Up T_2		Down T_2	
NP [nm]	T_c	C.I.	T_c	C.I.	T_c	C.I.	T_c	C.I.
130	158.20	±7.84	164.09	±0.29	2371.33	±4416.29	284.04	±0.49
110	201.52	±3.16	167.04	±0.28	745.07	±971.12	278.87	±0.35
90	197.23	±0.56	161.78	±0.19	464.57	±44.91	277.41	±0.24
70	201.57	±0.39	164.80	±0.10	335.26	±1.59	274.67	±0.11
50	193.34	±0.16	162.37	±0.05	308.55	±0.36	273.62	±0.05

Table B.6: Table of mean critical temperatures, and their respective 95% confident intervals (C.I.), calculated from the bootstrap-derived inflection points presented in Figure 4.6b. Listed are both evaluated critical temperatures (with the lower T_c presented as T_1 and the upper T_c as T_2), for both the temperature-increasing and temperature-decreasing parts of the second measurement sweep, at a gas composition of only O_2.

Appendix C

Drift analysis

In this appendix, a further analysis of the drift in intensity, as noted in Section 4.1.1, is presented. This analysis was included as complementary material, as it was not used to draw any conclusions or to support any further analysis.

To investigate the drift, that is, the difference in intensity between the temperature-decreasing and temperature-increasing parts of the sweep cycle after a full sweep has been completed and the temperature has returned to 50 °C, the intensity of the temperature-decreasing part of the sweep cycle was subtracted from that of the temperature-increasing part. The resulting differences are presented in Figure C.1 for a gas composition of 1:0.5.

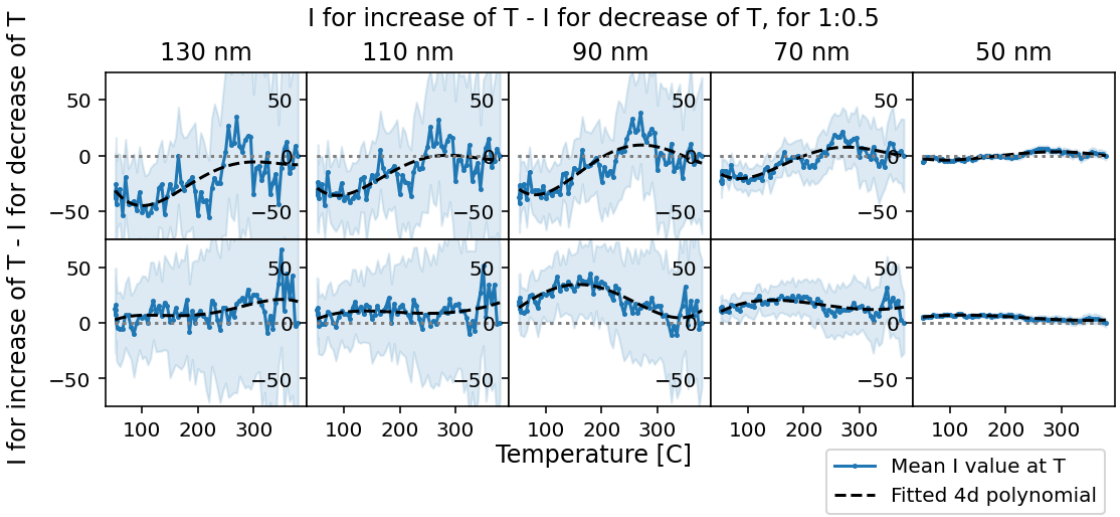

Figure C.1: Plots displaying the difference in mean intensity between increasing and decreasing temperature, at a gas ratio of 1:0.5 for particle sizes with radii of 50–130 nm, for both the first and second sweep. The solid blue line represents the mean, with the shaded region indicating the standard deviation. The dashed line represents a fourth-degree polynomial fitted to the data.

As the main interest is to assess the difference in intensity before and after the temperature cycle, the difference, as evaluated by the fourth-degree polynomial fitted to the data in Figure C.1, and the standard deviation were extracted at 50 °C for all gas compositions and presented as a function of particle size in the following set of plots.

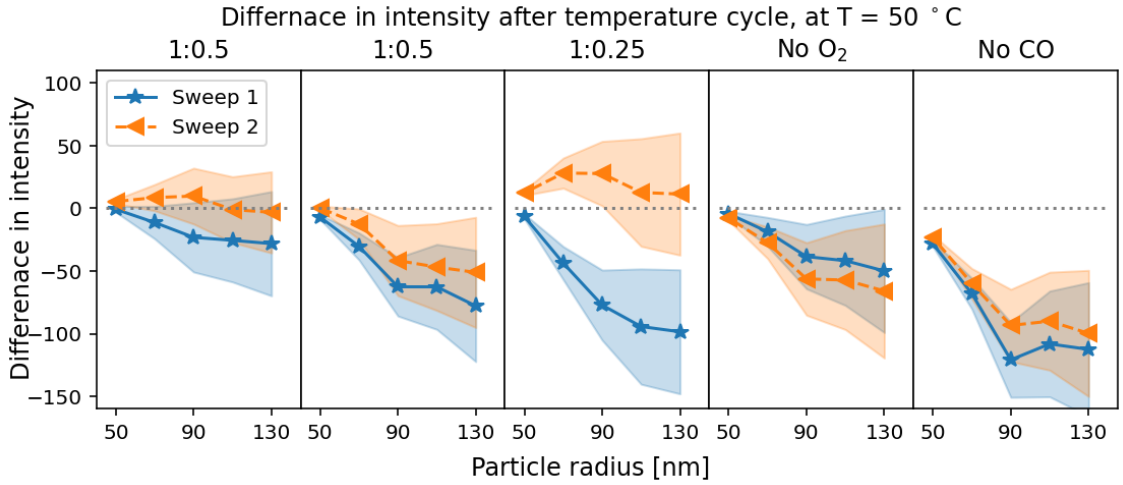

Figure C.2: The anisotropic drift in intensity throughout the measurement as a function of size, for different gas compositions. This was calculated for both sweeps using the fitted model displayed in Figure C.1 at a temperature of 50°C, representing a full temperature cycle. The shaded area represents the stand derivative at 50°C for each particle size.

Appendix D

Complementary data: Single-particle analysis

This appendix consists of complementary data to the single-particle analysis of the nanoplasmonic sensing data, conducted in Section 4.1.2. Each of the following sections are dedicated to their own receptive part of the analysis presented in the main text.

Presented in Appendix D.1 are the complementary figures to Figure 4.8, representing the mean intensity data after removal of the Ar background for the remaining particle sizes. Similarly, Appendix D.2 presents complementary figures to Figure 4.9, corresponding to the bootstrap-derived inflection points for the remaining particle sizes, obtained from the same data set used to plot the figures in Appendix D.1.

D.1 Complementary figures to Figure 4.8

The following figures are complementary to Figure 4.8 and show the plasmonic responses, as a function of temperature, after removal of the Ar background in the single-particle data for different particle sizes at a gas composition of 1:0.5. Presented in Figure D.1a are the second-sweep responses for particles of radius 130 nm, while Figures D.1b–D.3b present the corresponding figures, containing both sweep cycles, for particles with radii of 110–50 nm.

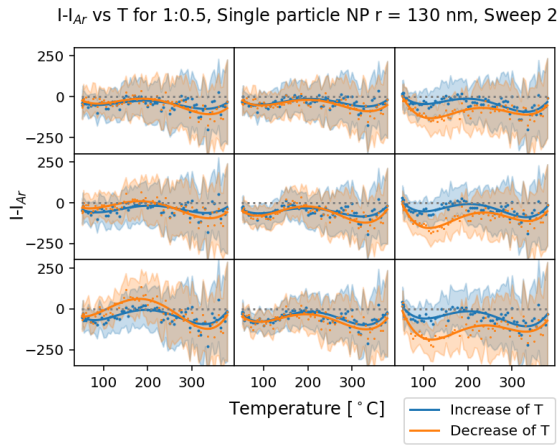

(a) Second sweep, particles of radius 130 nm.

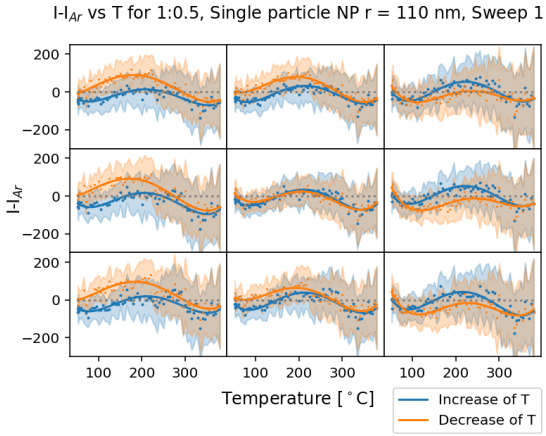

(b) First sweep, particles of radius 110 nm.

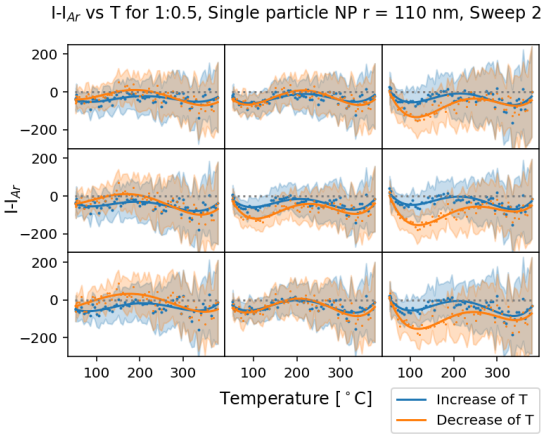

(c) Second sweep, particles of radius 110 nm.

Figure D.1: Showcasing the mean nanoplasmonic response as a function of temperature after removal of the Ar background for each nanoparticle in the 130 nm and 110 nm arrays, respectively, at a gas composition of 1:0.5. The solid lines represent fourth-degree polynomial fits to the mean intensities, with the blue and orange lines representing the temperature-increasing and temperature-decreasing parts of the sweep cycle, respectively. The shaded area represents the standard deviation of the mean intensity at each temperature step. In **(a)**, a complementary figure to Figure 4.8, representing the second sweep cycle for the 130 nm array, is presented. Shown in **(b)** and **(c)** are the first and second sweep cycles, respectively, for particles with a radius of 110 nm.

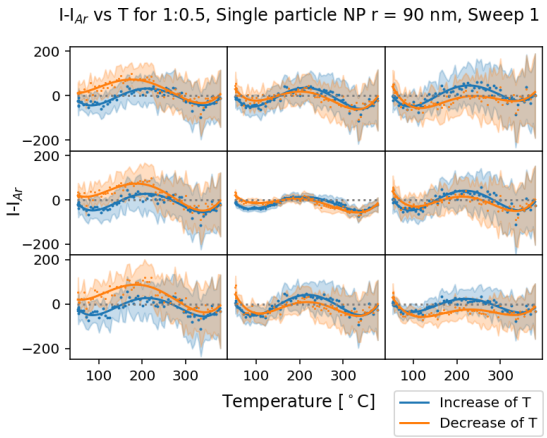

(a) First sweep, particles of radius 90 nm.

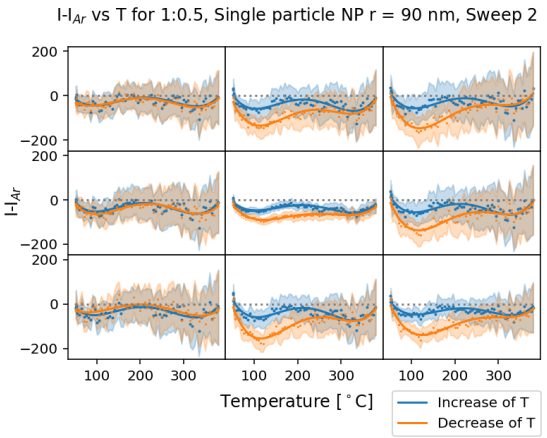

(b) Second sweep, particles of radius 90 nm.

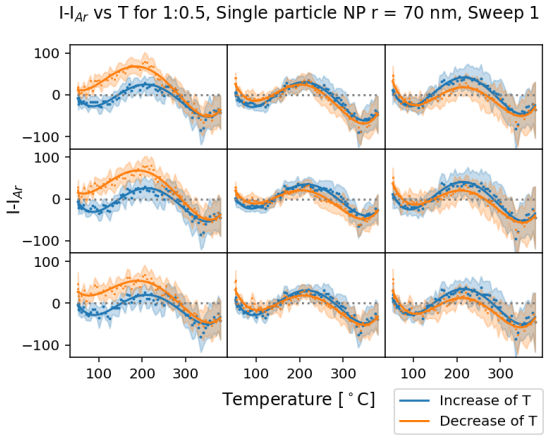

(c) First sweep, particles of radius 70 nm.

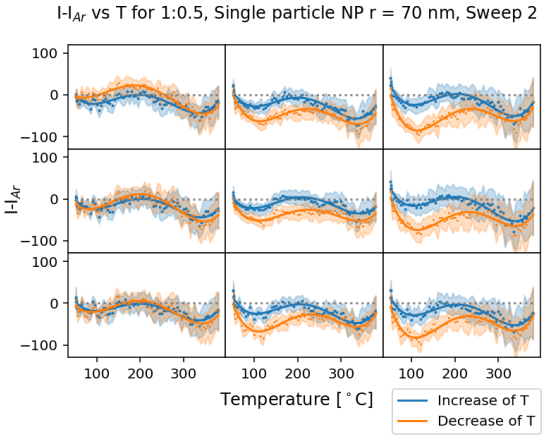

(d) Second sweep, particles of radius 70 nm.

Figure D.2: Showcasing the mean nanoplasmonic response as a function of temperature after removal of the Ar background for each nanoparticle in the 90 nm and 70 nm arrays, respectively, at a gas composition of 1:0.5. The solid lines represent fourth-degree polynomial fits to the mean intensities, with the blue and orange lines representing the temperature-increasing and temperature-decreasing parts of the sweep cycle, respectively. The shaded area represents the standard deviation of the mean intensity at each temperature step. In **(a)** and **(b)** are the first and second sweep cycles, respectively, for particles with a radius of 90 nm. Shown in **(c)** and **(d)** are the first and second sweep cycles, respectively, for particles with a radius of 70 nm.

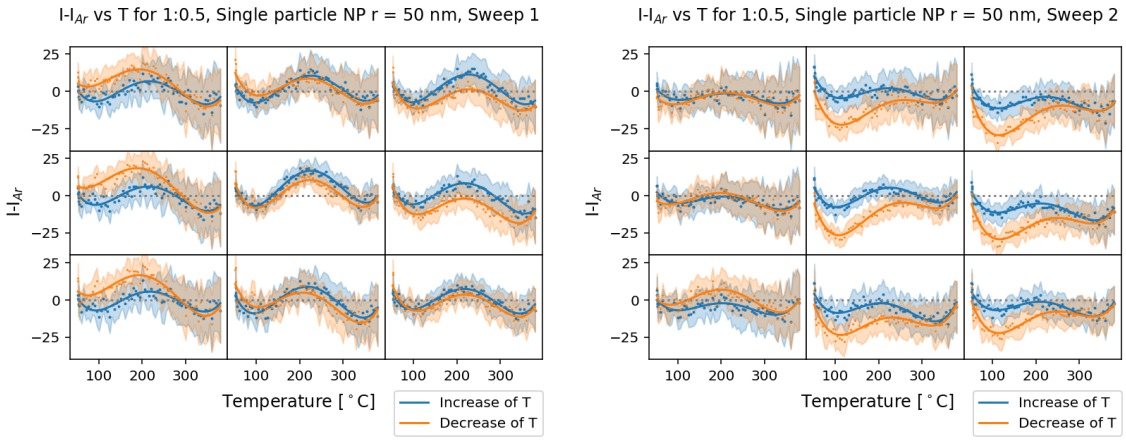

(a) First sweep, particles of radius 50 nm. **(b)** Second sweep, particles of radius 50 nm.

Figure D.3: Showcasing the mean nanoplasmonic response as a function of temperature after removal of the Ar background for each nanoparticle in the 50 nm array, at a gas composition of 1:0.5. The solid lines represent fourth-degree polynomial fits to the mean intensities, with the blue and orange lines representing the temperature-increasing and temperature-decreasing parts of the sweep cycle, respectively. The shaded area represents the standard deviation of the mean intensity at each temperature step. Presented **(a)** and **(b)** are the first and second sweep cycles, respectively, for particles with a radius of 50 nm.

D.2 Complementary figures to Figure 4.9

The following figures complement Figure 4.9 and represent the clustering of bootstrap-derived inflection points at a gas composition of 1:0.5, corresponding to the data presented in Appendix D.1. Figure D.4a presents the derived inflection points for the second sweep of particles with a radius of 130 nm, while Figures D.4b–D.6 present the corresponding inflection points for particles with radii between 110–50 nm, showcasing both measurement sweeps.

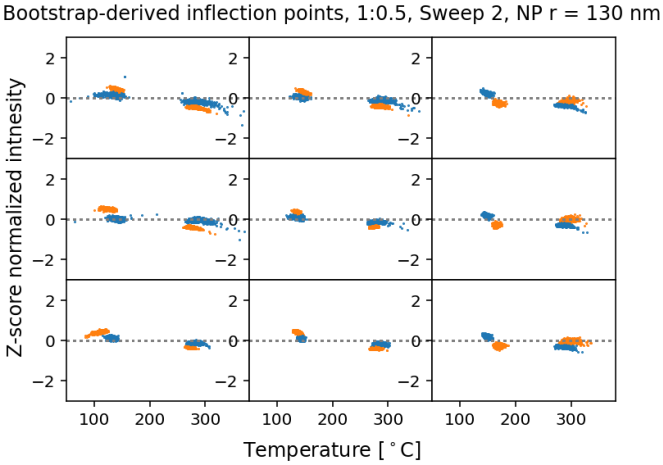

(a) Second sweep, particles of radius 130 nm.

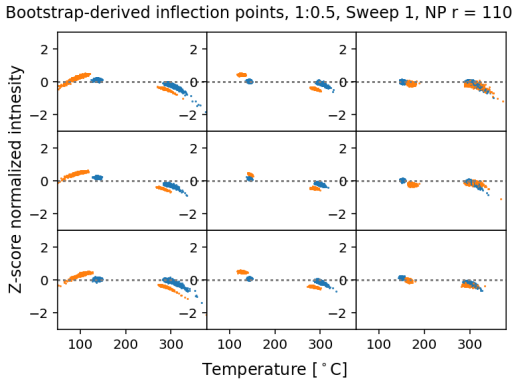

(b) First sweep, particles of radius 110 nm.

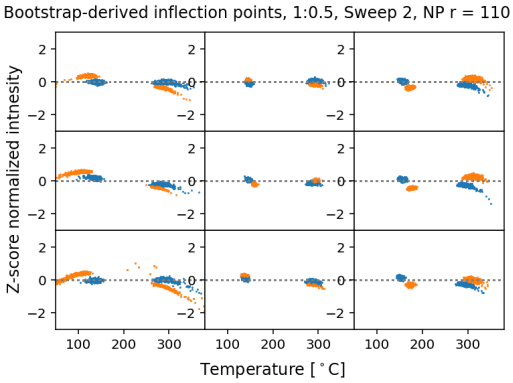

(c) Second sweep, particles of radius 110 nm.

Figure D.4: Showcasing the clustering of bootstrap-derived inflection points extracted from fourth-degree polynomials fitted to resampled nanoplasmonic sensing data, after removal of the Ar background, at a gas composition of 1:0.5. Presented in **(a)** are bootstrap-derived inflection points corresponding to the second measurement sweep for each particle with a radius of 130 nm. Shown in **(b)** and **(c)** are the corresponding inflection points for the first and second measurement sweeps, respectively, for each particle with a radius of 110 nm.

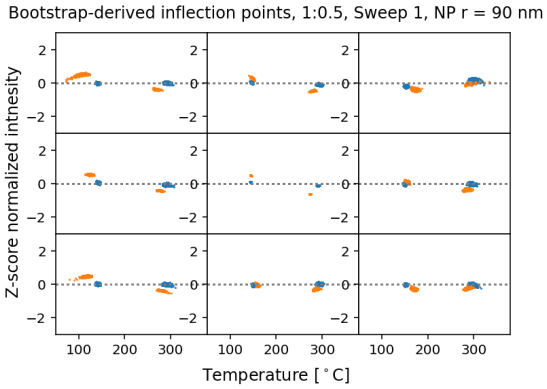

(a) First sweep, particles of radius 90 nm.

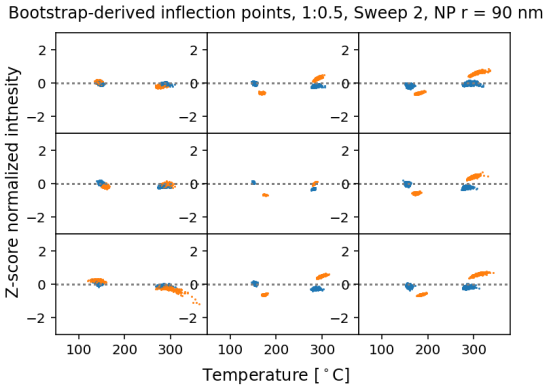

(b) Second sweep, particles of radius 90 nm.

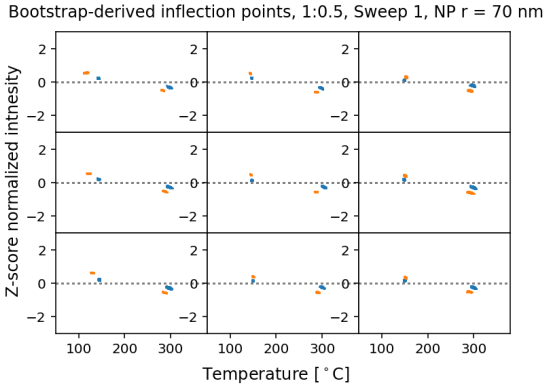

(c) First sweep, particles of radius 70 nm.

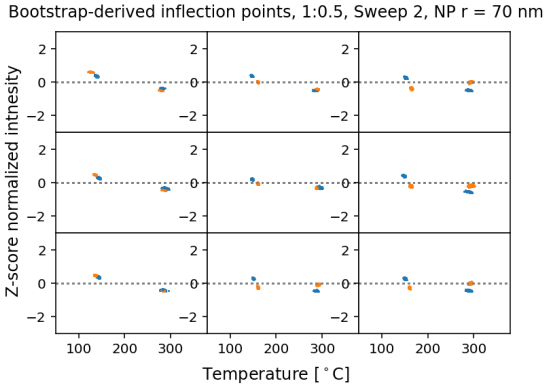

(d) Second sweep, particles of radius 70 nm.

Figure D.5: Showcasing the clustering of bootstrap-derived inflection points extracted from fourth-degree polynomials fitted to resampled nanoplasmonic sensing data, after removal of the Ar background, at a gas composition of 1:0.5. Presented in **(a)** and **(b)** are the bootstrap-derived inflection points corresponding to the first and second measurement sweeps, respectively, for each particle with a radius of 90 nm. Shown in **(c)** and **(d)** are the corresponding inflection points for the first and second measurement sweeps, respectively, for each particle with a radius of 70 nm.

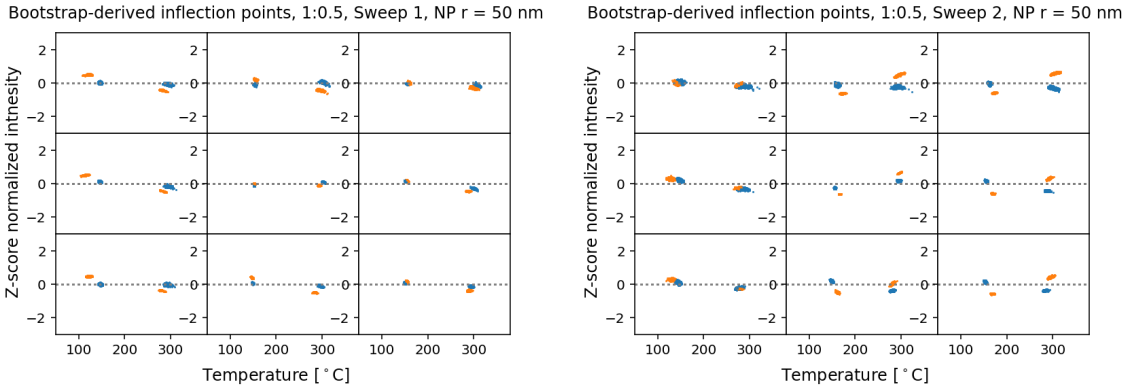

(a) First sweep, particles of radius 50 nm. **(b)** Second sweep, particles of radius 50 nm.

Figure D.6: Showcasing the clustering of bootstrap-derived inflection points extracted from fourth-degree polynomials fitted to resampled nanoplasmonic sensing data, after removal of the Ar background, at a gas composition of 1:0.5. Presented in **(a)** and **(b)** are the bootstrap-derived inflection points corresponding to the first and second measurement sweeps, respectively, for each particle with a radius of 50 nm.

DEPARTMENT OF PHYSICS
CHALMERS UNIVERSITY OF TECHNOLOGY
Gothenburg, Sweden
www.chalmers.se

CHALMERS
UNIVERSITY OF TECHNOLOGY